# On the origin of crack initiation in duplex stainless steel during cyclic loading in the VHCF regime

HONGWANG FU

UNIVERSITÄT
SIEGEN

SIEGENER WERKSTOFFKUNDLICHE BERICHTE | BAND 17/2017
HERAUSGEBER: PROF. DR.-ING. HABIL. H.-J. CHRIST

**Hongwang Fu**

# On the origin of crack initiation in duplex stainless steel during cyclic loading in the VHCF regime

SIEGENER WERKSTOFFKUNDLICHE BERICHTE 2017

Bibliografische Information der Deutschen Nationalbibliothek
Die Deutsche Nationalbibliothek verzeichnet diese Publikation in der Deutschen Nationalbibliografie; detaillierte bibliografische Daten sind im Internet über
http://dnb.d-nb.de abrufbar.

Dissertation, Universität Siegen, 2017

Herausgeber:
Prof. Dr.-Ing. habil. H.-J. Christ
Lehrstuhl für Materialkunde und Werkstoffprüfung
Institut für Werkstofftechnik
Paul-Bonatz-Str. 9-11
Universität Siegen
D-57068 Siegen

© Copyright Hongwang Fu 2017
© Copyright Lehrstuhl für Materialkunde und Werkstoffprüfung,
Universität Siegen 2017
Alle Rechte vorbehalten, auch das des auszugsweisen Nachdruckes,
der auszugsweisen oder vollständigen Wiedergabe, der Speicherung
in Datenverarbeitungsanlagen und das der Übersetzung.

Als Manuskript gedruckt. Printed in Germany.

urn:nbn:de:hbz:467-12236
ISSN 2193-5114

# On the origin of crack initiation in duplex stainless steel during cyclic loading in the VHCF regime

Dissertation
zur Erlangung des Grades eines Doktors
der Ingenieurwissenschaften (Dr.-Ing.)

vorgelegt von
M.Sc. Hongwang Fu

eingereicht bei der Naturwissenschaftlich-Technischen Fakultät
der Universität Siegen
Siegen 2017

Referent: Prof. Dr.-Ing. habil. Hans-Jürgen Christ
Korreferent: Prof. Dr.-Ing. habil. Ulrich Krupp

Tag der mündlichen Prüfung: 06.10.2017

# Eidesstaatliche Erklärung

Hiermit erkläre ich, dass ich die vorliegende Dissertation selbstständig und ohne unzulässige Hilfe Dritter durchgeführt und verfasst habe. Alle verwendeten Textteile, Zeichnungen, Diagramme, Tabellen aus anderen Quellen habe ich als solche gekennzeichnet. Ich versichere weiterhin, dass diese Dissertation noch keinem anderen Prüfungsamt vorgelegen hat.

Hongwang Fu

# Acknowledgements

I would like to express my deep sense of gratitude to my supervisor Prof. Christ for accepting me as his Ph.D. student and introducing me to this fascinating research field of very high cycle fatigue, for suggesting me challenging research problems, and for his support and encouragement during my work. His patience with explaining German culture during my study here, I will never forget.

I would like to give my thanks to my colleague Andrei Grigorescu, from whom I have learnt much about using experimental apparatuses such as transmission electron microscopy, focused ion beam, servo-hydraulic fatigue machine etc. He is also always generous to share his experiences and knowledge. Discussion with him is a great help for my research. Working with colleague Benjamin Dönges, focusing on our project, is a very delightful time and would be an impressive memory for me. Another ‘VHCF member’, Anton Kolyshkin, always made our talking become interesting and with full of joy. Learning TEM and FIB as a beginner with Fatih Bülbül is a wonderful time.

I am also grateful to Dipl. –Ing. Wolfgang Kramer who always helped me for solving all the technical problems. Without this, my research could not go so smoothly. My thanks would be also given to all the group members in our institute who created an indeed pleasant working environment.

I also want to thank my colleague Lin Wang who always extended his hand of showing me how to get used to life in Germany. His humour gave me a real grateful time. The young Prof. Jian Xiong, working in the same office with me, made my time pleasant.

Significant financial support from China Scholarship Council is gratefully acknowledged. This experience, living and studying in Germany, will be one of the most precious memories in my life.

Finally, I would like to thank my Grandmother, my parents, my brother and my wife Jing Zhu, for their support, encouragement, love and patience.

March, 2016

Hongwang Fu

# Table of Contents

**Kurzfassung** ........ III

**Abstract** ........ IV

**Symbols and abbreviations** ........ V

**1 Introduction** ........ 1

**2 Technical background and literature review** ........ 5

2.1 Fatigue behaviour of metallic materials ........ 5

2.1.1 Cyclic deformation behaviour ........ 5

2.1.2 Crack initiation mechanisms ........ 11

2.2 Duplex stainless steels ........ 19

2.2.1 Physical and mechanical properties ........ 19

2.2.2 Fundamentals of residual stresses ........ 24

2.2.3 Load sharing in two-phase alloys ........ 32

**3 Experimental techniques** ........ 37

3.1 Materials, specimen preparation and test apparatuses ........ 37

3.1.1 Materials and specimens used ........ 37

3.1.2 Ultrasonic fatigue machine ........ 39

3.1.3 Resonance and servo-hydraulic fatigue machine ........ 39

3.1.4 Nanoindentation ........ 40

3.2 Optical and electron microscopy ........ 40

3.2.1 Confocal laser microscopy ........ 40

3.2.2 Scanning electron microscopy ........ 40

3.2.3 Transmission electron microscopy ........ 40

3.3 Synchrotron and laboratory X-ray diffraction ........ 40

3.4 Digital image correlation ........ 45

**4 Results and discussion** ........ 46

4.1 Fatigue-induced residual stress redistribution........................................................46

4.1.1 Residual stress development in VHCF ........................................................46

4.1.2 Development of residual stresses in HCF ....................................................49

4.1.3 Discussion on residual stress development ...................................................52

4.2 Damage evolution ..........................................................................................................56

4.2.1 Formation of slip markings ..........................................................................56

4.2.2 Characterisation of micro-hardness..............................................................60

4.2.3 Variation of dislocation densities and arrangements ......................................64

4.2.4 Observation of micro-cracks ........................................................................71

4.3 In-situ stress distribution...............................................................................................73

4.4 Strain mapping and strain localisation ..........................................................................76

4.4.1 Mapping of residual strains............................................................................78

4.4.2 In-situ strain variation ..................................................................................79

4.5 Modelling of crack initiation ........................................................................................82

4.5.1 Intergranular micro-crack ..............................................................................82

4.5.2 Transgranular micro-crack.............................................................................87

**5 Concluding discussion ......................................................................... 93**

**6 Conclusions and future aspects........................................................ 96**

**7 Appendix ............................................................................................ 99**

**8 References ........................................................................................ 101**

# Kurzfassung

Die Mikrorissbildung eines Dulpexedelstahls (DSS) im VHCF Bereich wurde untersucht und diskutiert. Verschiedene Techniken mit hoher Auflösung wurden an den ermüdeten Proben implementiert, wobei die mechanischen Eigenschaften des DSSs identifiziert und mit den Mechanismen der Mikrorissinitiierung in Bezug gesetzt wurden. Die Ergebnisse der optischen Mikroskopie, Nanoindentierungstests und Synchrotronstrahlungsuntersuchungen zeigten auf, dass die austenitische Phase des DSS in VHCF ein zyklisches Entfestigung-Verfestigung-Entfestigungs Verhalten aufweisen. Die erste zyklische Entfestigung erfolgt während der ersten Million Lastzyklen, wo ein kontinuierliches Wachstum der Gleitspuren und eine Abnahme der Mikrohärte beobachtet wurden. Danach verfestigen die Austenitkörner; dies zeigte sich durch einen Wachstumsstopp der Gleitspuren und eine Erhöhung der Mikrohärte. Synchrotronstrahlungsexperimente, die in diesem Stadium durchgeführt wurden, zeigten, dass die Mikroeigenspannungen zwischen den beiden Phasen im Vergleich zum Ausgangszustand größer werden. Anschließend wachsen die Gleitspuren weiter und reduzieren die Mikrohärte der Austenitkörner. Dies deutet an, dass die zyklische Entfestigung wieder auftritt. Hierbei zeigten die Synchrotronstrahlungsexperimente eine Abnahme der Mikroeigenspannungen. Die zyklische Ver- und Entfestigung des Austenits kann auf Bewegung und Umordnung der Versetzungen zurückgeführt werden, was durch TEM Bilder gestützt wurde.

Die phänomenologischen Beobachtungen an den Proben zeigten zwei Arten von Mikrorissen, intergranulare Mikrorisse tauchen schrittweise von einem sehr frühen bis zu einem relativ späten Stadium auf und transgranulare Mikrorisse initiieren plötzlich. Die Mikrorissbildung kann durch die resultierende Schubspannung $\tau$ an der Phasengrenze interpretiert werden. Diese bestehen aus: 1) Schubspannung $\tau_1$ aufgrund der Akkumulation der Intrusionen und Extrusionen (Gleitung der Versetzungen), 2) Schubspannung $\tau_2$ wegen Versetzungsaufstaus und 3) Schubspannung $\tau_3$ aufgrund der externen Lastspannung. Die drei Komponenten entwickeln sich während der zyklischen Ver- und Entfestigung, und führen dazu, dass sich durch die unterschiedlichen resultierenden Schubspannungen an der Phasengrenze deutliche plastische Verformungen in den Ferritkörnern bilden. Die Schubspannung $\tau_1$ steigt dramatisch während der ersten $10^5$ Zyklen an, was auch aufgrund der Beobachtung des Extrusions-Intrusions-Wachstums erwartet wird. Die Schubspannung $\tau_3$ des Ferrits fällt ab, wenn der Austenit zyklisch verfestigt und es steigt an, wenn der Austenite zyklish entfestigt. Diese Ergebnisse wurden durch in-situ XRD- und in-situ DIC-Experimente erzielt. Die Schubspannung $\tau_2$ ist von den Phasengrenzbedingungen weitgehend abhängig und bestimmt die Morphologie der Mikrorisse. Enthält ein Austenitkorn Gleitspuren, wird die Mikrorissinitiierung in dem benachbarten Ferritkorn von einer der folgenden Bedingungen abhängig: 1) Wenn der Winkel zwischen der Phasengrenze und der ferritischen Oberfläche weniger als 90° beträgt, kann plastische Verformung leicht auftreten, und ein intergranularer Mikroriss entsteht schrittweise. 2) Wenn der Winkel zwischen der Phasengrenze und der ferritischen Oberfläche 90° oder mehr ist, werden die Gleitspuren überwiegend durch die Phasegrenze aufgehalten und es erfolgt keine plastische Verformung. Falls die resultierende Schubspannung ausreichend ist, um die Barrierewirkung überwinden zu können, sind die transgranularen Mikrorisse meist vorhanden. Die Phasengrenzbedingungen wurden durch SEM-Bilder bestätigt, die durch die FIB-Cutting erhalten wurden.

# Abstract

Formation of micro-cracks of a duplex stainless steel (DSS) in the very high cycle fatigue (VHCF) regime was studied and discussed. Several high-resolution techniques were applied to fatigued specimens, identifying the mechanical properties of the DSS and relating them to the mechanisms of the micro-crack initiation. Results acquired from optical microscopy, nanoindentation tests and synchrotron radiation investigations revealed that the austenite phase of the DSS in VHCF exhibits cyclic softening-hardening-softening behaviour. The first cyclic softening takes place during the initial millions of load cycles, where a continuous growth of slip markings and a decrease in micro-hardness were observed. Afterwards, austenite hardens in the tested austenite grains which show a stop in the growth of slip markings and an increase in the micro-hardness. Synchrotron radiation experiments performed at this stage revealed that the internal residual stresses between the two phases increase compared to the initial state. After this period, slip markings in austenite continue to grow and the micro-hardness decreases, indicating the reoccurrence of cyclic softening. The synchrotron radiation experiments executed at this stage showed a decrease in internal residual stresses. The cyclic hardening and softening behaviour of the austenite can be attributed to dislocation motion and rearrangement, and was supported by transmission electron microscopy (TEM) micrographs.

Phenomenological observations applied to the specimens showed two types of micro-cracks: intergranular micro-cracks form continuously from an early to a relatively late stage, and transgranular micro-cracks that initiate suddenly. The formation of these cracks is interpreted by the resultant shear stress $\tau$ at the phase boundary, which consists of 1) shear stress $\tau_1$ due to the accumulation of intrusions and extrusions (slip of dislocations), 2) shear stress $\tau_2$ due to dislocation pile-ups and 3) shear stress $\tau_3$ due to external load stress. The three components evolve during cyclic hardening and cyclic softening processes, yielding different resultant shear stresses and resulting in the formation of distinct plastic deformation in the ferrite grains. The shear stress $\tau_1$ increases dramatically within the initial $10^5$ cycles, which can be expected from the observation of extrusion-intrusion growth. The shear stress $\tau_3$ in ferrite decreases when austenite cyclically hardens, and increases when austenite cyclically softens. These were observed in the results obtained for stress and strain partitioning experiments applying in-situ X-ray diffraction (XRD) and in-situ digital image correlation (DIC) techniques. Importantly, the shear stress $\tau_2$ which is largely dependent on phase boundary orientations determines the morphology of the micro-cracks. On the occasion of an austenitic grain forming slip markings, the formation of micro-cracks in the adjacent ferritic grain will depend on the following conditions. 1) If the angle between the phase boundary and the ferritic surface is less than 90°, plastic deformation easily occurs and intergranular micro-cracks gradually form at the phase boundary. 2) If the angle between the phase boundary and the ferritic surface is greater than or equal to 90°, slip markings are frequently arrested by the phase boundary and no plastic deformation takes place. When the resultant shear stress is large enough to overcome the barrier effect, transgranular micro-cracks are mostly present. These hypotheses were confirmed by scanning electron microscopy (SEM) images acquired with focused ion beam (FIB)-cutting.

# Symbols and abbreviations

## Latin symbols

| | |
|---|---|
| A | Cross section area |
| b | Burgers vector |
| $b$ | Fatigue strength exponent |
| c | Fatigue ductility exponent |
| $c$ | Light speed |
| $C$ | Material parameter |
| $C_v^{sat}$ | Local vacancy concentration |
| $d$ | Lattice spacing |
| $D$ | Grain size |
| $d_0$ | Stress-free lattice spacing |
| $d_\varphi^{hkl}$ | Lattice spacing of (*hkl*) plane in φ direction |
| E | Young’s modulus |
| $E^{hkl}$ | Specific elastic constant |
| $f$ | Volume fraction |
| $f_0$ | Natural frequency |
| $f_w$ | Volume fraction of dislocation walls |
| $G$ | Bulk shear modulus |
| $h$ | Planck’s constant |
| h | Thickness of the glide region |
| $h_a$ | The recovery depth of the indentation |
| $h_c$ | The contact depth of the indentation |
| $h_{max}$ | The maximum depth of the indentation |
| $h_e$ | The elastic displacement of the indentation |

| | |
|---|---|
| $\boldsymbol{h_e}$ | Height of the extrusion |
| $h_r$ | The depth of the residual indentation |
| $k$ | Frictional shear stress |
| $\Delta K$ | Stress intensity factor range |
| $\Delta K_{eff}$ | Effective stress intensity factor range |
| $K_{min}$ | Minimum stress intensity factor |
| $K_{max}$ | Maximum stress intensity factor |
| $K_{res}$ | Stress intensity factor caused by residual stresses |
| $L_{\mathrm{i}}$ | Load sharing index |
| m | Material parameter |
| $m_0$ | Mass of the clamping system (lower part) |
| $m_1$ | Mass of the clamping system (upper part) |
| $N$ | Number of cycles |
| $dN/da$ | Crack growth rate |
| $N_i$ | Number of cycles to crack initiation |
| $N_f$ | Number of cycles to failure |
| $p$ | Ratio of the irreversible strain to the total strain within PSB |
| $P_{max}$ | The maximum load force of the indentation |
| $R$ | Load ratio |
| $R_{eff}$ | Effective load ratio |
| $R_{p0.01}$ | 0.01% proof strength |
| $R_{p0.2}$ | 0.2% proof strength |
| $R_m$ | Tensile strength |
| $S_1^{hkl}$ | X-ray elastic constant depending on interference (*hkl*) and the material phase |

| | |
|---|---|
| $\frac{1}{2}S_2^{hkl}$ | X-ray elastic constant depending on interference (*hkl*) and the material phase |
| $V_f^{\alpha}$ | Volume fraction of ferritic phase |
| $\overline{w}$ | Surface roughness in PSB |
| $w_s$ | Specific fracture energy |

**Greek symbols**

| | |
|---|---|
| $\Delta\varepsilon$ | Total strain range |
| $\Delta\varepsilon_{el}$ | Elastic strain range |
| $\Delta\varepsilon_{\mathrm{pl}}$ | Plastic strain range |
| $\Delta\varepsilon/2$ | Strain amplitude |
| $\varepsilon_f$ | Tensile strain |
| $\varepsilon_f'$ | Fatigue ductility coefficient |
| $\varepsilon_y$ | Strain in y direction |
| $\varepsilon_{VM}$ | Von Mises Strain |
| $\varepsilon_{\varphi}^{hkl}$ | Elastic strain of (*hkl*) plane in φ direction with loading axis |
| $\varepsilon_{\varphi,\psi}^{hkl}$ | Elastic strain of (*hkl*) plane in angles $\psi$ and $\varphi$ |
| $\gamma_{pl,PSB}$ | Local plastic shear strain amplitude in PSB |
| $\Delta\tau$ | Resolved shear stress range |
| $\nu$ | Poisson’s ratio |
| $\nu^{hkl}$ | Specific elastic constant |
| $\sigma$ | True stress |
| $\Delta\sigma/2$ | Stress amplitude |
| $\sigma_{app}$ | Applied stress |
| $< \sigma_I >$ | Mean stress in inclusion |
| $\sigma_m$ | Mean stress amplitude |

| | |
|---|---|
| $< \sigma_M >$ | Mean stress in matrix |
| $< \sigma^{\alpha}_{RD,t} >^{MAX}_{i}$ | Maximum average total stress in ferrite for cycle $i$ |
| $< \sigma^{\alpha}_{RD,t} >^{MIN}_{i}$ | Minimum average total stress in ferrite for cycle $i$ |
| $< \sigma_{RD,M} >^{MAX}_{i}$ | Maximum average macrostress for cycle $i$ |
| $< \sigma_{RD,M} >^{MIN}_{i}$ | Minimum average macrostress for cycle $i$ |
| $\sigma'_f$ | Fatigue strength coefficient |
| $\sigma^{M}_{res}$ | Macro residual stress |
| $\theta$ | Diffraction angle |
| $\Delta\theta$ | Peak shift angle |
| $\lambda$ | Wavelength of X-ray |
| $\delta$ | Kronecker function |
| $\psi$ | Azimuth angle |
| $\varphi$ | Pole angle |
| $\omega_{ij}$ | Transformation matrix |

**Abbreviations**

| | |
|---|---|
| bcc | Body-centred cubic |
| DEC | Diffraction elastic constants |
| DIC | Digital image correlation |
| DSS | Duplex stainless steel |
| EBSD | Electron back-scatter diffraction |
| fcc | Face-centred cubic |
| FIB | Focused ion beam |
| FGA | Fine granular area |
| FWHM | Full width at half maximum |
| HCF | High cycle fatigue |

| | |
|---|---|
| LCF | Low cycle fatigue |
| ODA | Optical dark area |
| PSB | Persistent slip band |
| PSM | Persistent slip marking |
| SEM | Scanning electron microscopy |
| TEM | Transmission electron microscopy |
| VHCF | Very high cycle fatigue |
| XRD | X-ray diffraction |

# 1 Introduction

The word ‘fatigue’ is derived from the Latin ‘fatigare’, meaning ‘to cause to break down’ originally, and ‘to weary, tire out’ later. In engineering terminology, fatigue is a damage accumulation process of structural materials subjected to repeated loading. In the 19th century, catastrophes caused by the failure of railway components encouraged German engineers to begin fatigue testing of various materials. August Wöhler is one of the most well-known early fatigue researchers, who found the fatigue limit of an applied wheel axis steel [1]. His studies led to the development of the so-called ‘Wöhler curve’, which shows the statistical regularity of failure behaviour, characterised as amplitude-life and endurance limit, and is still used today for lifetime calculations of metallic materials. Another useful conceptual tool for practical engineering is the damage tolerance approach. This approach is different from the former conservative principle, where defects such as small cracks can exist in a component, as the principle of this method is mainly to calculate the time for the growth of the crack to a critical value until the material wholly fracture. This concept originates from Irwin’s pioneering contribution in 1957 [2] which introduced a stress intensity factor K to describe the singularity of crack tips. Afterwards, Paris, Gomez and Anderson [3] found that the crack propagation rate is strongly correlated with the range of stress intensity factor ΔK during cyclic loading, which leads to the formation of this concept.

An important observation obtained between the two concepts can be found in Bauschinger’s work [4], which pointed out that metallic materials exhibit different elastic limits when they are under monotonic and cyclic loading conditions. This concept essentially confirms the cyclic responses of metals which are nowadays termed as cyclic hardening and cyclic softening. Motivated by the works of Wöhler and Bauschinger, Ewing and Humphrey [5] presented more convincing reasons for the failure of materials from a microscale perspective with the help of optical microscopy in 1903. Wide slip bands with defined edges originating from slip-lines lead to cracking in some crystals. Results from Thompson, Wadsworth and Louat in 1956 [6] revealed that such slip-lines always emerge at the same position even if a thin surface layer was polished away. The slip traces are therefore known as ‘persistent slip bands’ (PSB).

Investigations carried out more recently, especially in America in the 1970s and 1980s, focused on the range of stress intensity factor ΔK on the crack propagation rate. In 1970, Elber [7] found the cracks keep closure even if the specimens were under cyclic pull-pull conditions, implying that the crack propagation rate may not be dominated by ΔK but rather by the effective values of ΔK. Ritchie, Suresh and Moss [8, 9] proposed the terminology ‘plasticity induced crack closure’ to interpret this phenomenon. In brief, a plastically transformed area is formed at the crack tip which leaves a wake of plastically deformed zone along the crack length. This zone has compressive residual stress induced by the elastic and plastic deformation of the material during unloading. During the next cycle, the crack tip does not open while loading unless the applied load is enough to overcome the compressive residual stress present in the plastic wake zone. On the other hand, in Europe, models on crack initiation prevailed with the utilisation of electron microscopes, examining the intrinsic changes of metals. The EGM model [10] gives detailed knowledge of the dislocation structure of PSB while considering dislocation interactions and vacancy generation. Polák's model [11] later assumed that point defects are supposed to be generated in the whole volume of PSBs, i.e., both in the dislocation-rich wall and in dislocation-poor channels.

Theories have continued to develop as the microstructural complexities in polycrystalline materials have continuously evolved to new grades to improve their mechanical properties for engineering applications. Adjustments of chemical composition in pure crystals lead to different fatigue mechanisms as well. It is until the 20th century, components run for more than $10^7$ cycles did not draw scientists' attention, although the failure of a Cr-Mo steel after $10^8$ fatigue cycles was noted by Naito et al. in 1983 [12]. Traditionally, such components are expected to have an infinite lifetime according to the fatigue limit concept. In 1999, Bathias [13] emphasised that failure rupture can still occur in a large number of alloys even the specimens are under fatigue limit conditions. This requires more care with respect to the choice of alloys and the techniques used in the endurances prediction. Great interest has been developed both in technical and academic aspects; investigations on this aspect have brought about the concept of very high cycle fatigue (VHCF), compared with low cycle fatigue (LCF) and high cycle fatigue (HCF).

Current knowledge of crack initiation in VHCF is that the initiation site changes from the surface to the internal defects where a so-called 'fish eye' fracture morphology forms. For materials without internal defects, fatigue damage accumulates to form persistent slip bands. The roughness of the surface in the form of extrusions and intrusions can act as stress concentration sites, from which cracks form [14]. Due to the complexities of materials used in engineering applications, mechanisms of crack initiation in the VHCF regime must be established. The fatigue conference in 1998, organised by C. Bathias and S. Stanzl-Tschegg in Paris, established key research question in the VHCF field. Afterwards, VHCF fatigue conferences were held almost every three years in different countries (Austria, Japan, USA, Germany and China), motivated by fundamental and practical issues. VHCF behaviour, according to Christ et al. [15], is summarised as below:

- the crack initiation phase emerges extremely late,
- plastic deformation is scarce,
- the plastic deformation distributes heterogeneously,

- the damage evolution is very local,
- stress concentration becomes more important and
- the production history of the materials has significant influence.

With such challenges, the priority program 'Life$^{\infty}$' SPP 1466, financially supported by 'Deutsche Forschungsgemeinschaft (DFG)' came into being, with the aim of successfully exploring the mechanisms of VHCF specific to damage evolution, crack initiation and propagation together with considering the influence of microstructure, ambient and testing methods. The current study is a subset of this framework, in partnership with the Solid State Physics Siegen, Mechanics Institute Siegen, Hochschule Osnabrück and European Synchrotron Radiation Facility (Grenoble, France), to investigate the VHCF behaviour of the duplex stainless steel 1.4462 (German designation).

Duplex stainless steels (DSSs) possess a comparable volume fraction of austenite and ferrite, and have found application in the offshore, nuclear, oil, and petrochemical industries. The austenitic phase in duplex steels improves the corrosion resistance, while the ferritic phase promotes the mechanical properties. The complexities of the fatigue behaviour of the duplex steel are: I) different elastic and plastic properties of the two phases, II) inhomogeneous microstructures with different crystal structures (fcc and bcc), III) crystallographic orientation of each grain, IV) topography and V) barriers strength (twin, grain and phase boundaries). As Christ addressed, the production history also affects the fatigue response. The processes of heat treatment of the DSS, annealing at high temperature and quenching in cold water, result in substantial residual stresses between the two phases due to the different thermal expansion coefficients. This is the prime motivation of the present work with an emphasis on the effect of residual stresses on crack initiation in the VHCF regime. The construction and objectives of this research program are listed as follows:

- Fatigue behaviour of metallic materials and basic knowledge about DSSs are reviewed in chapter 2. The experimental techniques employed to achieve the objectives are described in chapter 3.
- In the first section of chapter 4, regularities of residual stress development in VHCF and HCF were characterised by means of high energy synchrotron radiation and conventional laboratory X-ray diffraction. Dislocation structures were investigated through transmission electron microscopy (TEM), and the differences interpreted.
- In the second section of chapter 4, damage evolution was systematically investigated with respect to the formation of slip markings, characterisation of micro-hardness, variation of dislocation densities and observation of micro-cracks, identifying the fatigue response of the DSS in the VHCF regime.

- In the next two sections of chapter 4, experiments on strain and stress distribution were determined by means of in-situ X-ray diffraction (XRD) and in-situ digital image correlation (DIC), respectively, confirming the significance of stress concentration on crack initiation of the two-phase steel. On the basis of these experimental findings, modelling of the crack initiation is performed in the last section of chapter 4.
- Emphasis on cyclic hardening and cyclic softening of the austenitic phase (leading to residual stress redistribution), and on crack initiation combined with other experimental findings, are demonstrated in chapter 5. Finally, the concluding remarks and scope of future research are given in chapter 6.

# 2 Technical background and literature review

This chapter summarises the basic theoretical background and scope of the present research. Fatigue behaviour of metallic materials specific to cyclic deformation behaviour and crack initiation mechanisms in LCF, HCF and VHCF are reviewed in section 2.1. Physical and mechanical properties of DSSs are described in the first part of section 2.2. Emphasis on residual stress existing uniquely in two-phase alloys and its influence on load sharing are given in the following two parts of section 2.2.

## 2.1 Fatigue behaviour of metallic materials

Fatigue behaviour of metallic materials can cover a wide scope of behavior depending on the loading condition and surrounding environment. Fracture resulting from temperature variations causing cyclic stresses in a structure is termed as thermal fatigue. When coupled with mechanical loading to subject the structures to out-of-phase or in-phase loading, it is termed as thermal-mechanical fatigue. Corrosion fatigue describes structures subjected to cyclic stress loading combined with corrosive conditions. Mechanical cyclic loading carried out with prolonged holding times at high temperature is called creep-fatigue. Fretting fatigue results from fluctuating stresses along with oscillatory relative motion and frictional sliding between surfaces [16]. In this section, the reviewed literature focuses only on mechanical fatigue behaviour, considering the research goals of this study. Additionally, fatigue responses of materials composed of fcc, bcc or a combination of the two are considered only according to the material used.

### 2.1.1 Cyclic deformation behaviour

Fatigue damage caused by cyclic loading actually results from the irreversible movement of dislocations. Dislocations that glide on specific crystallographic planes are called slip planes, on which the directions glide along are termed as slip directions. A general requirement is that the slip planes and slip directions are most densely packed, which lowers the shear stress for atomic displacement. The slip planes and slip directions together are called slip systems. For fcc structures, slip occurs on the {111} octahedral planes and $<1\bar{1}0>$ close-packed directions. Given the permutations of the slip plane types and direction types, fcc crystals have 12 slip systems (4 slip planes × 3 slip directions). Bcc, unlike fcc structures, has no truly close-packed planes. Slip commonly takes place on the highest atomic packing plane {110} and relatively high atomic packing planes {112} {123}; the slip direction is always $<1\bar{1}1>$. There are 48 slip systems in total for bcc crystals.

Under cyclic load conditions, dislocations in the activated slip systems glide irreversibly. Dislocations with opposite Burgers vectors approaching each other within a certain distance of separation causes annihilation. Fig. 2.1.1 shows a schematic diagram of the annihilation process for screw and edge dislocations.

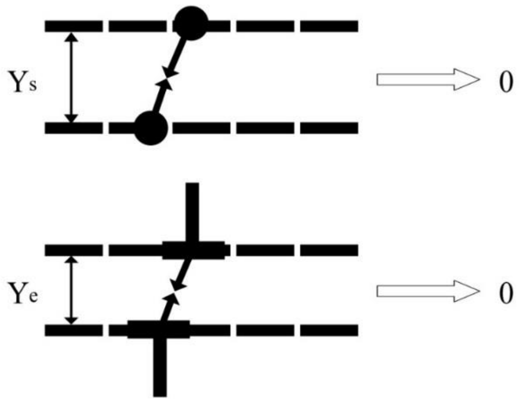

**Fig. 2.1.1:** Schematic diagram showing annihilation processes for screw (upper) and edge (lower) dislocations, $Y_s$ and $Y_e$ are the critical distances for screw and edge dislocations, respectively [17].

When the distance between the two dislocations is greater than the critical distance, they can form a stable configuration known as a dipole in the form of vacancy or interstitial type configuration. Fig. 2.1.2 shows a schematic of a dipole structure.

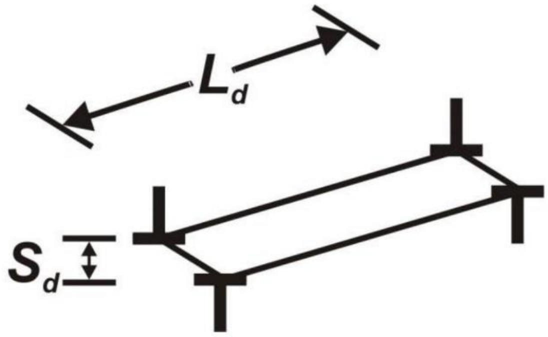

**Fig. 2.1.2:** Schematic diagram of a dipole structure [17].

Since screw dislocations can easily annihilate during cross-slip, dipole configurations are only composed of edge dislocations. They do not move as a whole but reconfigure themselves slightly when the external or internal stresses are changed. A dipole is not a representation of the alignment of two dislocations with opposite Burger vectors. The angle between two dislocations in a dipole lies between 25° and 65°, with an average around 45° [18]. The latter angle represents the position of minimum interaction energy of dislocations within dipoles. When two dislocations without opposite Burgers vectors approach with each other, one of the following three events can take place: 1) they lock together, forming a Lomer-Cottrell barrier, 2) they draw each other, forming a jog intersection or 3) they intersect and pass each other [19].

Annihilation also occurs when dislocations glide to free surface, leaving behind step structures composed of Burger vectors. With continuous cyclic loading, the step structures keep growing as a consequence of increasing the dislocation dipoles, and so-called persistent slip bands (PSB) finally come into being. The PSBs inside are likely ladder structures which consist of closely arranged edge dislocations enclosed by a nearly dislocation-free zone. The surface part of a PSB consisting of extrusions and intrusions is called a persistent slip marking (PSM) which manifests persistent irreversible slip activity localised within PSBs. According to Essmann [10] and Man [20], the whole structure can be schematically drawn as follows:

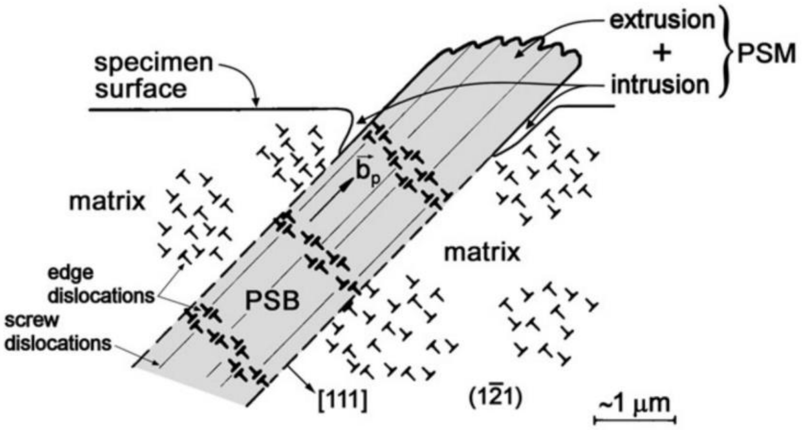

**Fig. 2.1.3:** Section through the grain showing surface profile of mature PSM formed at the side where the PSB intersects the free surface [20].

PSBs manifest the plastic deformation of a material and its surface. In LCF, strong PSBs are relatively homogeneously distributed in all grains. HCF results in a fraction of favourably oriented grains with PSBs. The PSBs reveal irreversible plastic deformations during cyclic loading. In VHCF, the plastic deformations are characterised as PSM showing irreversible cyclic slip as well. Examinations of the irreversible cyclic slip has been carried out both in physical and mathematical aspects, and can be attributed to the following reasons [17]:

- Slip displacement during unloading cycles is less than during loading cycles due to the absorption of an embrittling species or due to the oxidation of slip steps,
- Random distribution of slip (independent of prior history) with the progressive preferential deepening of valleys at the surface,
- Cross slip of screw dislocations and different paths for their forward and reverse glide during complete fatigue cycles,
- The extrusions, with a triangular cross section, grow at rate of 1–10 nm/cycle, whereas the protrusions are an order of magnitude slower,
- Dislocation-dislocation interactions lead to the formation of nodes, jogs or dislocation locks which impede motion during part of a fatigue cycle,
- Production of point defects during saturation due to the dynamic equilibrium between dislocation

generation and annihilation, and,

- Irreversibility due to sharp changes as well as differences in dislocation back stress due to slip on different glide planes during the tension and compression portions of fatigue.

Due to cyclic loading, not only can annihilation of dislocations occur, but multiplication can take place. During dislocation motion, multiplication occurs by pinning of the dislocation, bowing out and wrapping around the pinning points. This is also known as the Frank-Read mechanism, depicted in Fig. 2.1.4.

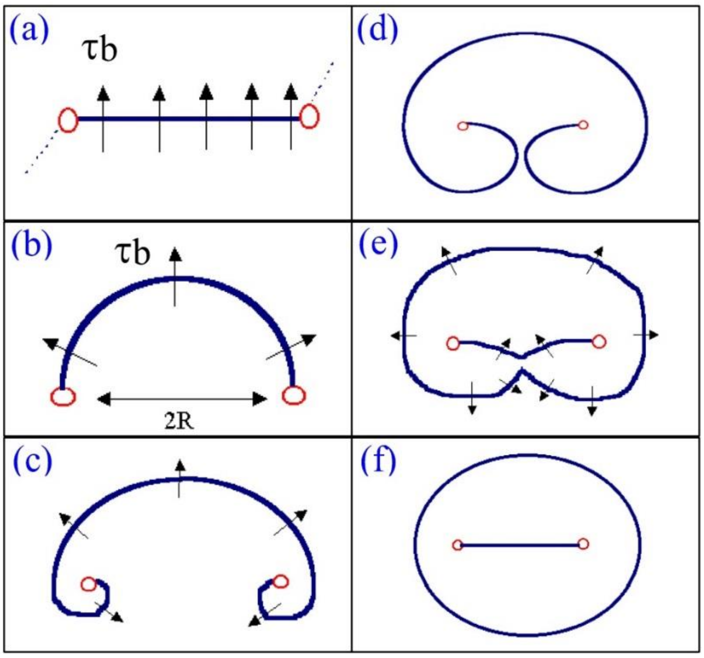

**Fig. 2.1.4:** Schematic diagram showing the dislocation multiplication process; a) pinned ends and dislocation line with shear stress, b) dislocation bows out, c) dislocation spontaneously grows, d) two opposite segments meet and annihilate, e) loop and segment separate and d) loop expands and dislocation line straightens.

As described previously, cyclic loading can lead to dislocation annihilation and dislocation generation. However, the whole process is actually dominated by the accumulation of dislocations. Newly generated dislocations arrange themselves to form dislocation networks. In cyclic loading with high strain amplitudes (LCF), dislocations are identified as either band and channel structures or cell structures with considerable cell disorientation. In cyclic loading with low strain amplitude (HCF), loop path structures or vein and channel structures are the most representive. In VHCF, the variation of dislocation density is scarce owing to the low-stress amplitude. Only a few grains with preferential orientations can be triggered. Dislocations generate from the Frank-Read source and grow within the slip plane until hindered by barriers such as grain boundaries or phase boundaries.

Dislocation structures reveal the natural response of materials and should be systematically investigated. Fig. 2.1.5 shows a map of typical dislocation structures of fcc materials as a function of different plastic strain ranges ($\Delta\varepsilon_{pl}$) as well as number of cycles to failure ($N_f$) and the slip character of the material. It also gives TEM micrographs of cell structures in LCF, dipoles or dipole bundles in HCF and planar arrangements in VHCF.

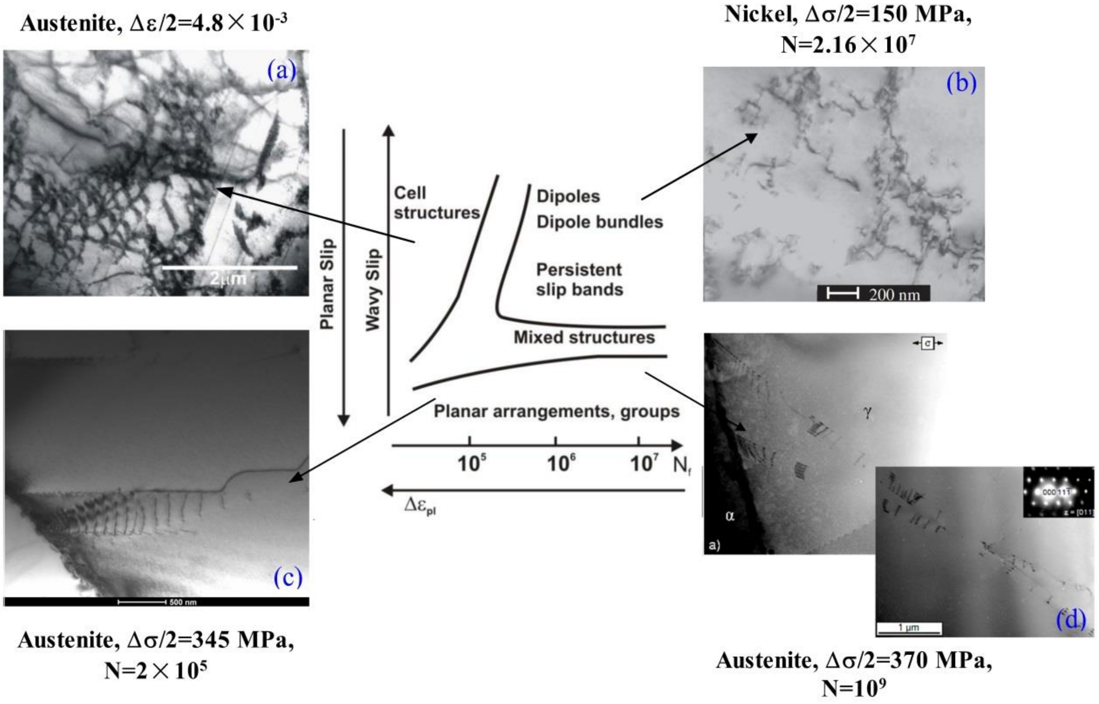

**Fig. 2.1.5:** Different dislocation structures as a function of slip model, plastic strain amplitude and cyclic life. The TEM micrograph in (c) is from the present work. (a), (b) and (d) are from [16, 21, 22], respectively.

The development of dislocation density and variation of dislocation arrangement result in changing of the mechanical response, e.g., the hysteresis loop. This is known as cyclic hardening or cyclic softening, depending on how the shape changes and the test conditions (stress or strain). Components subjected to a constant amplitude, fully reversed stress control, cyclic hardening or cyclic softening of the material features a reduced or an increased axial strain amplitude. Similarly, under constant amplitude, strain-controlled fatigue loading, cyclic hardening or softening of the material causes an increase or decrease, respectively, in the axial stress amplitude. Fig. 2.1.6 gives an example of cyclic hardening and cyclic softening responses under strain control conditions.

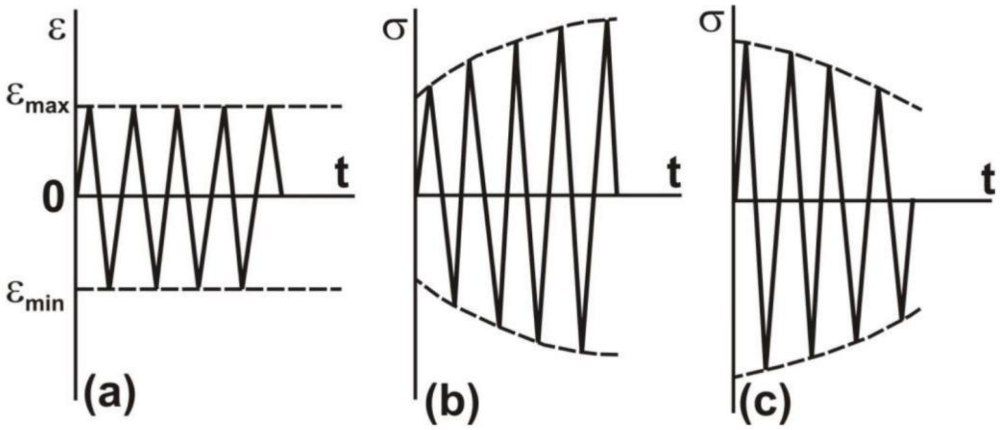

**Fig. 2.1.6:** Cyclic hardening and cyclic softening of a material, a) constant amplitude strain cycling, b) cyclic hardening and c) cyclic softening [16].

The resulting stress amplitude values in Fig. 2.1.6 are registered as a function of the number of cycles to characterise the cyclic hardening or cyclic softening. Fig. 2.1.7 shows a schematic representation of the variation of uncontrolled stress with an increase in the number of cycles. The cyclic deformation curve can be divided into three stages. The cyclic hardening/softening (depending on the pre-treatment of the material, such as deformation, or annealing) is followed by a plateau of cyclic saturation. In the end, there is an inhomogeneous deformation of the dominant macrocrack, which finally leads to failure of the specimen.

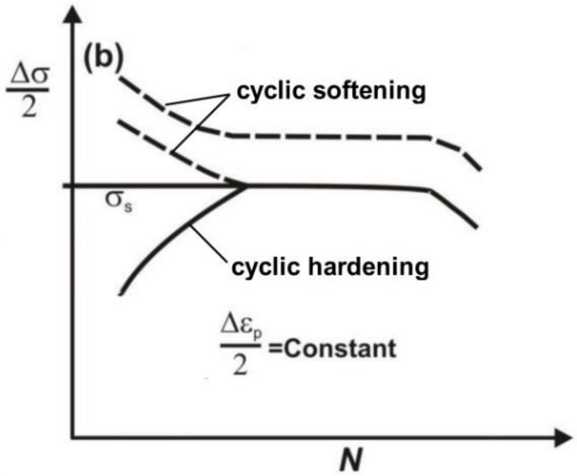

**Fig. 2.1.7:** Cyclic deformation curves.

In LCF and HCF, cyclic hardening and cyclic softening effects are evident, while in VHCF such mechanical behaviour is scarce as the hysteresis loops are almost linear. Thus, higher resolution techniques are required to test the cyclic hardening and cyclic softening behaviour in VHCF.

### 2.1.2 Crack initiation mechanisms

In this section, theoretical models of crack initiation established in the 1980s, with the aim of explaining the formation of cracks in LCF and HCF, are briefly reviewed. Afterwards, models developed in recent years for VHCF are summarised as well.

**Model of Brown and co-workers**

Antonopoulos et al. [23], based on the experimental findings that dipole density in the walls of PSBs is much larger than in the matrix, assumed that the whole PSB experiences an internal macroscopic tensile stress in the direction of the primary Burgers vector. The internal stress, corresponding to an elastic tensile strain of about $2\times10^{-4}$, leads to logarithmic infinite stress at the interface between the PSB and matrix, marked in Fig. 2.1.8 as point A and point B. Location A is in compression (crack closing), while location B (crack opening) is in tension. The unevenly distributed stress gives rise to the first crack initiation at point B.

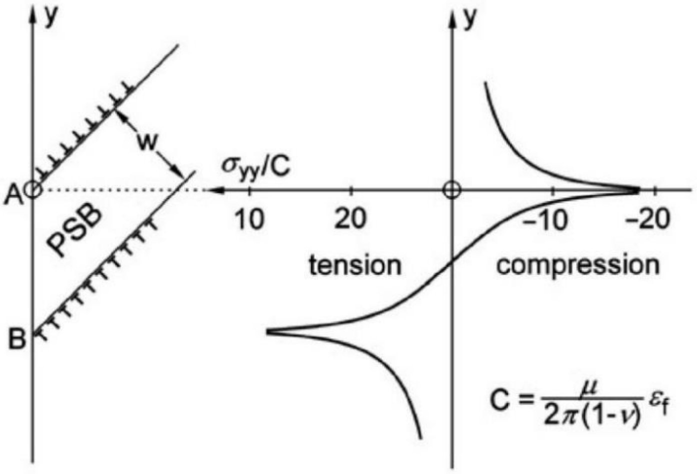

**Fig. 2.1.8:** Schematic of the model of Brown and co-workers showing surface stresses at the intersection of the PSB with the free surface [24].

Brown and Nabarro [25] expanded upon this model according to the complexity of the formation of an extrusion on the surface and the Basinski criticisms [26]. Energy differences between vacancy and interstitial dipoles of equal height leads to conversion of interstitial dipoles to vacancy dipoles by slipping, resulting in the formation of extrusions at the crystal surface. The height of the extrusion, as described in [27], is given by the tensile strain $\varepsilon_f$ multiplied by the length of the PSB. For a given polycrystal with grain size D, the height of extrusion can be written as:

$$h_e = D\varepsilon_f \tag{2.1}$$

This proportionality is in qualitative agreement with experimental findings. However, it is only valid during early rapid growth but not with heights within fatigue life according to Polák et al. [28].

**Vacancy models**

The EGM model [10] offers detailed knowledge of the actual dislocation structure of PSB. It is a semi-quantitative model in consideration of dislocation interactions and vacancy generation to form the dislocation structure PSB. In this model, the surface profile at the emerging PSB is composed of two stages: 1) the rapid formation of a static extrusion and 2) the slow gradual evolution of surface roughness by random irreversible slip [20].

The glide and annihilation of edge dislocations within the walls of PSBs lead to vacancy-type defects in the PSBs and to the deposition of so-called ‘interface’ dislocations at opposite PSB-matrix interfaces, as shown in Fig. 2.1.9(a). This is contrary to the model of Brown and co-workers, in that extra half planes of interface dislocations are inserted into the PSB (in comparison with Fig. 2.1.8), resulting in compressive stress along the PSB lamella. Under symmetric pull-push load conditions, the interface dislocations glide out at opposite side of PSBs. In the tensile phase, glide occurs at locations $A$ and $A'$, while in the compressive phase, the glide takes place at locations $B$ and $B'$, as shown in Fig. 2.1.9(b). This leads to the formation of ribbon-like extrusions, in accordance with the experimental results for single crystals. In the EGM model, the height of the static extrusions follows the fact that there will be a volume expansion of the PSB lamella, originating from the local vacancy concentration $C_v^{sat}$ attained in cyclic saturation in the dislocation walls where the annihilations take place. Taking into consideration the volume fraction of walls $f_w \approx 0.1$ and $C_v^{sat}$ being approximately $6\times10^{-3}$, the mean vacancy concentration over the entire PSB would be $f_w \cdot C_v^{sat} \approx 6\times10^{-4}$ [29]. The volume change of PSB lamella caused by a one-dimensional elongation of the PSB in the direction of Burgers vector **b** leads to the height of the static extrusion as:

$$\boldsymbol{h_e} \approx 0.5 C_v^{sat} \cdot f_w \approx 3 \times 10^{-4} D \tag{2.2}$$

where D is the specimen diameter measured in direction of the Burgers vector for a single crystal and grain size for a polycrystal. It is therefore inferred that extrusions in polycrystals would be smaller than in single crystals as the grain size is always much smaller than the specimen diameter.

It is anticipated that there will be a slower continuous extrusion growth after the static extrusions have been formed. Vacancies lost to the PSB by diffusion to the matrix are replaced by the glide and annihilation, whereby the PSB-matrix interfacial dislocations continuously generate. This leads to gradual roughening of the surface of the material, as shown in Fig. 2.1.9(c). Surface roughness in the PSB $\overline{w}$ can be estimated by the following equation:

$$\overline{w} \approx \sqrt{6bphN\gamma_{pl,PSB}} \tag{2.3}$$

where $h$ represents the thickness of the glide region, $N$ is the age of the PSB, $p$ is the ratio of the irreversible strain to the total strain within the PSB, and $\gamma_{pl,PSB}$ is the local plastic shear strain amplitude in the PSB. Two distinct types of stress raisers are indicated in Fig. 2.1.9(c). Type I forms early at the PSB-matrix interface, while type II develops gradually as previously discussed. These propositions are in great agreement with the experimental findings in single crystals and partially in polycrystals.

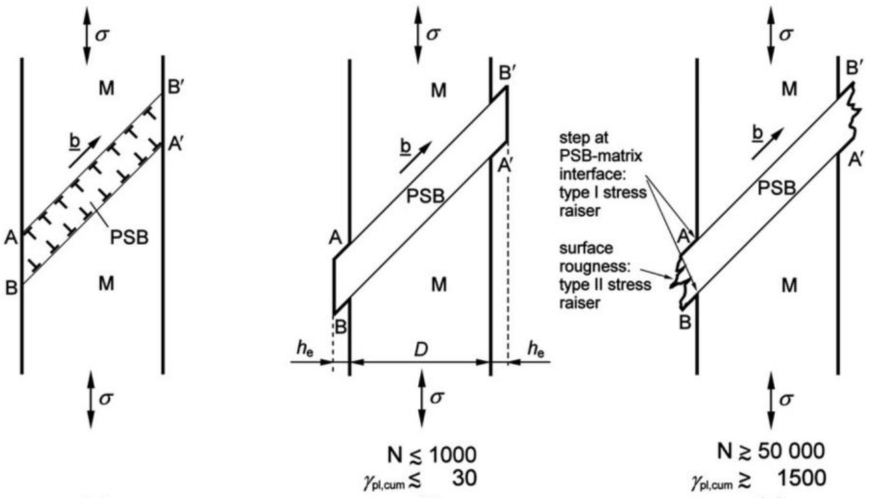

(a) (b) (c)

**Fig. 2.1.9:** PSB surface formation according to the EGM model: a) accumulation of interface dislocation, b) rapid formation of static extrusion and c) slowing roughening of the PSB profile. Reproduced from [20].

Based on the EGM model, Polák [30] developed a modified vision with the consideration that point defects are supposed to be generated in the whole PSB, namely in both dislocation-rich walls and dislocation-poor channels. The generation rate of point defects (vacancies) is relatively homogeneous within the PSB, while the annihilation rate is a function of sink density. Mobile vacancies annihilate when approaching sinks. As edge dislocations and edge dipoles act as perfect sinks and arrange themselves more frequently in the walls than in the channels, a quasi-equilibrium vacancy concentration in between can be caused by the generation and annihilation during fatigue cycling. The vacancy density reaches a maximum in the middle of the channels and decrease gradually towards the walls and the matrix (see sections $A - A'$ and $B - B'$ in Fig. 2.1.10(a)). The concentration gradients lead to a systematic flux of vacancies from the channels to the walls and/or matrix, resulting in mass changes due to the exchange between vacancies and atoms. Compressive and tensile stress, built up due to mass distribution, can only be released in the y-direction, leading to the steady growth of the ribbon-like extrusion as depicted in Fig. 2.1.10(b). Due to the mass reduction close to the PSB-matrix interfaces, the tensile macroscopic stresses arise and are relaxed by the formation of intrusions. The intrusions are believed to be crack initiation sites as stress concentration accumulates on these sites due to the smaller radius, compared with extrusions.

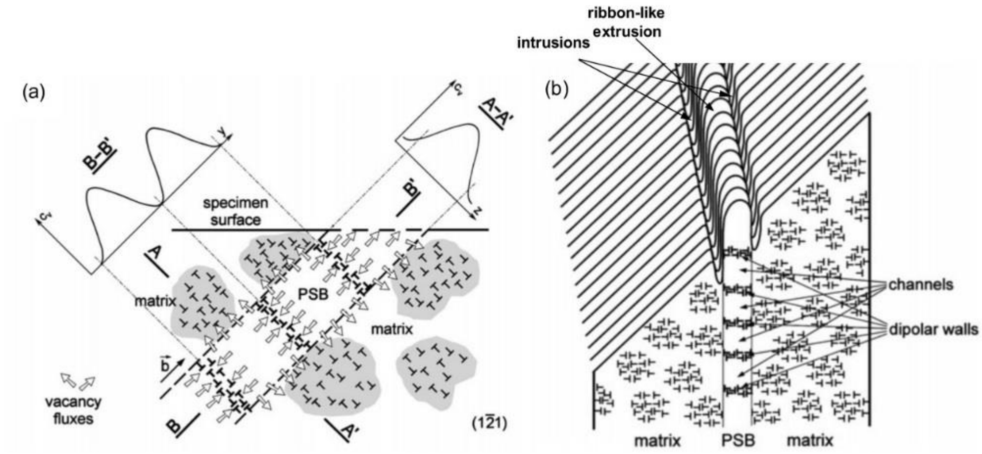

**Fig. 2.1.10:** Polák's model showing a) vacancy flux from the channels to the walls and/or matrix and b) surface profile of intrusions and ribbon-like extrusions. Reproduced from [20].

On the basis of TEM and scanning electron microscopy (SEM) investigations, Hsiung and Stoloff [31] observed vacancy clusters beneath the surface of $Ni_3Al$+B single crystals fatigued at room temperature. They suggested that lattice misfits develop between the PSB and the matrix, which are believed to increase with the accumulation of plastic strain. The vacancy clusters at the interface between the PSB and the matrix lead to the formation of micro voids (micro-cracks). This model, however, does not show the surface roughness (formation of intrusion and extrusion) and is limited to $Ni_3Al$ single crystals in which no PSBs with ladder structure have been observed.

**Tanaka-Mura's model**

Dislocation accumulation alternating between two parallel closely located layers during cyclic loading is the basic idea of this model. The build-up of dislocation dipoles piled up against barriers (grain or phase boundary) is the main reason for extrusion and intrusion.

In this model, a favourably oriented grain is considered on the surface, i.e., the slip plane and the slip direction have an angle of 45° with the loading axis. There are three isolated individual PSBs within this grain, as shown in Fig. 2.1.11(a). Dislocations are generated on the surface of the specimen and move along the slip direction to the interior. With continuous loading, dislocation pile-ups with a positive sign appear on layers I, the reverse flow causes dislocation pile-ups with a negative sign showing on the neighbour layers II. The ratchet deformation is intensified by back stress due to the previous segment of the loading cycle. The dislocation dipoles or vacancies are then accumulated, resulting in monotonic build-up of intrusions or extrusions. Tanaka and Mura proposed [32] two ways for the crack configuration shown in Figs. 2.1.11(b) and (c). In the case of extrusions, embryonic cracks are formed at the phase boundary within a surface grain due to the pile-up of vacancy dipoles. Intrusions acting as stress concentration sites on the surface are considered as crack embryos.

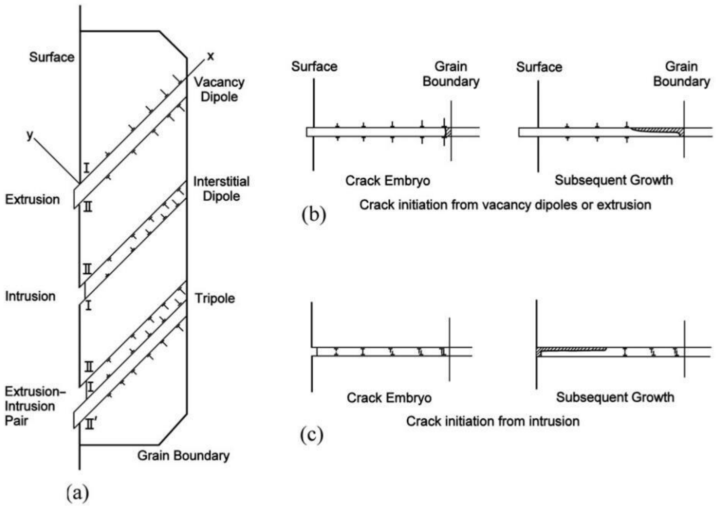

**Fig. 2.1.11:** Tanaka-Mura's model showing a) PSBs with accumulated dislocation pile-ups at the grain boundary, b) crack initiation from vacancy dipoles or extrusion and c) crack initiation from intrusion [32].

Tanaka and Mura took the stored strain energy, caused by dislocation accumulation, into consideration to describe the relationship between fatigue crack initiation and number of cycles:

$$N_i = \frac{4Gw_s}{(\Delta\tau-2k)^2\pi(1-\nu)d} \tag{2.4}$$

here $G$ is the bulk shear modulus, $w_s$ is the specific fracture energy, $\Delta\tau$ is the resolved shear stress range, $k$ is the frictional shear stress, $\nu$ is Poisson's ratio and $d$ is the grain size.

Tanaka-Mura's model is attractive in that it gives a quantitative evaluation of the crack nucleation life with some experimental parameters. This model has been used to successfully describe crack initiation and early crack growth in LCF and HCF for some materials. However, according to Man [20], the criticisms for this model lie in:

- The mechanism of crack nucleation for extrusion (Fig. 2.1.11(b)) can hardly be reconciled with the experimental data as the fatigue cracks start at the surface in the vicinity of extrusions but not beneath the specimen surface at the grain boundary.
- The model is not applicable to polycrystals where immobile obstacles are present. It is thus not capable of explaining the surface relief formation and fatigue crack nucleation in pure, notch-free single crystals.

**Other models**

The model of Zhai et al. [33, 34] suggested that there will be a great number of vacancies in the PSB as the walls of the PSB may collapse due to the combination of tensile internal stress and applied stress. As a consequence, the vacancies aggregate to form micro-cracks within and perpendicular to the individual PSB and/or micro voids near the surface region. Although this model is in consideration of the real dislocation structure of PSB, it does not regard the dynamic equilibrium between multiplication and annihilation of screw and edge dislocations within a PSB.

Lin and co-workers [35] proposed a micromechanical model for crack initiation. The extrusions and intrusions are driven by alternating specific micro-stress fields in the PSB during cyclic loading. The prediction by this model for extrusion growth is in a good agreement with the experimental findings. However, it cannot explain the simultaneous growth of extrusions and intrusion as in Lin's model, where the formation of extrusions and intrusions depends on the sign of the stress field.

In contrast to vacancy models, Basinski and Basinski [36] addressed that there is no correlation between persistent slip markings and vacancy mobility after an extensive investigation of observing PSM profiles in single crystalline copper fatigued at different temperatures. They suggested that the slip in secondary slip systems with Burgers vectors lying in the cross glide plane may be the reason for the observed macro PSM profiles. This fits experiments carried out at 4.2–350 K, but fails to explain how it is responsible for the temperature change in macro PSB profiles, based on observations at 15 K.

**Models for VHCF**

As outlined previously, fatigue behaviour of metallic materials in VHCF has attracted scientists' attention in the year since Bathias [13] stated there is no fatigue limit for metals. Afterwards, investigations on VHCF are thriving with the intention of both settling the practice issues and exploring the theoretical mechanisms involved. Now, acceptances on VHCF are the duplex- or multi-stage S-N diagram and crack initiation models for different kinds of materials. Type I materials are those with no extrinsic internal defects, while type II materials are materials containing internal defects. The internal defects correspond to the non-metallic inclusions and pores, excluding the second phase, precipitates, and intermetallic particles. Mughrabi [37, 38] emphasised that in HCF, fatigue crack initiation becomes more and more important at larger fatigue lives relative to propagation, and thus determines the lifetime. It appears that much more attention should be paid to crack initiation in VHCF. Here, mechanisms on crack initiation will be classified into two groups, for type I and type II materials.

**Type I materials**

Mughrabi [14] suggested a multistage fatigue life diagram with four different regions for type I material, as depicted in Fig. 2.1.12. Region I is the traditional LCF range which can be explained by the Manson-Coffin-law. Region II is the PSB dominated plateau where dislocation walls and dislocation-free channels come into being within the system. On the surface, roughness in terms of extrusions and intrusions acts as stress concentration, from which cracks initiate. Region III is the transition from the HCF limit to the VHCF range and region IV is the irreversibility threshold corresponding to the VHCF limit.

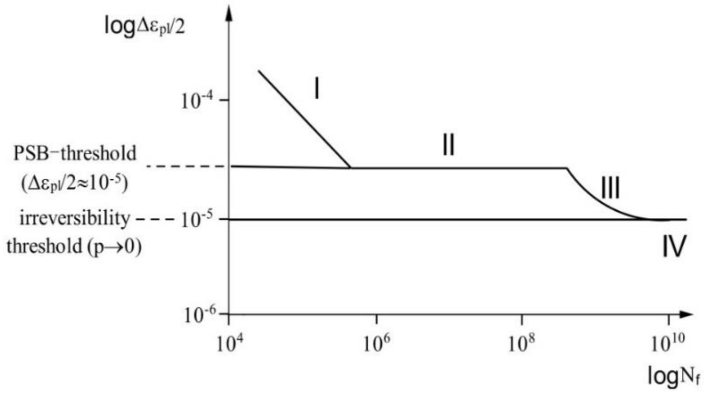

**Fig. 2.1.12:** Schematic multistage fatigue life diagram for type I materials [14].

Regarding the crack initiation mechanism of type I materials, Mughrabi [14] suggested that when a critical surface state is reached, some valleys in the roughness profile act as stress raisers resulting in local stress exceeding the PSB threshold value, leading to embryonic PSBs, as indicated in Fig. 2.1.13. Such a PSB will only grow into a modest depth of the material. However, the notch-peak surface profile at the PSB site is expected to grow deeper as the cyclic strain localises in the PSB with increasing cycle number. Finally, region I fatigue cracks initiate. At present, there are no direct experimental findings to verify this model. However, in copper polycrystals cyclic fatigued below the PSB threshold up to $10^8$, an unusual type of persistent slip occurs (found after etching). Moreover, in the stress field of a notch, PSB formation and crack initiation/growth were observed. It is thus desirable and worthwhile to study this model in further detail.

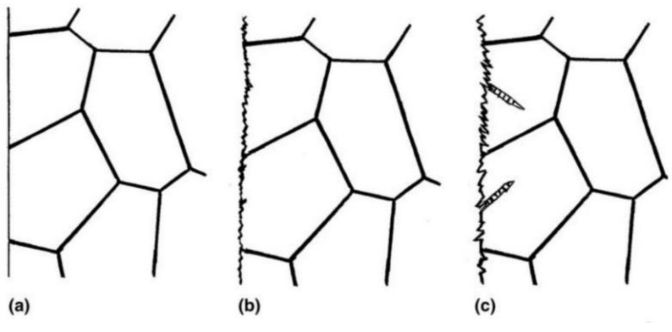

**Fig. 2.1.13:** Schematic illustration of crack initiation for type I materials [14]: a) initial state, b) early stage of surface roughening and c) PSB formation at a later stage.

**Type II materials**

A typical S-N diagram for type II materials is shown in Fig. 2.1.14. In region I, fatigue failures are initiated at the surface. The conventional HCF fatigue limit (region II) extends to the VHCF (region III) region where cracks initiate from internal defects. So far, the existence of region IV is in dispute.

A real fatigue limit can be expected because the extent of the irreversible strain decreases with loading amplitude.

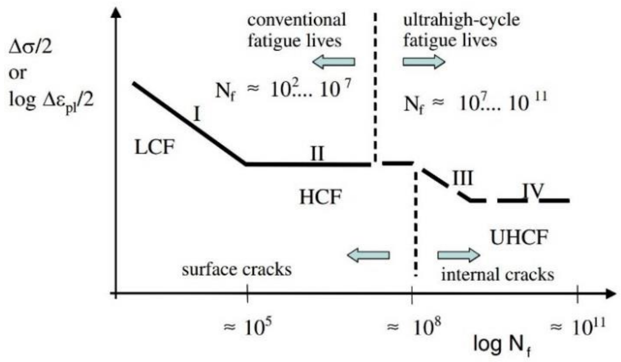

**Fig. 2.1.14:** Double S-N curve for type II materials containing inclusions [39].

In reality however, the S-N curve for type II materials is much more diverse. The S-N curve of low-strength steel Ck15 showed a true fatigue limit. No failure was found even if the specimens ran for $10^{10}$ fatigue load cycles [40]. A decrease in fatigue strength, containing two different slopes, was observed in materials with fcc and bcc lattice structure under corrosive or high-temperature conditions [41]. In investigations on some materials under rotating bending conditions, a plateau below the traditional fatigue limit was found at a higher number of cycles [42]. Some materials under axial tension-compression loading show a continuously decreasing S-N curve as well [43]. The diversity of S-N curves was summarised in [44].

Murakami et al. [45, 46] investigated a large number of high-strength steels in the VHCF regime and found that cracks always initiate from the non-metallic inclusions inside of the specimen. Frequently, an optical dark area (ODA) around the inclusion, in comparison to its surroundings, can be observed on the fracture surface. This is attributed to the interaction of hydrogen embrittlement and cyclic damage, as depicted in Fig. 2.1.15.

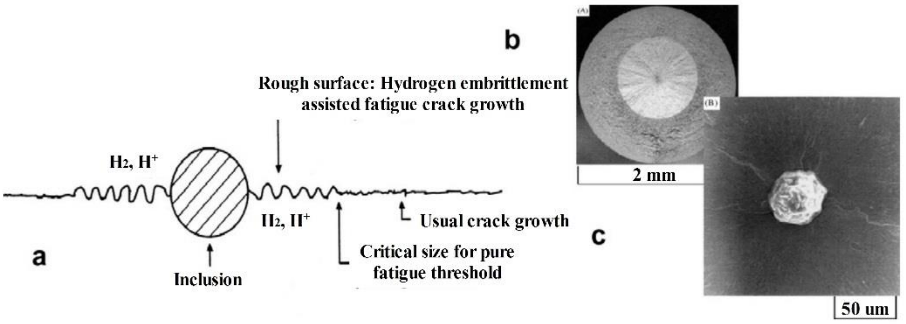

**Fig. 2.1.15:** Murakami's model [45] of crack initiation for type II materials: a) interaction of the hydrogen embrittlement and cyclic damage, b) overview of the ODA and c) close view of the ODA showing non-metallic inclusion inside. The figures are from [44].

Murakami and Endo [47] developed a statistical approach, considering the volume density, size and location of the inclusions. According to this model, the fatigue limit $\sigma_{FL}$ can be calculated as:

$$\sigma_{FL} = \frac{C(HV+120)}{\sqrt{(A)}^{1/6}} \left(\frac{1-R}{2}\right)^{\alpha} \tag{2.5}$$

where $HV$ is the Vikers hardness, $\alpha$ is a hardness-dependent exponent ($\alpha$=0.226+$HV \cdot 10^{-4}$), $R$ is the stress ratio, $A$ is the cross section area of the inclusion, and $C$ is a constant with the value of 1.43, 1.56, 1.41 for an inclusion at the surface, underneath the surface or within the bulk, respectively.

Sakai [48] found a fine granular area (FGA) around the inclusion which can be explained with another model of the failure mechanism. It is divided into three stages. In stage I, a fine granular layer is gradually formed around the interior inclusion. Stage II is identified by nucleation and coalescence of the micro-debonding. Finally, stage III corresponds to the micro-debonding spreading over and forming the FGA around the inclusion.

## 2.2 Duplex stainless steels

DSSs consisting of comparable volume fractions of two phases are finding increased use as structural materials exposed to aggressive environments. Recently, much effort has been devoted to producing DSSs with an advantageous cost/performance ratio. As a result, DSSs in a combination of excellent mechanical properties and corrosion resistance have been established as standard materials in a wide range of industrial sectors such as in chemical industries, oil and gas sectors, paper and pulp industries, offshore, paper production and pollution control equipment [49].

Such DSSs consist of a ferrite matrix with islands of austenite or vice versa. Chromium weight content is owned by 22–26% and nickel exists in a narrow range of weight content of 4–7% exhibiting stainless properties. Typical representatives of these DSSs are designed to have a microstructure in the annealed condition consisting of approximately equal portions of austenite and ferrite.

In this section, basic properties of DSSs and their influencing factors are summarised. In particular, the fundamentals of residual stresses always existing in duplex steels are demonstrated. Lastly, the unique phenomenon load sharing between the two phases present in duplex-phase alloys is given with the aim of identifying the influence of load partitioning on crack initiation in the duplex steel used in this study.

### 2.2.1 Physical and mechanical properties

The physical properties of duplex steels can be predicted from single-phase austenitic and ferritic stainless steels, as can be seen in Table 2.2.1. The Young's modulus is highest for the ferritic steel, approximately 220 GPa. The austenitic steels, however, exhibit higher density and electrical resistivity which is correlated with the high level of alloying elements. Thermal expansions in austenitic steels are likewise higher, which may cause thermal stresses in the application during heat treatment and welding. With regards to these covered properties, duplex steels exhibit intermediate values but are closer to those in ferritic steels.

**Table 2.2.1:** Physical properties for various types of stainless steels [50]:

| Property | Type of stainless steel | | |
|---|---|---|---|
| | Austenitic | Ferritic | Austenitic-Ferritic |
| Density (g/cm$^3$) | 7.9-8.2 | 7.6-7.8 | 7.7-7.8 |
| Young's modulus (GPa) | 195 | 220 | 200 |
| Thermal expansion (×10$^{-6}$/°C) | 17-19 | 12-13 | 13 |
| Thermal conductivity (W/m°C) 20 °C | 12-15 | 20-23 | 20 |
| Heat capacity (J/kg°C) 20 °C | 440 | 460 | 440-460 |
| Resistivity (nΩm) 20 °C | 850 | 600-750 | 700-850 |
| Ferromagnetism | No | Yes | Yes |

The mechanical properties of the duplex steels are dependent on the element composition, phase and grain arrangement as well as texture, which will be discussed in the following.

**Influence of element composition**

The element composition of a duplex steel has a great influence on its mechanical properties; minor adjustment may lead to a significant change of these materials. Here, the effects of the element composition on mechanical behaviour are listed:

Chromium (Cr) is added to steel to increase corrosion resistance, oxidation resistance, hardenability and/or high-temperature strength. To produce superior mechanical properties, chromium is frequently added as a toughening element.

Nickel (Ni) is an important element in duplex steels as it is a ferrite strengthener. It remains in solution in ferrite, strengthening and toughening the ferritic phase and thus improving the hardenability and impact strength of the steel. Higher Cr contents prevent the formation of martensite and favour the formation of ferrite, which can be prevented by a higher content of nickel. Since high nickel contents are associated with high costs, CrNi steels often have Cr contents in the range of 18% and Ni contents in the range of 8%.

Nitrogen (N) is the most effective solid solution strengthening element and is beneficial to corrosion resistance. The formation of intermetallic phases allows processing and fabrication of duplex steels. The effect of nitrogen on mechanical properties of austenitic steel 304 is illustrated in Fig. 2.2.1 where the yield strength increases by 50% at nitrogen contents of 0.20 wt.%.

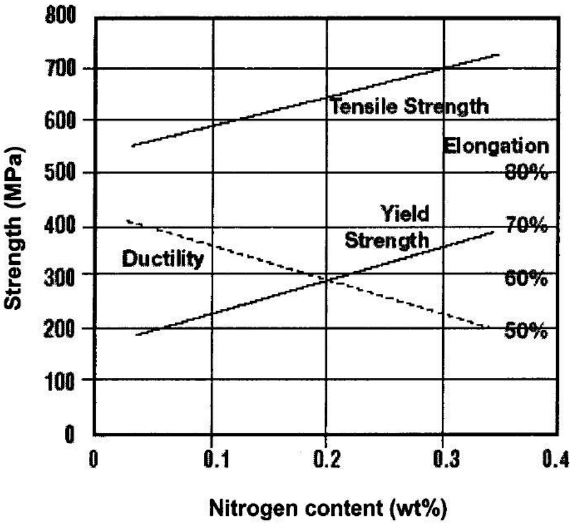

**Fig. 2.2.1:** Effect of nitrogen content on the yield strength, tensile strength and ductility of type 304 stainless steel [51].

Molybdenum (Mo) increases the hardenability and may cause the secondary hardening of quenched steels during tempering. It enhances the creep strength of low-alloy steels at elevated temperatures.

Manganese (Mn) is generally beneficial to corrosion resistance, but is deleterious to the ductility and weldability properties. In addition, manganese has a great effect on the hardenability of steels.

Carbon (C) is the major element on primary hardening in steels. It enforces the hardness and tensile strength but decreases the ductility and weldability of the materials.

Silicon (Si) is one of the principal deoxidizers and has less influence on improving strength and hardness of the material than manganese. It is detrimental to the surface quality.

In all, increasing the levels of micro-alloy elements increases strength but decreases ductility of steels. The effect of alloying element on strength of austenitic and austenitic-ferritic steels can follow Nordberg's regression [52] analysis:

$$R_{p0.2} = 120 + 210\sqrt{N + 0.02} + 2Mn + 2Cr + 14Mo + 10Cu$$

$$+(6.15 - 0.054\delta)\delta + \left(7 + 35(\mathrm{N} + 0.2)\right)d^{-1/2} \tag{2.6}$$

$$R_m = 470 + 600(N + 0.02) + 14Mo + 1.5\delta + 8d^{-1/2} \tag{2.7}$$

where $R_{p0.2}$ is the 0.2% proof strength in MPa, $R_m$ is the tensile strength, Mn, Cr, Cu, N and Mo denote the alloying element in wt.%, $\delta$ is the $\delta$-ferrite content and $d$ is the grain size in mm. In addition, duplex steels may contain small concentrations of one or more strong nitride and carbide element such niobium (Nb), titanium (Ti) and vanadium (V), combining with carbon and/or nitrogen to form finely dispersed precipitates.

### Influence of microstructure

DSSs exhibiting different mechanical or corrosion properties depend on the volume fraction of austenite and ferrite. In general, ferrite has higher yield strength but limited work hardening property. Austenite exhibits excellent corrosion resistance, ductility and strong work hardening behaviour. The work hardening exponent (n) is defined as:

$$\sigma = K \cdot \varepsilon^{n} \tag{2.8}$$

where $\sigma$ and $\varepsilon$ are the true stress and true strain, respectively, and n is the hardening exponent at 0.31–0.45 [53]. High values of n are for unstable steels, i.e., those which form martensite at large deformations. Elevated nitrogen contents decrease the value of n. The hardening component gives a good ductility for austenite which means that the material is extremely tough and exhibits a high failure elongation.

The volume fraction ratio of the two phases is determined by the chemical compositions of the material and the solidification conditions as well, as can be seen in Fig. 2.2.2. At a temperature below 1400 °C, austenite starts to nucleate and grows at the ferritic grain boundaries. The volume ratio of the two phases changes during cooling and stays stable near a temperature of 1000 °C.

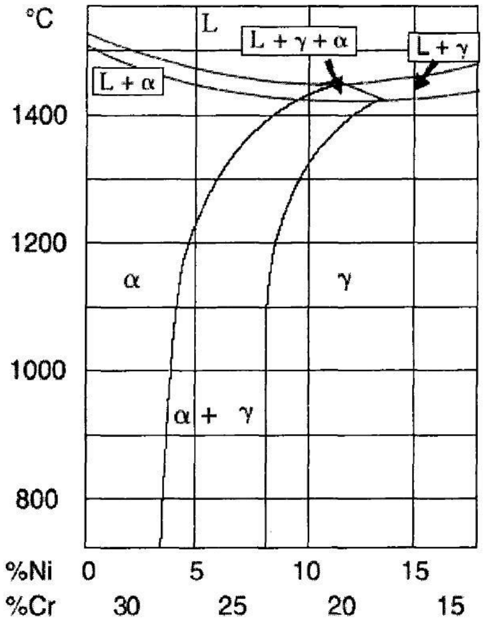

**Fig. 2.2.2:** Pseudo-binary Fe-Cr-Ni phase diagram at 68% iron [54].

Table 2.2.2 shows the mechanical properties of three grades of DSSs, in comparison to single austenitic and ferritic steels. Ferritic steels usually show higher strength but are less ductile, while austenitic steels give the opposite properties. Regarding DSSs, they have excellent ductility and strong work hardening characterised by high tensile strength.

**Table 2.2.2:** Mechanical properties of stainless steels at room temperature [55].

| Steel category | Grade | Tensile strength (MPa) | 0.2% yield strength (MPa) | Elongation (%) | Hardness (HRB) |
|---|---|---|---|---|---|
| Ferritic | 317L | 515 | 205 | 40 | 96 |
| | 317LN | 550 | 240 | 40 | 96 |
| | Sea-cure | 585 | 450 | 18 | 100 |
| | 2304 | 600 | 400 | 25 | 32 |
| | 2205 | 620 | 450 | 25 | 31 |
| | 2507 | 795 | 550 | 15 | 32 |

**Influence of texture and cold work**

When used in practical applications, DSSs are usually in the shape of sheet or rod bars produced by hot rolling or hot extrusion. The microstructures in such productions are characterised by a crystallographic texture, i.e., the materials have elongated grains with preferential orientations resulting in anisotropic properties. Normally, DSS products have a significantly higher strength in the transverse direction than in the rolling direction. Table 2.2.3 shows the anisotropic mechanical properties in the DSS 1.4462, obtained from Mateo et al. [49].

**Table 2.2.3:** Mechanical properties of the DSS 1.4462 as a function of specimen orientation (T, L and D represent for specimens produced in the transverse, longitudinal and 45° with the longitudinal direction).

| Sample | $\sigma_y$ (MPa) | $\sigma_{uts}$ (MPa) | Elongation (%) | Fatigue limit (MPa) |
|---|---|---|---|---|
| T | 651 | 840 | 32 | 450 |
| L | 598 | 773 | 40 | 425 |
| D | 580 | 768 | 46 | 350 |

The mechanical properties of stainless steels are also strongly affected by cold work. When the strain path is changed, the flow strength and work hardening rate will typically diverge from those expected from monotonic deformation. The change in plastic response can be classified into two types [56]: 1) decreased initial flow stress followed by a high work hardening rate, 2) increased initial flow stress followed by a low or possibly negative work hardening rate. The first type was characterised by internal stresses coming from the prestrain of an inhomogeneous microstructure. Regarding the second type of plastic response, the latent hardening caused by interaction between two active slip systems is the main reason.

Investigations on cold formed DSS revealed that load sharing changes between the two phases due to the internal stresses generated from cold work. Dislocation arrangements in the austenitic grains increase the yield and tensile strengths and accordingly decrease the failure elongation.

### 2.2.2 Fundamentals of residual stresses

Residual stresses are the stresses remaining in a material or body after manufacturing and processing in the absence of external forces or thermal gradients [57]. Basically, residual stresses are from the mismatch between different regions due to the plastic deformation or temperature or combination of plastic deformation and temperature. The component then undergoes inhomogeneous elastic or plastic deformation in such a manner that incompatibilities of the state of deformation occur. In practice, the origin of residual stress can result from various reasons, as summarised below:

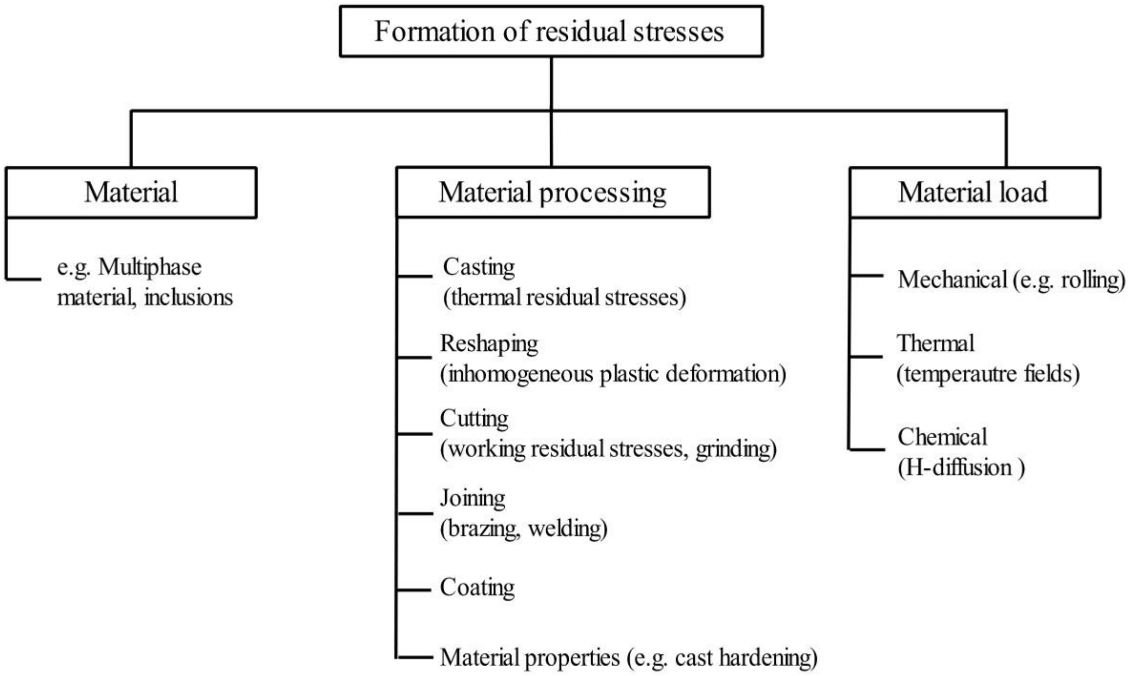

**Fig. 2.2.3:** Origins of residual stresses [58].

As a matter of fact, residual stresses have both detrimental and favourable consequences for materials under certain conditions. Compressive residual stresses on the surface can significantly improve the mechanical properties and thus lead to high resistance to failure, while tensile residual stresses play the opposite role. As addressed by Christ et al. [15], residual stresses cannot be neglected in fatigue testing. In VHCF, residual stresses are sometimes comparable with the applied stress. As there are different types of residual stresses, it is critical to consider how and/or which kind of residual stress affects the mechanical property of materials. In literature, residual stresses can be referred to macro, micro, internal, type I (II or III), phase, transgranular or intergranular residual stresses, according to different authors. The most accepted classifications of the residual stresses are the macro, micro residual stresses or the type I, II and III residual stresses. Normally, macro residual stress corresponds to type I residual stress, while micro residual stresses are the sum of type II and type III residual stresses. However, conceptual confusion usually originates from distinct materials, i.e., single or multiphase materials. For two- or multiphase materials, type II residual stress is normally caused by heat treatment due to the different thermal expansion coefficients among the phases. For single phase materials, type II residual stress is the difference value between a local region and the whole specimen. One situation is the shot peening method, where considerable residual stress is built up due to plastic deformation on the surface compared with the inner material. The different value between the two parts is the type II residual stress. In order to better understand the concept of residual stresses and their physical meanings, these explanations are summarised as below:

- Type I (macro) residual stress represents the average residual stress acting within all phases and crystals homogeneously in the gauge volume. It balances itself from one large region to another, i.e., from the surface to the inner part of the material. Releasing of type I residual stress causes macroscopic shape change of the material.
- Type II (micro) residual stress describes the mean deviation from the macroscopic residual stress level of an individual grain for single phase material. In a multiphase material, type II residual stress represents the average residual stress of the crystals belonging to a phase $\alpha$ contributing to the measurement. Releasing of type II residual stress leads to microscopic distortion.
- Type III (micro) residual stress is the local deviation of the residual stresses within a single grain from its average residual stress. It originates from local defects and is not homogeneously distributed across submicroscopic areas (atomic scale). Releasing of such residual stress thus cannot cause microscopic distortion.

The existence of the three types of residual stresses in a single- and duplex-phase material is schematically illustrated in Fig. 2.2.4. Fig. 2.2.4(b) reveals three types of residual stress distributions in the DSS 1.4462 used in this study. Type I residual stress is caused by different cooling speeds between surface and inner parts of the material and type II residual stress arises from different thermal expansion coefficients between the two phases. In the following chapters, macro residual stress mentioned is related to type I residual stress, and micro residual stress is only related to type II residual stress. Type III residual stress is typically smaller than the other two residual stresses and is not in consideration in this thesis.

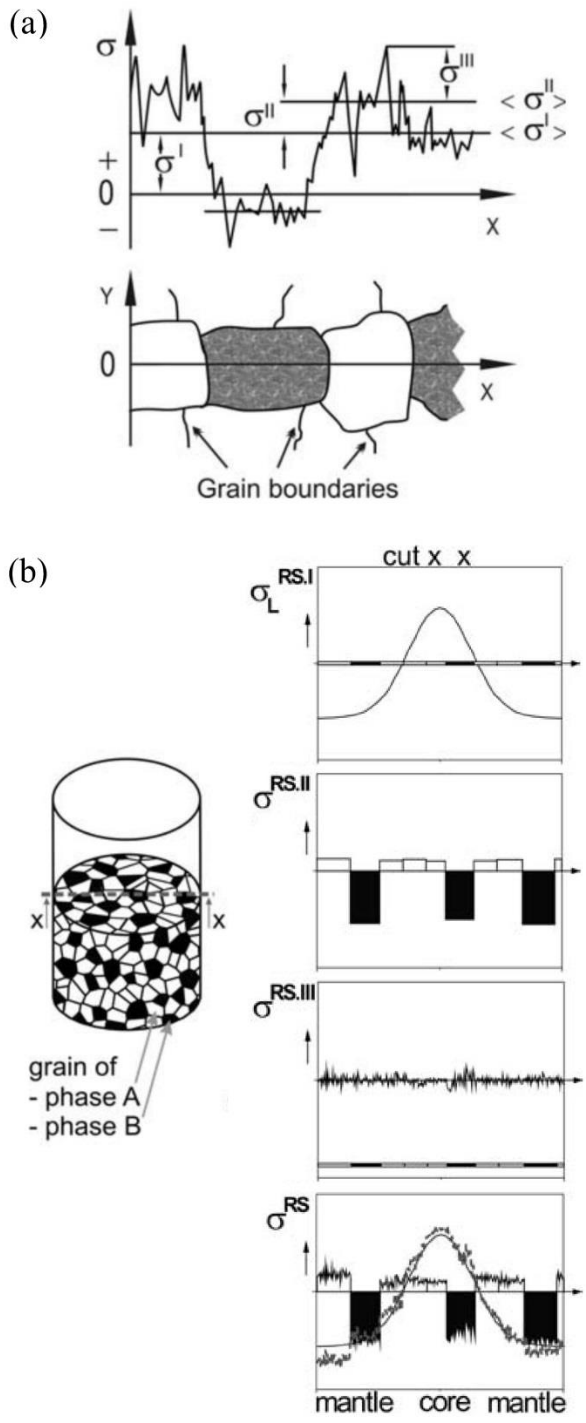

**Fig. 2.2.4:** Schematic showing the three different types of residual stresses distributed in a) single phase materials and b) two-phase materials [59].

As described, compressive residual stresses play a positive role for materials with respect to improving the mechanical properties. In practice, compressive residual stresses in engineering components are induced by shot peening on the surface to enhance fatigue resistance. The lifetime of materials, theoretically, can be predicted by taking residual stresses in consideration when the residual stress magnitude and distribution are well assessed. It is thus essential to know how residual stresses develop during cyclic fatigue loading. Normally, a relaxation of compressive residual stresses can be observed when the specimen is cyclically fatigued. Özdemir and Edwards [60] studied residual stress relaxation in 7075-T7 aluminium and concluded that the relaxation of residual stresses is due to the growth of short cracks in the most stressed zone. Iida and Taniguchi [61] investigated the residual stress relaxation on the shot-peened C45 steel after alternate bending, and found that residual stresses relax after $10^5$ cycles of testing. Torres and Voorwald [62] investigated the quenched and tempered AISI 4340 steel with various Almen shot peened intensities. The specimens were subjected to rotating bending fatigue test. Residual stresses were found to lost approximately 50% after $10^3$–$10^4$ cycles and then become stable; the higher the applied stress, the greater the relaxation of residual stresses. A similar result can be observed from investigation [63] of Juijerm et al. of a deep rolled aluminium, which revealed that compressive residual stresses do not relax if they achieve a critical value of -300 MPa, otherwise a relaxation of residual stresses could be obtained as shown in Fig. 2.2.5.

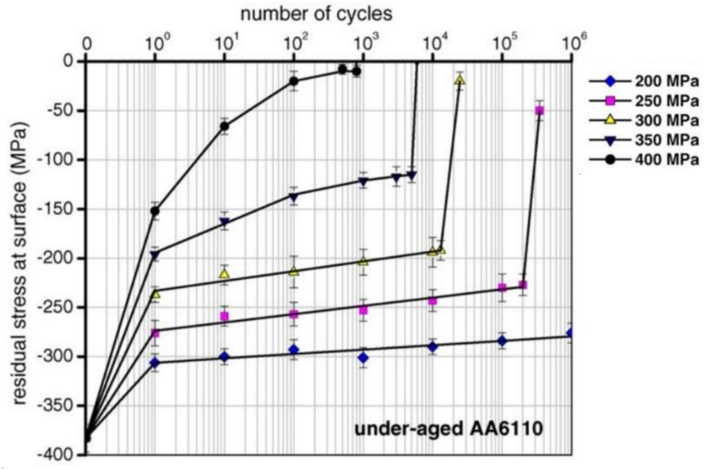

**Fig. 2.2.5:** Residual stresses relaxation at the surface of deep rolled under-aged AA6110 during stress-controlled fatigue at room temperature for different stress amplitudes [63].

Zaroog et al. [64] demonstrated that the relaxation of residual stresses induced by shot peening could be divided into two stages: the first cycle relaxation due to surface yielding and the following cycles having a gradual relaxation. The cyclic relaxation is affected mainly by the initial magnitude and gradient of the residual stress field and degree of cold working, fatigue stress amplitude, the number of cycles, mean stress, material cyclic stress-strain response and the degree of cyclic hardening/softening.

Prior research on residual stress development in two-phase materials focused on the internal stress changes, as surface modification such as shot peening, laser peening or coating was rarely employed. Internal stresses caused by thermal processes or plastic deformation are unevenly distributed and develop to give a compromise between the inhomogeneous microstructure and the anisotropic deformation during cyclic loading. They do not vanish until a total fracture at the interface releases them, during which they inevitably take part in crack initiation.

An informative study about residual stress development of the DSS X2CrNiMoN22-5 can be found in Possel-Dölken's dissertation [65]. The specimens prepared in the normal annealed state and rolled state were fatigued in cyclic bending tests at different stress amplitudes. One representative stress profile can be seen in Fig. 2.2.6.

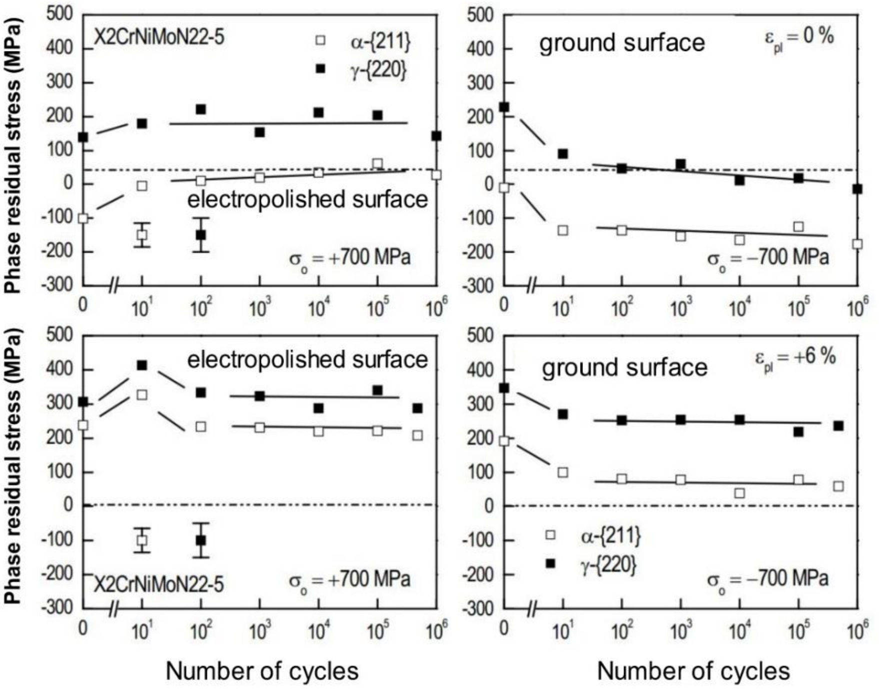

**Fig. 2.2.6:** Phase residual stress (type I + type II) development of the normal (upper figures) and the rolled state (bottom figures) specimens with electropolished and ground surface at a surface stress amplitude of $\sigma_0$=±700 MPa[65].

After numerous experiments, it was concluded for micro residual stresses that:

- The micro residual stresses for all tested samples are stable,
- The orientation dependent residual stresses are more sensitive to plastic deformation,
- The micro residual stresses can be considered into the lifetime calculation because they are stable and do not relax during cyclic fatigue loading.

Residual stress development of the same material was also investigated by Hauk [66] under cyclic loading at different stress amplitudes, as shown in Fig. 2.2.7. Macro residual stresses increase and then become stable. Micro residual stresses develop only at the very early stage and then stay almost unchanged. The occurrence of micro residual stresses can be associated with the change of microstructures and the strength of the material.

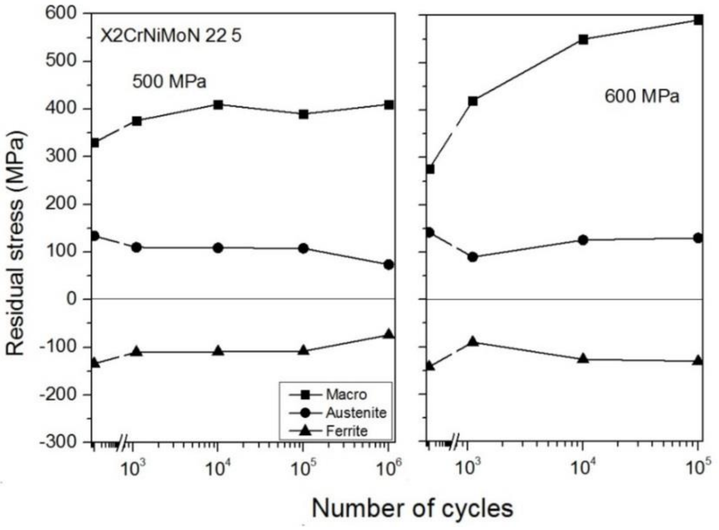

**Fig. 2.2.7:** Development of residual stresses in the DSS X2CrNIMoN 22 5 at stress amplitude of 500 MPa and 600 MPa [66].

Johansson [67] investigated residual stress evolution of commercial DSS of type SAF 2304 by means of XRD. The total stress tensors were measured and separated into macro and micro stress tensors, as can be seen in Fig. 2.2.8. The stresses in the rolling direction increase during the first hundred cycles and then reach a saturation stage. The stresses in the other two directions show similar trends, but the changes are smaller and fall within the error range. The rapid hardening of the austenitic phase can be attributed to the increase in micro residual stresses. The cyclic loading response of the duplex steel is thus mainly controlled by the plastic deformation behaviour of the austenitic phase.

The stability of micro residual stresses in different fatigue conditions for different materials is distinct, depending on the initial state, elastic and plastic response of materials. An accurate analysis of residual stress development is thus required because the integral structural life can be only precisely estimated when the role of residual stresses and microstructure-induced stress heterogeneity is considered.

Micro residual stresses are actually the result of back stresses due to dislocation pile-ups at grain or phase boundaries and elastically strained second phase of heterogeneous materials [68]. If these dislocations move in the reverse direction during localised plastic deformation, the back stresses and hence the directed micro residual stresses are initially reduced. Further deformation causes renewed build-up of back stresses in the opposing direction accompanied by dislocation multiplication and hardening, which will once again increase the micro residual stresses.

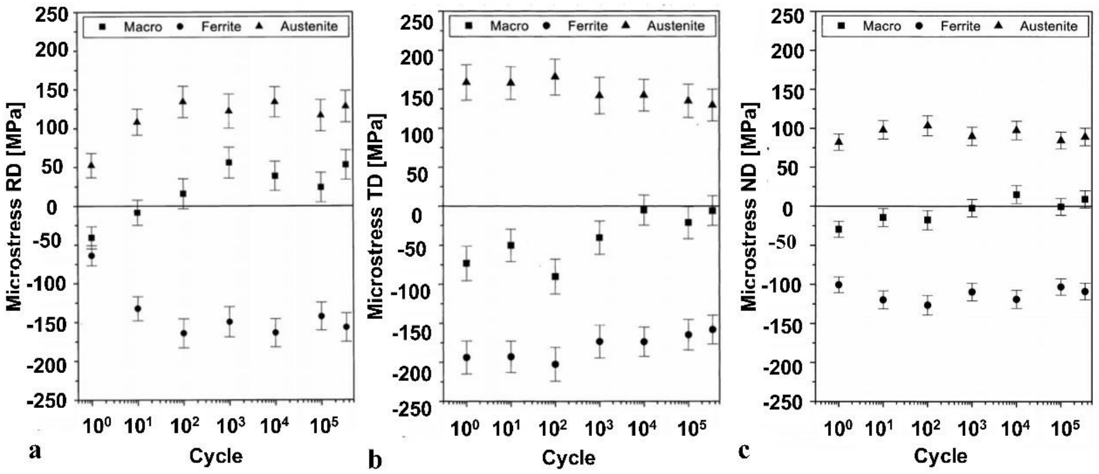

**Fig. 2.2.8:** Evolution of micro residual stresses of SAF 2304 DSS during fatigue load cycles a) stresses in the rolling direction, b) stresses in the transverse direction and c) stresses in the normal direction [67].

Dislocation arrangement during cyclic deformation leads to low energy state of dislocations, giving rise to micro residual stress relaxation. Newly generated dislocations give a renewed build-up micro residual stresses in a superposition of the relaxation process. In this thesis, the evolution of residual stresses is systematically investigated in HCF and VHCF regimes. Dislocation micrographs were observed by means of TEM to interpret the variations. The results are shown in section 1 of chapter 4.

Almer et al. [69] investigated the residual stress evolution of 1080 DSS during fatigue loading at a stress load ratio R=0, and found that macro residual stress relaxes at the very early stage and then stays almost stable until the material fractures. It is thus reasonable to incorporate macro residual stress into the calculation of fatigue life by using strain life equation:

$$\Delta\varepsilon = \Delta\varepsilon_{el} + \Delta\varepsilon_{pl} = \frac{\sigma_f' - \sigma_m}{E}(N_f)^b + \varepsilon_f'(N_f)^c \qquad (2.9)$$

where $\sigma_f'$ and $\varepsilon_f'$ are fatigue strength and fatigue ductility coefficient, and $b$ and $c$ are the fatigue strength and fatigue ductility exponents, respectively. Finite element simulation results showed that in the high cycle fatigue regime the strain range is dominated by the elastic strain contribution. Under this condition, equation (2.9) can be modified to:

$$N_f = \left(\frac{\Delta\sigma}{\sigma_f' - (\sigma_a + \sigma_{res}^M)}\right)^{1/b} \qquad (2.10)$$

Using the definitions of stress amplitude $\sigma_a = E\varepsilon_{a,elastic}$ and mean stress $\sigma_m = \sigma_a + \sigma_{res}^M$ (R=0 in investigation of Almer et al.), the number of cycles to failure can be predicted. Moreover, a better fit could be achieved by using this equation where the subscript $f$ (failure) was replaced to $i$ (initiation). The fit lines can be seen in Fig. 2.2.9.

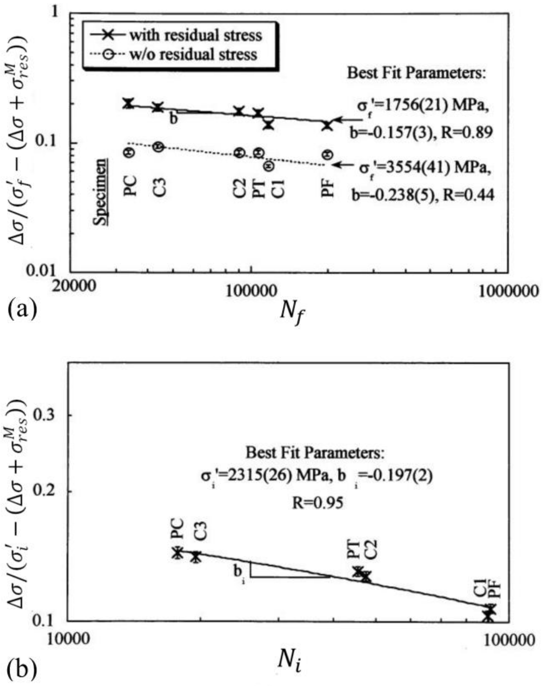

**Fig. 2.2.9:** Relationship between notch stress and a) $N_f$ and b) $N_i$, showing good correlation when macro residual stress is considered [69].

Macro residual stress was also considered into crack propagation, in which the crack growth rate $dN/da$ against stress intensity factor range $\Delta K$ is plotted. A representative curve for crack propagation is shown in Fig. 2.2.10 [70].

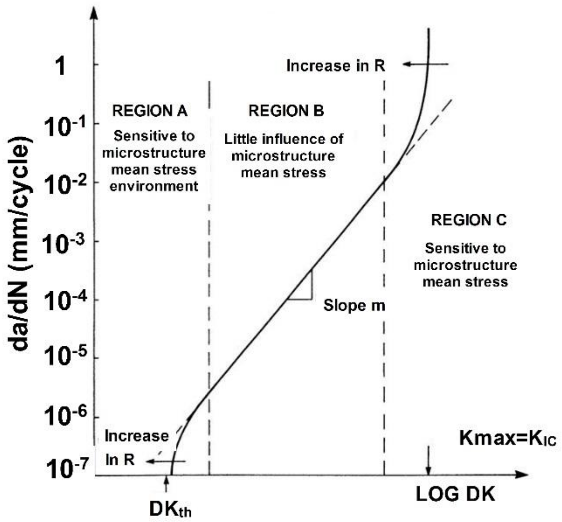

**Fig. 2.2.10:** Representative curve for fatigue crack growth rate [70].

This curve is composed of three regions, A, B and C. Regions A and C are microstructure sensitive while region B is sensitive to the load ratio R ($K_{min}/K_{max}$). According to Paris' law, the relationship between $dN/da$ and $\Delta K$ is:

$$\frac{dN}{da} = C\Delta K^{m} \tag{2.11}$$

where $C$ and $m$ are material parameters. An increase in R causes regions A and C to move to lower $\Delta K$ values. When macro residual stress is present, $\Delta K$ can be changed to:

$$R_{eff} = \frac{K_{min}+K_{res}}{K_{max}+K_{res}} \tag{2.12}$$

where $K_{res}$ is the stress intensity factor due to the macro residual stress. Tensile residual stress field leads to larger $R_{eff}$ than R, leading to lower $\Delta K$ values. The effective stress intensity factor range $\Delta K_{eff}$ is actually responsible for the crack process as:

$$\frac{dN}{da} = C\Delta K_{eff}^{m} \tag{2.13}$$

For a material in which fatigue crack propagation rate is sensitive to R in region B, compressive residual stress would have the most influence on fatigue crack growth when $K_{min} < |K_{res}|$ [70]. The micro residual stresses, however, according to Almer et al. [71] have no influence on crack propagation since they fade rapidly within the crack tip during fatigue.

### 2.2.3 Load sharing in two-phase alloys

Two-phase materials like martensitic-ferritic alloys and austenitic-ferritic alloys or composites consist of a harder phase and a relative soft phase. When the applied cyclic stress is higher than the yield point of the softer phase (damage zone in Fig. 2.2.11), material damage can take place in the softer phase during cyclic loading [72]. As a consequence, the following phenomena were observed:

- Formation of cracks in the soft phase by intrusion and extrusion processes.
- Formation of cracks at the grain boundaries by dislocation pile-ups.

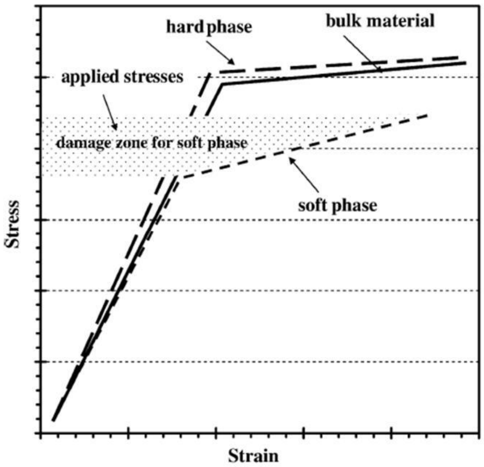

**Fig. 2.2.11:** Stress versus strain curves of two-phase materials, where the hard phase is much stronger than the soft phase [72].

The evidence indicates that material damage initiates at the softer phase, leading to two types of crack initiation due to the deformation mismatch between the two phases. One of these is where crack initiation starts in the damaged soft phase, and the other starts either at the phase or grain boundaries or in the corner of the grains [72].

The stress distribution in two-phase materials can be achieved either by computer simulation or experimentally by in-situ XRD work. Calculation of stresses and strains in multiphase materials goes back to the 1960s, during which the most successful model for determination of micro stresses was developed by Eshelby [73], combining the Voigt (homogeneous strain) and Reuss model (homogeneous stress). This model, based on an ellipsoidal, anisotropic inclusion surrounded by an infinite extended matrix, was applied to calculate the load stress and residual stress, taking different elastic moduli, thermal expansion coefficients and yield stresses into consideration. The inclusion can undergo a transformation (such as twinning or localised thermal expansion) but the change of shape and size is restricted because of the surrounding matrix. Under this condition, the inclusion and the surrounding material remain in a stressed state. The strain states in the body and the inclusions are potentially inhomogeneous. Eshelby introduced the idea of an imaging stress in order to satisfy the boundary conditions for a dilute composite, i.e., the inclusions are randomly distributed within the matrix. According to equation 2.14, the mean stress can be calculated easily.

$$(1-f) < \sigma_M > +f < \sigma_I >= 0 \tag{2.14}$$

$f$ is the fraction inclusion I in a matrix M. The model has the following attributes:

- It has a rigorous analytical basis for low inclusion concentrates.
- It is valid for all aspect ratios.
- It can be computed on a programmable calculator or computer.
- It applies to thermal and to load-induced stress fields.
- It is rigorous only for ellipsoidal particles.
- It is conceptually difficult to grasp and
- additional assumptions are required to model plastic flow.

According to this model, simulation works [74-76] have been conducted successfully to analyse stress distribution in multiphase materials and composites. Experimentally, diffraction methods as described are often utilized in evaluating the stress distribution between phases of a material [77]. With the development of high energy X-rays, synchrotron and neutron radiation techniques are becoming more and more powerful tools for analysing the residual stress or load stress in two-phase materials due to the merits of nondestructivity, fast recording speed and strong penetration depth. The high penetration depth involves large volume fraction of grains of the material, contributing to the diffraction mode in all directions. An arbitrary strain can be thus calculated from the 2D detector. In particular, when strains in the loading and transversal directions are analysed (in the inner part of the material, the strain in the normal direction is typically considered as the same as in the transversal direction, namely, $\varepsilon_{yy} = \varepsilon_{zz}$), the stresses in the two phases can be achieved according to the following principle:

$$(1-f) < \sigma_M > + f < \sigma_I > = \sigma_{app} \tag{2.15}$$

Bacon et al. [78] investigated phase stress during loading of a steel-based matrix composite by means of high energy synchrotron radiation. A load transfer from the matrix to the reinforcement $TiB_2$ occurs, as shown in Fig. 2.2.12. The results also indicate that there is good interfacial cohesion between the matrix and the reinforcement during loading.

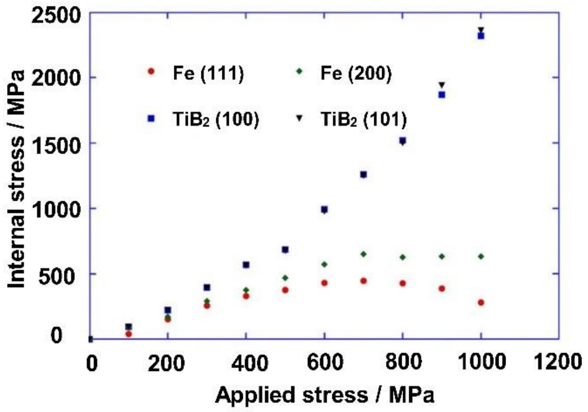

**Fig. 2.2.12:** Load transfer in the Fe and $TiB_2$ phases of the 316/$TiB_2$ composite [78].

Load transfer effects during fatigue were investigated by Johansson et al. [67], who determined the stress-strain curves in different fatigue load cycles for an austenitic-ferritic DSS. A load-sharing index $L_\mathrm{i}$ (equation 2.16) was introduced to better interpret the load transfer phenomenon:

$$L_\mathrm{i} = V_f^\alpha \frac{<\sigma^\alpha_{RD,t}>_i^{MAX} - <\sigma^\alpha_{RD,t}>_i^{MIN}}{<\sigma_{RD,M}>_i^{MAX} - <\sigma_{RD,M}>_i^{MIN}} \tag{2.16}$$

where $V_f^\alpha$ is the volume fraction of the ferritic phase, $< \sigma^\alpha_{RD,t} >_i^{MAX}$ and $< \sigma^\alpha_{RD,t} >_i^{MIN}$ denote the maximum and minimum average total stress in the ferritic phase for cycle $i$, while $< \sigma_{RD,M} >_i^{MAX}$ and $< \sigma_{RD,M} >_i^{MIN}$ denote the maximum and minimum macrostress for cycle $i$. This index has the following properties: when $L_\mathrm{i}$=0, all load is taken by the austenite, when $L_\mathrm{i}$=1, all load is taken by the ferrite and when $L_\mathrm{i}$=0.5, both phases take the same amount of load. Notice that when $L_\mathrm{i}$ is equal to $V_f^\alpha$, both phases transfer the same amount of load per unit area and thus both phases have the same elastoplastic behaviour. From the equation, it is important to note that micro residual stresses strongly affect the load-sharing index. The load-sharing index variation with number of cycles can be seen in Fig. 2.2.13. Initially, the austenitic phase behaves similarly to the ferritic phase. But for the following cycles, more loads per unit area are transferred to ferrite. A maximum load-sharing index was observed at the fatigue load cycle number of N=400 followed by a decrease in load-sharing index, indicating a hardening process of austenitic phase takes place.

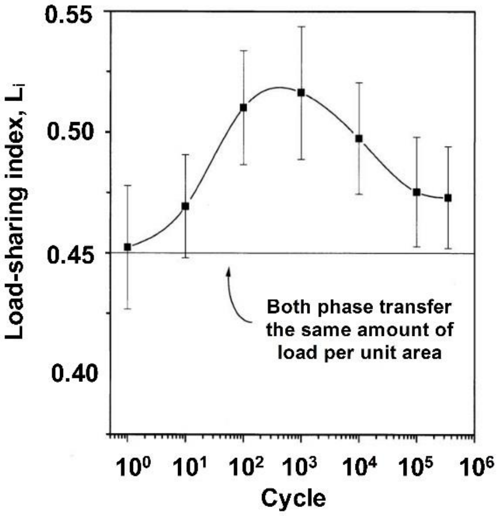

**Fig. 2.2.13:** Load-sharing index as a function of load cycle [67].

In VHCF, fatigue damage locally occurs in several grains or even only one grain, and cracks initiate at such sites by intensification of the incompatibility with increasing load cycles. Techniques with higher resolution are thus required to identify the damage accumulation and its driving force evolution. Digital image correlation has recently been combined with SEM to track full-field deformation on the nano-scale, and the results can link the microstructural features of a material to its macro-scale mechanical behaviour.

The DIC method is a non-contact optical technique used to measure the displacement on the surface of an object. The basic principle is to create randomly distributed fine particles or patterns on the surface and then calculate the displacements of such patterns after deformation or other conditions by comparing with the initial state. Numerous efforts have been achieved by employing DIC to two-phase materials in order to better understand the deformation behaviour of each phase and the interactions in between. Alharbi et al. [79] investigated a ferritic-martensitic steel by using DIC, from which the strain distribution was acquired. The results indicated that ferrite and martensite have deformed to similar degrees, with a slightly higher mean value for the softer ferrite. Cracks initiate at the sites where the strain are present. Ososkov et al. [80] studied the strain partitioning in DP600 steel by using DIC and found that the local strain distribution is not inhomogeneous where 70% of the maximum of the mean strain is located in ferrite and 30% of the maximum of the mean strain is taken by martensite. Ghadbeigi et al. [81] utilised in-situ tensile tests during SEM measurement and used DIC to measure the strain distribution in DP1000 steel during deformation. Plastic strains in two phases were statistically analysed, as can be seen in Fig. 2.2.14. The martensite experiences large plastic deformation during tensile testing with local strain values up to 110% for an applied strain of 42%. The strain partitioning is very comparable between the two phases throughout the test.

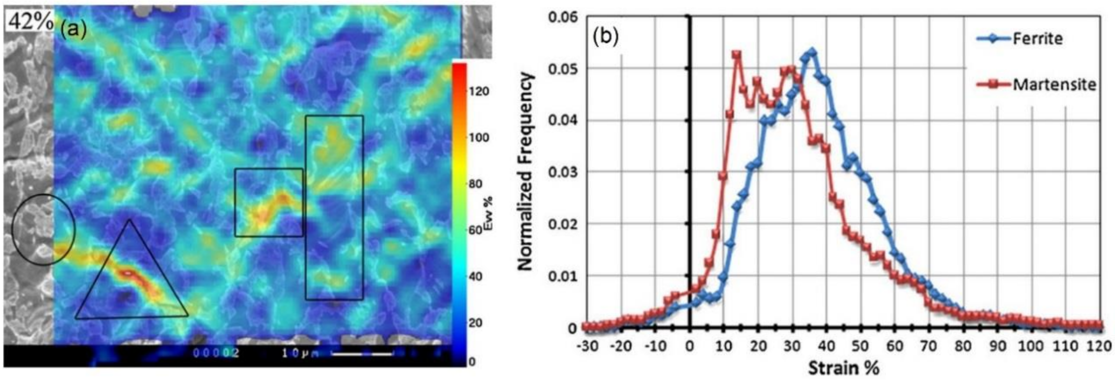

**Fig. 2.2.14:** Plastic strain distribution of DP1000 during tensile testing in a) the microstructure and b) quantitatively plotted for each phase [81].

Based on the review above, diffraction and DIC methods are powerful tools to analyse stress and strain partitioning. In this thesis, both methods were applied to the DSS 1.4462 in the VHCF regime, attempting to reveal the intrinsic nature of the elastic-plastic responses of the material and explore the mechanisms of crack initiation. These parts will be presented in sections 3 and 4 of chapter 4.

# 3 Experimental techniques

This chapter describes the experimental details in the present investigation. The material used and all fatigue testing apparatuses are described in section 1. Material characterisation techniques are described in section 2. The stress and strain partitioning determined by means of XRD and DIC are presented in sections 3 and 4.

## 3.1 Materials, specimen preparation and test apparatuses

### 3.1.1 Materials and specimens used

The material used in this investigation is an austenitic-ferritic DSS 1.4462 (X2CrNiMoN22-5-3 or 318LN). The chemical composition is given in Table 3.1.1.

**Table 3.1.1:** Chemical composition of the DSS 1.4462 used in this study [82].

| Fe | C | Cr | Ni | Mo | Mn | N | P | S |
|---|---|---|---|---|---|---|---|---|
| Bal. | 0.02 | 21.9 | 5.6 | 3.1 | 1.8 | 0.19 | 0.023 | 0.002 |

Delivered rod bars with a diameter of 25 mm were cut into small pieces and sent into furnace for heat treatment. The material was heated up to 1250 °C and annealed for 4 h, then cooled down to 1050 °C within 3 h for nucleation and growth by about 50% in the austenite grains. Finally, the material was quenched in water to avoid the formation of σ phase and spinodal decomposition of the ferrite. The resulting microstructure (Fig. 3.1.1) consists of 50% austenite with an average grain size of 46 μm and a Vickers hardness of 260 HV, and 50% ferrite with an average grain size of 33 μm and a Vickers hardness of 280 HV.

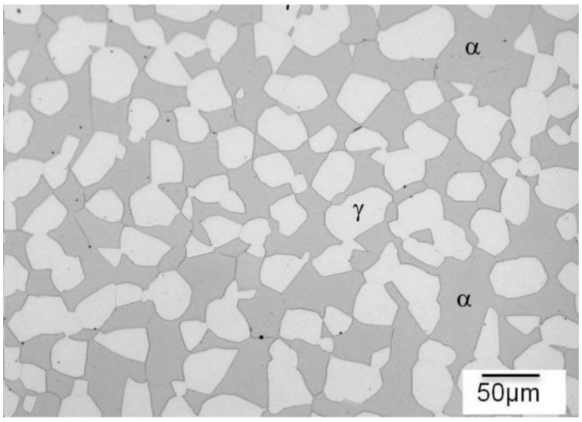

**Fig. 3.1.1:** Microstructural features of the heat treated DSS 1.4462 [83].

Mechanical properties of the material were investigated by Düber et al. [84] who analysed the critical cyclic shear stress for the austenite phase being 68.5 MPa and for the ferrite phase being

99 MPa. Further mechanical properties are listed in Table 3.1.2 for heat treated condition (HTC) and initial condition (IC).

**Table 3.1.2:** Mechanical properties of HTC and IC samples [22].

| | E [GPa] | $R_{p0.2}$ [MPa] | $R_{p0.01}$ [MPa] | $R_m$ [MPa] |
|---|---|---|---|---|
| HTC | 197 | 535 | 380 | 770 |
| IC | 197 | 720 | 615 | 870 |

Subsequently, the heat treated rod bars were machined to hourglass or dog-bone shaped specimens for VHCF investigations. The geometries are shown in Fig. 3.1.2 (a) and (b). For residual stress measurement in HCF, the geometry of the specimens used is shown in Fig. 3.1.3.

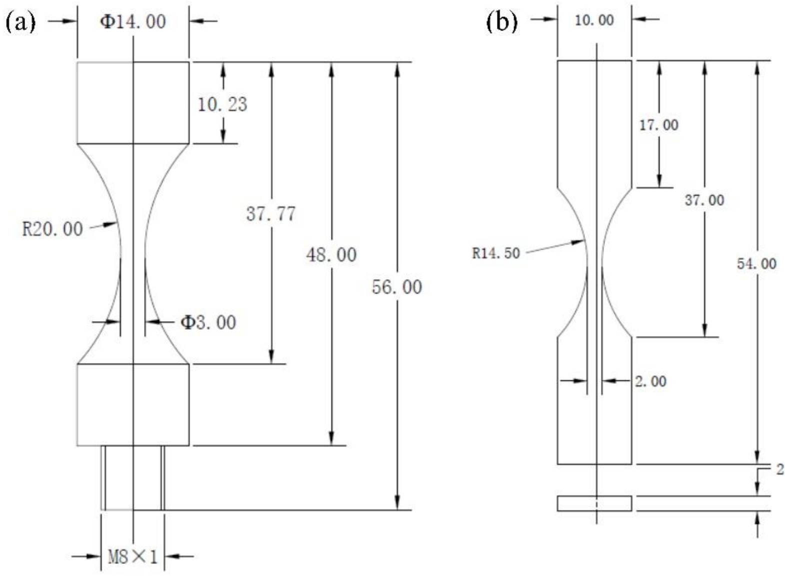

**Fig. 3.1.2:** Geometries of the VHCF specimens a) hourglass shaped and b) dog-bone shaped.

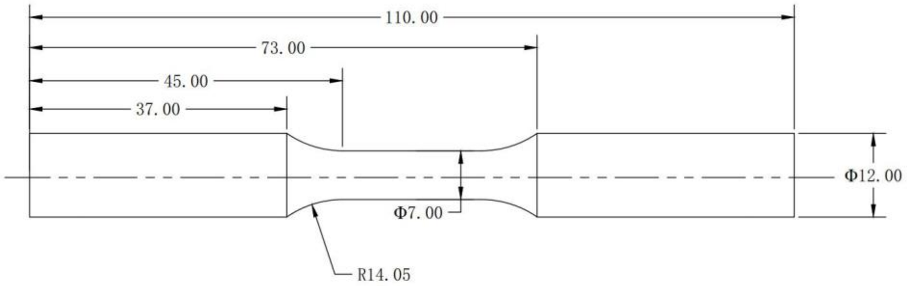

**Fig. 3.1.3:** Specimen geometry used in HCF for residual stress determination.

Finally, the specimens were ground using SiC sandpaper up to 2500 grit and then electropolished for 15 min in an electrolyte containing 70 vol.% ethanol, 12 vol.% distilled water, 10 vol.% diethylene and 8 vol.% perchloric acid (70%) at T=−35 °C and U=12 V.

### 3.1.2 Ultrasonic fatigue machine

Cyclic loading in VHCF was executed in an ultrasonic testing system (BOKU Vienna) at a frequency of f=20 kHz under fully-reversed mode (stress ratio R=−1). The loading part of the machine is controlled by the ultrasonic fatigue test generator, serving power to an ultrasonic converter which transfers a sinusoidal electric power into mechanical oscillations and injects longitudinal waves into one end of the load train. The stress wave is then magnified in amplitude by means of a narrowing horn and transferred into the sample. The stress amplitude is maximum at the most narrow cross section (i.e., in the middle) of the sample, as seen in Fig. 3.1.4. The elastic strain amplitude is measured by means of a strain gauge during calibration and the strain gauge is used to calculate the stress amplitude via Hooke's law. A control system keeps the stress amplitude constant during testing via online control of the signal of an inductive displacement gauge. The damping of the investigated DSS causes a significant heat generation, which was counteracted by using a pulse-pause loading mode. This reduces the effective testing frequency to about 1.5–2 kHz. Moreover, cooling air was impacted to the specimens to keep the testing at room temperature.

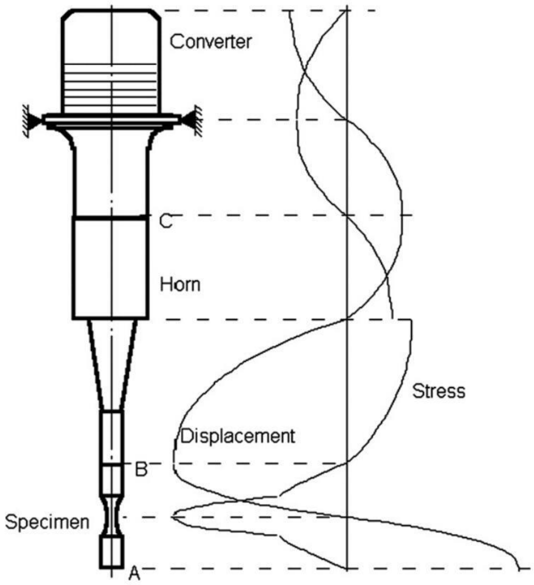

**Fig. 3.1.4:** Load train to perform ultrasonic fatigue test in tension-compression mode [85].

### 3.1.3 Resonance and servo-hydraulic fatigue machine

Fatigue tests in HCF and LCF were carried out by using a resonance fatigue machine (Rumul) or servo-hydraulic fatigue machine. The former is controlled by a spring-mass-system which excites a sinusoidal vibration for the whole specimen. When the mass of the clamping systems $m_0$ (upper part), $m_1$ (bottom part), the length L, the cross section area A and the Young's modulus E of the specimen are known, the frequency $f_0$ can be calculated as:

$$f_0 = \frac{1}{2\pi}\sqrt{\frac{EA}{L}\frac{m_0+m_1}{m_0 \cdot m_1}} \tag{3.1}$$

The resonance fatigue machine provides a frequency of 80–100 Hz. During testing, cooling air was used in order to keep the specimen at room temperature.

Fatigue tests executed in LCF were examined by a servo-hydraulic fatigue machine MTS 810 in laboratory air at room temperature. Tests were performed under fully reversed stress control with a continuous sinusoidal waveform at a constant frequency of 1 Hz. The stress-strain curve and the evolution of residual stress are shown and discussed in section 4.1.

### 3.1.4 Nanoindentation

Micro-hardness of one specimen was investigated in order to identify the hardness change of austenitic and ferritic phases during VHCF. Three austenitic grains with slip markings were randomly selected. Near the three austenitic grains, three adjacent ferritic grains were measured as well. For each measurement of the micro-hardness, seven measurements were performed continuously from the surface to the inner part of the grain to achieve the best accuracy.

## 3.2 Optical and electron microscopy

### 3.2.1 Confocal laser microscopy

Confocal laser microscopy (Olympus-4000) was used to examine the surface quality of the specimens after polishing and investigate the slip markings on the surface of the specimen after fatigue testing. Confocal laser microscopy was also employed to examine the pattern used in DIC experiments.

### 3.2.2 Scanning electron microscopy

A Philips XL30 SEM and a dual beam focused ion beam (FIB)/SEM system of type FEI Helios Nanolab 600 were used for crack identification on the surface. Small cracks under the surface and phase boundary orientations were observed after FIB-cutting. Phase identification in the micro zone was obtained by electron back-scatter diffraction (EBSD) equipped in the Helios Nanolab 600.

### 3.2.3 Transmission electron microscopy

TEM examinations were carried out applying a Talos$^{\mathrm{TM}}$ F200A TEM. Dislocation arrangements in austenitic and ferritic phase of the specimens were observed before and after fatigue. The specimens with a diameter of 3 mm and thickness of 80-120 μm were cut and ground from the bulk material. They were polished in a jet apparatus (Tenupol-3) containing an electrolyte consisting of 10 vol.% perchloric acid (60%) and 90 vol.% acetic acid at T=5–10 °C and U=40 V.

## 3.3 Synchrotron and laboratory X-ray diffraction

In this study, nondestructive techniques to measure the residual stresses were applied using high energy synchrotron radiation diffraction and laboratory XRD. The basic principle of the two methods is the same and is based on Bragg's equation. The path difference between the scattered beams in different planes, for instance, ray 1and 2 diffracted by planes A and B in Fig. 3.3.1, is:

$$ML + LN = dsin\theta + dsin\theta = 2dsin\theta \tag{3.2}$$

The prerequisite for the diffracted two beams being in phase is that the path difference equals an integer multiple of the wavelength:

$$2dsin\theta = n\lambda \tag{3.3}$$

Here $d$ is the lattice spacing, $\lambda$ is the wavelength of the X-ray and $\theta$ is the incident angle.

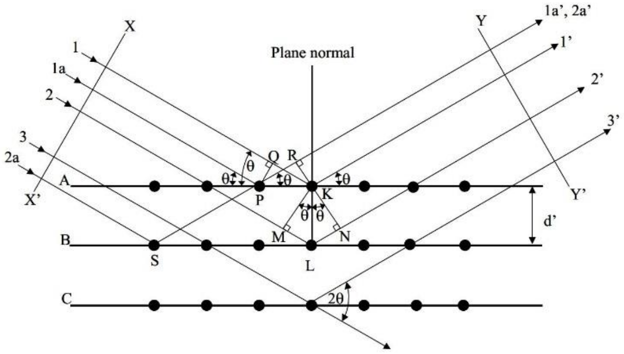

**Fig. 3.3.1:** Diffraction of the X-ray by a crystal lattice.

The presence of tensile or compressive stress leads to an expansion or compression of the inter-planar lattice spacing in the direction of the acting stress. Then the strain can be calculated according to the following equation:

$$\varepsilon = \frac{d-d_0}{d_0} \tag{3.4}$$

with $d_0$ being the lattice spacing of the stress-free material. From Bragg's equation, it can be obtained as:

$$\Delta\theta = -\varepsilon tan\theta \tag{3.5}$$

Analysis of peak shifts allows for the determination of strain values. In practice, however, stress or strain distribution is three dimensional. In order to obtain the stress tensors, a minimum of Cartesian systems must be defined:

- Sample system S: $S_1$ and $S_2$ are given by the sample itself and they are perpendicular to each other. $S_3$ axis is the normal direction to the sample surface which $S_1$ and $S_2$ lie in.
- Laboratory system L: $L_3$ is the measuring direction and perpendicular to the reflecting planes (*hkl*). $L_2$ is parallel to the sample surface and $L_1$ is normal to the plane of $L_2$ and $L_3$.

The azimuth angle $\psi$ and the pole angle $\varphi$ in the two systems are shown in Fig. 3.3.2.

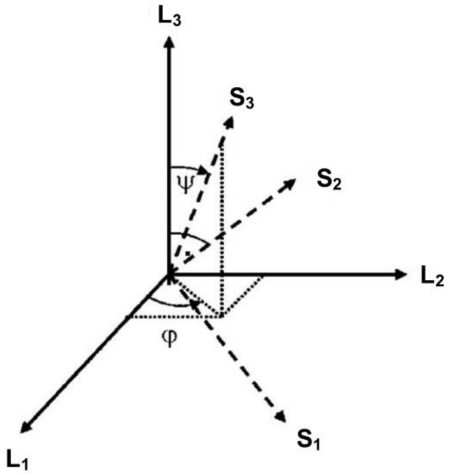

**Fig. 3.3.2:** Orientation of the laboratory system relative to the sample system.

The transformation matrix $\omega_{ij}$ between the sample system and laboratory system is given as:

$$\omega_{ij} = \begin{pmatrix} \cos\varphi\cos\psi & \sin\varphi\cos\psi & -\sin\psi \\ -\sin\varphi & \cos\varphi & 0 \\ \cos\varphi\sin\psi & \sin\varphi\sin\psi & \cos\psi \end{pmatrix} \tag{3.6}$$

Based on this, the strain in an arbitrary direction of defined plane (*hkl*) can be written as:

$$\varepsilon_{\varphi,\psi}^{hkl} = \varepsilon_{11}cos^2\varphi sin^2\psi + \varepsilon_{22}sin^2\varphi sin^2\psi + \varepsilon_{33}cos^2\psi$$

$$+\varepsilon_{12}sin2\varphi sin^2\psi + \varepsilon_{13}cos\varphi sin2\psi + \varepsilon_{23}sin\varphi sin2\psi \tag{3.7}$$

Given the specific elastic constants $E^{hkl}$ and $\nu^{hkl}$, the diffraction elastic constants (DEC), depending on the reflection (*hkl*) measured (which takes into account the anisotropy of the crystalline elasticity) are:

$$S_1^{hkl} = \frac{-\nu^{hkl}}{E^{hkl}} \tag{3.8}$$

$$\frac{1}{2}S_2^{hkl} = \frac{1+\nu^{hkl}}{E^{hkl}} \tag{3.9}$$

Equation 3.7 can be written by using stress components through Hooke's law:

$$\varepsilon_{\varphi,\psi}^{hkl} = \frac{1}{2}S_2^{hkl}sin^2\psi(\sigma_{11}cos^2\varphi + \sigma_{12}sin2\varphi + \sigma_{22}sin^2\varphi)$$

$$+\frac{1}{2}S_2^{hkl}(\sigma_{13}cos\varphi sin2\psi + \sigma_{23}sin\varphi sin2\psi + \sigma_{33}cos^2\psi)$$

$$+S_1^{hkl}(\sigma_{11} + \sigma_{22} + \sigma_{33}) \tag{3.10}$$

This equation can be used to determine the average stress tensors in quasi-isotropic crystalline materials.

The energy difference between the laboratory X-ray and high-energy synchrotron radiation leads to a different penetration depth of the material, thus resulting in separate calculation methods. Due to the low penetration depth of the laboratory X-ray (about 10 $\mu m$), $\sigma_{23}$ and $\sigma_{33}$ and $\sigma_{13}$ are always assumed to be zero, allowing equation 3.10 to be written as:

$$\varepsilon_{\varphi,\psi}^{hkl} = \frac{1}{2}S_2^{hkl}sin^2\psi(\sigma_{11}cos^2\varphi + \sigma_{12}sin2\varphi + \sigma_{22}sin^2\varphi) + S_1^{hkl}(\sigma_{11} + \sigma_{22}) \tag{3.11}$$

with $\sigma_\varphi = \sigma_{11}cos^2\varphi + \sigma_{12}sin2\varphi + \sigma_{22}sin^2\varphi$ and the derivation of $\frac{d\varepsilon_{\varphi,\psi}^{hkl}}{dsin^2\psi}$ follows:

$$\frac{d\varepsilon_{\varphi,\psi}^{hkl}}{dsin^2\psi} = \frac{1}{2}S_2^{hkl}\sigma_\varphi \tag{3.12}$$

The stress value $\sigma_\varphi$ is then directly obtained from the slope $m$ of $\frac{d\varepsilon_{\varphi,\psi}^{hkl}}{dsin^2\psi}$. By tilting $\psi$ to various angles to get slopes of $\varphi$=0°, 45° and 90° (or some other three $\varphi$ positions), the two dimensional stress tensors can be determined without knowing the stress-free lattice spacing of the material. This is the well-known $sin^2\psi$-method which is particularly suited for applications in industrial practice. The measuring principle is shown in Fig. 3.3.3.

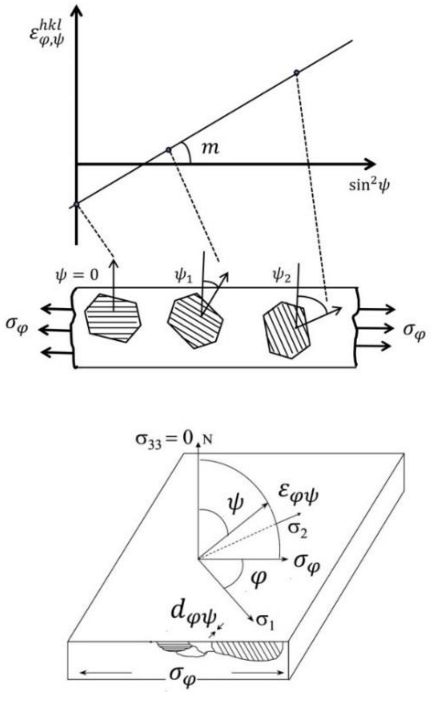

**Fig. 3.3.3:** Principle of the $sin^2\psi$-method for residual stress measurement.

High-energy synchrotron radiation, as the name suggests, contains high X-ray energy, resulting in higher penetration depth. Normally, specimens are prepared sufficiently thin for incident beams to transmit. A fast read 2D detector is mounted behind to record the diffracted patterns. Fig. 3.3.4 gives a schematic illustration of this setup.

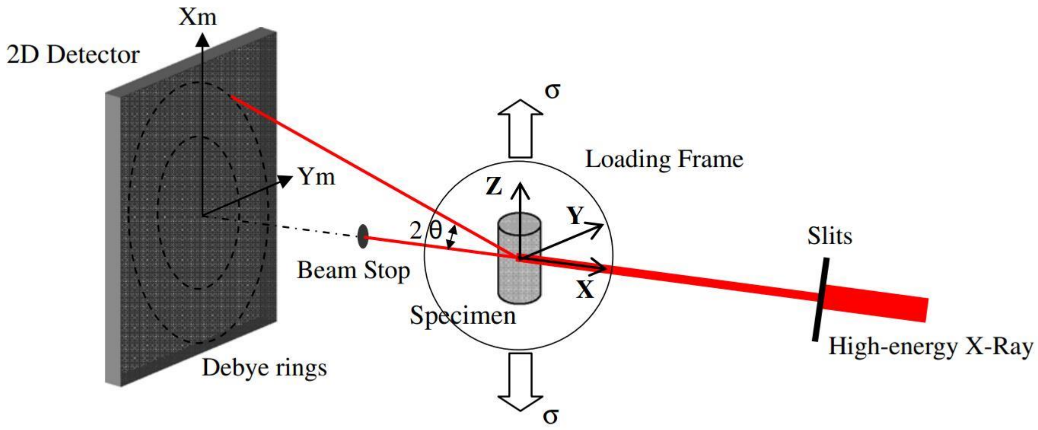

**Fig. 3.3.4:** Schematic showing the working principle of the high energy synchrotron radiation technique [86].

The theoretical principle of this technique for residual stress determination is according to the following equations:

$$1/E^{hkl} = 2d^{hkl} sin\theta/hc \tag{3.13}$$

$$\varepsilon_{\varphi}^{hkl} = (d_{\varphi}^{hkl} - d_0)/d_0 \tag{3.14}$$

where $h$ is Planck's constant, $c$ is the speed of light, and $d^{hkl}$, $2\theta$, $E^{hkl}$ are the lattice spacing, scattering angle and energy of the (*hkl*) plane reflection, respectively. In equation 3.14, $\varepsilon_{\varphi}^{hkl}$ denotes the strain of the (*hkl*) plane in the $\varphi$ direction with the loading axis Z, $d_{\varphi}^{hkl}$ and $d_0$ represent the lattice spacing of the (*hkl*) plane in the $\varphi$ direction and the stress-free lattice spacing. As can be seen from the two equations, the characteristics of the strain measurement are that: a) an arbitrary strain (strain mapping) can be obtained, b) the strain obtained is an average strain for the measured gauge, namely beneath the surface and c) the accuracy of the measurement is dependent on the stress-free lattice spacing. Specifically, when the strains along $X_m$ and $Y_m$ (shown in Fig. 3.3.4) are obtained, the (residual) stress tensors can be calculated as:

$$\sigma_{ij} = \frac{1}{S_2/2}[\varepsilon_{ij} + \frac{S_1}{S_2/2+3S_1}\delta_{ij}\varepsilon_{kk}] \tag{3.15}$$

where $\delta$ is the Kronecker $\delta$-function ($\delta = 1$ for $i = j$, $\delta = 0$ for $i \neq j$), and $\varepsilon_{kk} = \varepsilon_{11} + \varepsilon_{22} + \varepsilon_{33}$.

For two-phase materials, the stress tensors determined above are the total stress tensors. They are composed of macro and micro stress tensors which can be separated and determined only when the volume fractions are known. The principles are according to the following equations:

$$< \sigma_{ij,t}^{\alpha} >= \sigma_{ij,M}+< \sigma_{ij,m}^{\alpha} > \tag{3.16}$$

$$< \sigma_{ij,t}^{\gamma} >= \sigma_{ij,M}+< \sigma_{ij,m}^{\gamma} > \tag{3.17}$$

$$< \sigma_{ij,m}^{\alpha} > V_f+< \sigma_{ij,m}^{\gamma} > \left(1 - V_f\right) = 0 \tag{3.18}$$

where $\sigma_{ij,M}$ represents the macro residual stress, $< \sigma^{\alpha}_{ij,t} >$ and $< \sigma^{\alpha}_{ij,m} >$ are the mean measured total residual stresses and required micro residual stress for the α phase, and $V_f$ is the volume fraction of α phase. Symbols with the same sub- or superscript have the same meaning for the γ phase.

## 3.4 Digital image correlation

DIC is a non-contact optical technique which has been increasing use as of late. Advances in computer technology and high-resolution digital cameras enable this technique to determine the mechanical strain on the micro- and nano-scales.

The principle of this technique is to track the position of the physical points shown in a reference image and a deformed image. The coordinate $(x^*, y^*)$ after deformation relates to the coordinate $(x, y)$ before deformation. The displacement gradients are assumed to be constant throughout the subset, and so the coordinate $(x^*, y^*)$ is expressed as:

$$x^* = x + u_x + \frac{\partial u_x}{\partial x}\Delta x + \frac{\partial u_x}{\partial y}\Delta y \tag{3.19}$$

$$y^* = y + u_y + \frac{\partial u_y}{\partial x}\Delta x + \frac{\partial u_y}{\partial y}\Delta y \tag{3.20}$$

where $\Delta x$ and $\Delta y$ are the $x$ and $y$ direction components of the distance from the centre of the subset to the point $(x, y)$ respectively. $u_x$ and $u_y$ are translations of the centre of the sub-image in the $x$ and $y$ directions. The Lagrangian strains can be calculated as:

$$\varepsilon_{xx} = u_x + 0.5(u_x^2 + u_y^2) \tag{3.21}$$

$$\varepsilon_{yy} = u_y + 0.5(u_x^2 + u_y^2) \tag{3.22}$$

$$\varepsilon_{xy} = 0.5(u_x + u_y) \tag{3.23}$$

In the present study, strain mappings were obtained by in-situ and ex-situ experiments. A flat specimen was loaded step by step to a total strain of 0.15%, during which the strain distribution of the DSS was measured. Subsequently, the specimen was fatigued to different load cycles. An identical experiment procedure was carried out in order to investigate the strain redistribution during tensile loading. During the fatigue interruptions, residual strains were determined (without external stress) to investigate the local damage accumulation and the crack formation.

# 4 Results and discussion

In this chapter, cyclic responses of the DSS 1.4462 in the VHCF regime are presented. This chapter is divided into five sections. Residual stress development in VHCF and HCF is shown in section 4.1. Damage evolution with respect to the formation of slip markings, evolution of micro-hardness and variation of dislocations is shown in section 4.2. Stress partitioning and strain distribution in austenite and ferrite during in-situ tensile experiments are described in sections 4.3 and 4.4, respectively. On the basis of all of experimental findings, modelling of crack initiation is performed in the last section.

## 4.1 Fatigue-induced residual stress redistribution

### 4.1.1 Residual stress development in VHCF

Residual stress determination was performed by means of high-energy synchrotron radiation XRD at the PETRAIII P07 beamline at Deutsche Elektronen-Synchrotron (DESY). A beam with a photon energy of 87 keV and a diameter of 50 μm was used. The high photon energy allows the beam to transmit through the whole specimen thickness (2.5 mm). The diffracted beam was recorded by a fast read-out image plate 2D-detector (2048×2048 pixels) with a 0.2 mm pixel size. During recording, a rocking curve of ±2.0° with a step size of 0.05° rotating around the specimen axis was made to ensure that more grains are involved and the influence of the rolling texture is reduced. After the initial measurement, the specimen was fatigued in an ultrasonic fatigue machine which was fixed on the stage of the beamline at the stress amplitude of 380 MPa. The experiment was interrupted after $10^n$ and $5\times10^n$ (n=4, 5, 6) load cycles in order to measure the evolution of the residual stresses. During the whole experiment, the geometrical relationship between the fatigue sample and the synchrotron beam was kept constant to acquire ex-situ measurements.

The principle of synchrotron radiation XRD for residual stress determination was described in section 3.3, where emphasised that knowing the stress-free lattice spacing $d_0$ is crucial. For single-phase materials, $d_0$ can be obtained by measuring the powder material where no internal residual stresses are expected. For dual-phase materials, in some previous studies [86-88], lattice spacing in the initial state of the material was considered as stress-free and residual stresses measured later reveal relative development. In the present study, this difficulty was overcome by the following method: a specimen was placed into a sulfuric acid solution (1 M with 0.2 M NaCl) at 60 °C for 20 h to dissolve the ferrite grains on the surface. The austenitic phase that is isolated and can be considered as stress-free. Fig. 4.1.1 shows the 3D morphology of the surface measured by confocal laser microscopy. The ferritic phase on the surface is etched to a depth of about 70 μm and exhibits a blue or purple colour, while the austenitic phase exists as an island and shows a green or orange colour. Considering that the penetration depth of the laboratory X-ray beam is about 10 μm for steels, the measured island austenite on the surface can be considered stress-free. Subsequently, the lattice spacing of the stress-free austenite was determined by means of XRD.

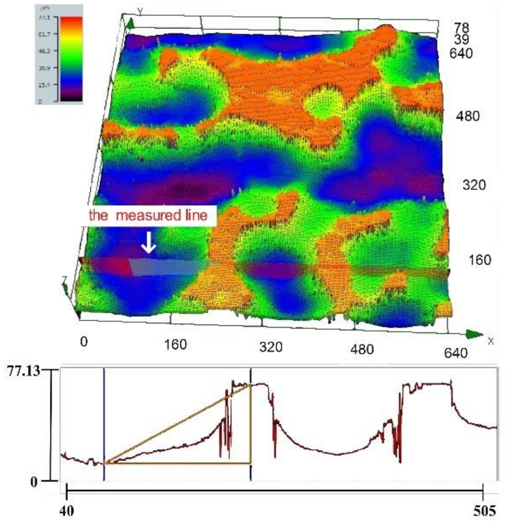

**Fig. 4.1.1:** 3D morphology of the etched surface showing the island austenite grains located in the ferrite matrix (the upper figure) and the dissolution depth (the bottom figure).

Three different (*hkl*) plane families (220), (311) and (222) were selected to determine the lattice spacing of the stress-free austenite. Such plane families having higher reflection angles reduce instrumental and artificial errors. By using the Nelson-Riley extrapolation, where the lattice spacing is plotted against the Nelson-Riley function $(\frac{cos^2\theta}{sin\theta} + \frac{cos\theta}{\theta})$ to minimise the instrument error as shown in Fig. 4.1.2, $d_0$ is found to be 3.60536 ± 0.00053 Å. The lattice spacing for unstressed ferrite was calculated according to the stress equilibrium conditions as 2.88158 ± 0.00047 Å.

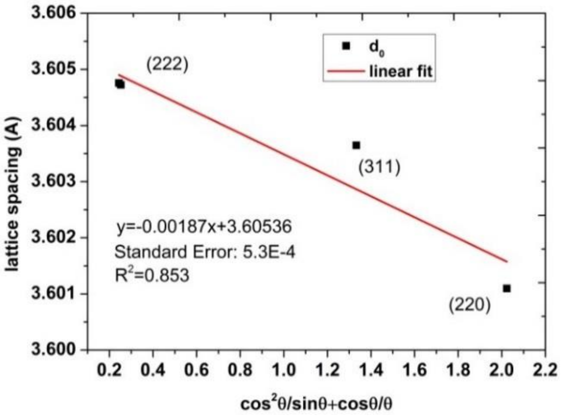

**Fig. 4.1.2:** Determination of the lattice spacing by using Nelson-Riley extrapolation.

Using equations 3.14–3.18, residual stresses were eventually determined. The results of the specimen measured with synchrotron radiation at the stress amplitude of 380 MPa are illustrated below.

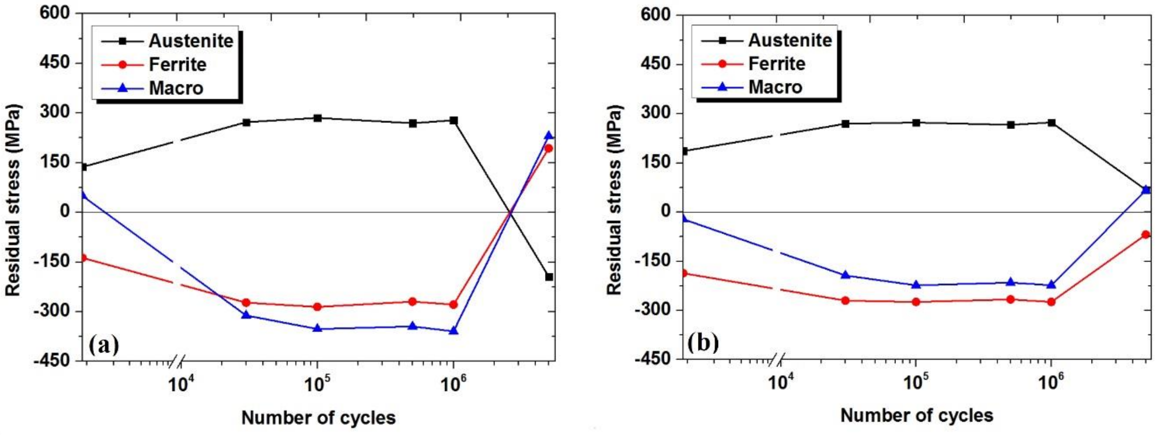

**Fig. 4.1.3:** Residual stress evolution measured by synchrotron radiation XRD a) longitudinal direction, $\sigma_{11}$ and b) transverse direction, $\sigma_{22}$ ($\Delta\sigma/2$=380 MPa, R=−1).

The following conclusions can be drawn from Fig. 4.1.3:

- The initial micro residual stress in austenite is approximately 137 MPa in the longitudinal direction and is 186 MPa in the transverse direction.
- The ferrite phase exhibits very similar absolute micro residual stress values, but as negative values i.e., compressive stress, fulfilling the mechanical equilibrium conditions.
- A redistribution of micro residual stresses in terms of an increase in tensile micro residual stress in austenite and a decrease in compressive micro residual stress in ferrite is observed at a fatigue load cycle number of $N=5\times10^7$.
- After $N=5\times10^7$ fatigue load cycles, the difference between the micro residual stress of the two phases decreases.

In order to confirm the development of the micro residual stresses in VHCF, an additional experiment was carried out by means of laboratory XRD. The initial values of the residual stress for both phases were first evaluated. Subsequently, the specimen was fatigued to different load cycles at a stress amplitude of 360 MPa. Finally, development of the residual stresses was monitored discontinuously and the results are illustrated in Fig. 4.1.4.

Residual stress development of the second specimen exhibits a similar tendency as the first one. Again, micro residual stress in austenite is observed to increase at $10^7$ cycles and reaches a maximum at the fatigue load cycle number of $N=5\times10^7$. Micro residual stress in ferrite, however, begins to decrease after $10^7$ cycles and reaches a minimum at a fatigue load cycle number of $N=5\times10^7$. Further fatigue loading appears to lead to micro residual stress relaxation. What differs from the first specimen is the initial value of the residual stresses. This may be attributed to the different measuring principles between the two methods: (a) the effectively measured volume for laboratory XRD is only the surface while for synchrotron radiation XRD it is the subsurface; (b) the absolute value of the synchrotron radiation XRD depends on the absolute lattice spacing but does not for laboratory XRD; (c) the initial states of the two specimens are not identical, i.e., the specimen for laboratory XRD method has a lower macro residual stress.

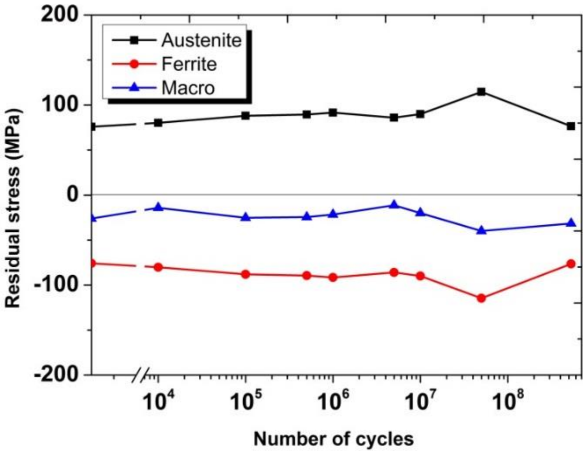

**Fig. 4.1.4:** Residual stress (longitudinal direction, $\sigma_{11}$) development ($\Delta\sigma/2$=360 MPa).

### 4.1.2 Development of residual stresses in HCF

In VHCF, catastrophic failure is usually caused by the accumulation of scarce damages during repeated loading. Such scarce damages actually lead to unnoticeable changes of the material, such as in the temperature of the specimen, micro-crack propagation or residual stresses in this case. Any artificial errors may lead to inaccuracy. In order to confirm the measuring technique and find the mechanism of the residual stresses' evolution, experiments in HCF were performed. Four specimens were prepared with the geometry shown in Fig. 3.1.3 and fatigued in a servo-hydraulic fatigue machine of type MTS 810 under stress control conditions. The tests were divided into two groups. The first two samples were tested at stress amplitudes of 450 and 500 MPa to obtain the cyclic deformation response; the cyclic deformation curves under the two conditions are illustrated in Fig. 4.1.5. The other two samples were fatigued to different cycles to determine the evolution of residual stresses.

The two specimens under distinct stress amplitudes exhibit preliminary hardening in the first cycle followed by continuous cyclic softening. The same results were observed by Mateo and Lianes et al. [89, 90] who claimed that in HCF the DSS exhibits rapid hardening during the first cycle and slow cyclic softening in the following cycles. At a very low-stress amplitude (330 MPa), however, no cyclic hardening was observed, but only rapid cyclic softening. Xia et al. [91] investigated another grade of DSS (17Cr-14Mn-2Mo-0.7Si-0.25N-0.06C) in two different heat treatment conditions, and found that the DSS initially hardened followed by a continuous softening. Sahu [16] studied the same DSS as in the present study in strain control and observed rapid cyclic hardening followed by cyclic softening.

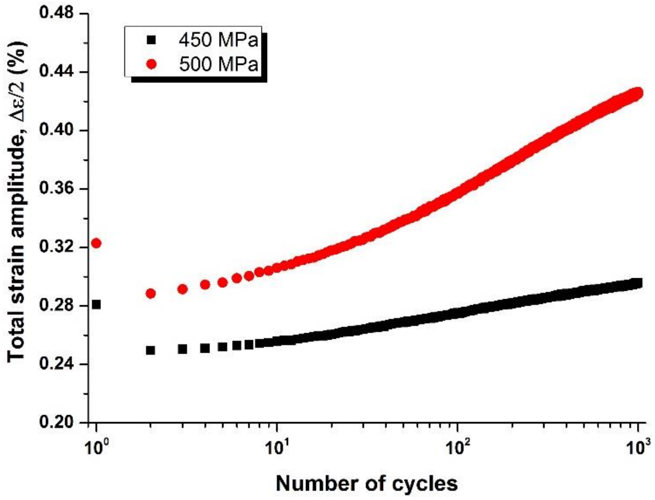

**Fig. 4.1.5:** Cyclic deformation curves of the constant stress controlled tests in HCF as a representation of the total strain amplitude vs the number of cycles in a logarithmic scale.

Subsequently, experiments on residual stress evolution for the other two specimens were executed at the cyclic hardening and cyclic softening stages. Interruptions were performed at fatigue load cycle numbers of N=5, 20, 50, 100, 200, 300, 400, 500 and 600. Residual stress development at further fatigue cycles (for example at the stage of crack propagation or fracture stage) is not in the scope of this thesis and thus is not in consideration. After each interruption, a gradual decrease in the stress amplitudes from its maximum value to zero was applied to ensure that no residual load stress or residual load strain exists in the specimens. A representation of the load signal is shown in Fig. 4.1.6.

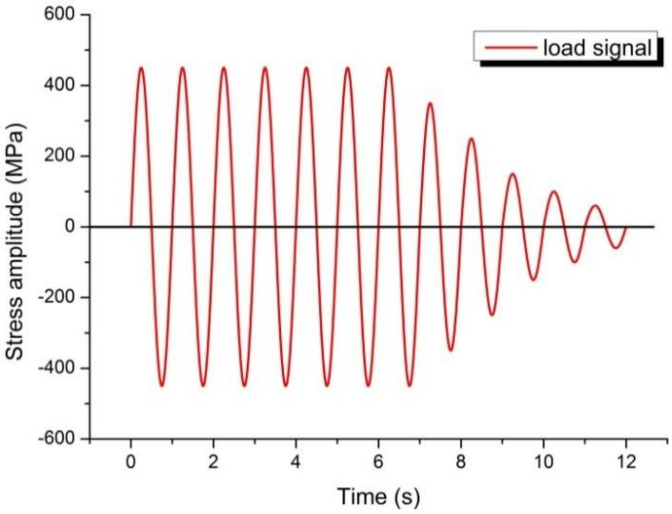

**Fig. 4.1.6:** A representation of the interruption's load signal in HCF showing a gradual decrease in the stress amplitude.

Residual stress determination for the two specimens was performed by means of laboratory XRD. The results of the two cases are shown in Fig. 4.1.7.

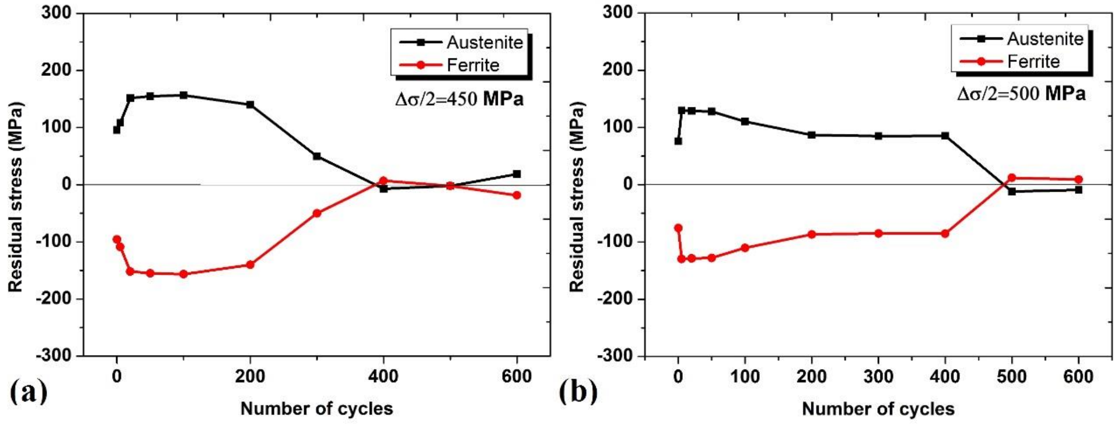

**Fig. 4.1.7:** Residual stress development in HCF: a) 450 MPa and b) 500 MPa.

The following conclusions can be drawn from these two specimens:

- Tensile micro residual stress in austenite and compressive micro residual stress in ferrite are observed.
- Residual stress development in HCF exhibits a similar trend as that in VHCF. Again, an increase in the internal residual stress in each phase is observed. However, it requires fewer fatigue load cycles compared with VHCF (about $10^7$).
- With further fatigue load cycles, internal residual stresses decrease for both cases.
- Micro residual stresses appear to vanish after more than 500 fatigue load cycles.

Residual stress determination in HCF was also performed by means of high energy synchrotron radiation XRD. An hourglass-shaped specimen was mounted at the ultrasonic fatigue machine and fatigued at a stress amplitude of 400 MPa with fully repeated tensile-compressive load mode. Interruptions were made at fatigue load cycles of N=2×$10^4$, $10^5$, 5×$10^5$, $10^6$ and 5×$10^6$. The results are illustrated in Fig. 4.1.8.

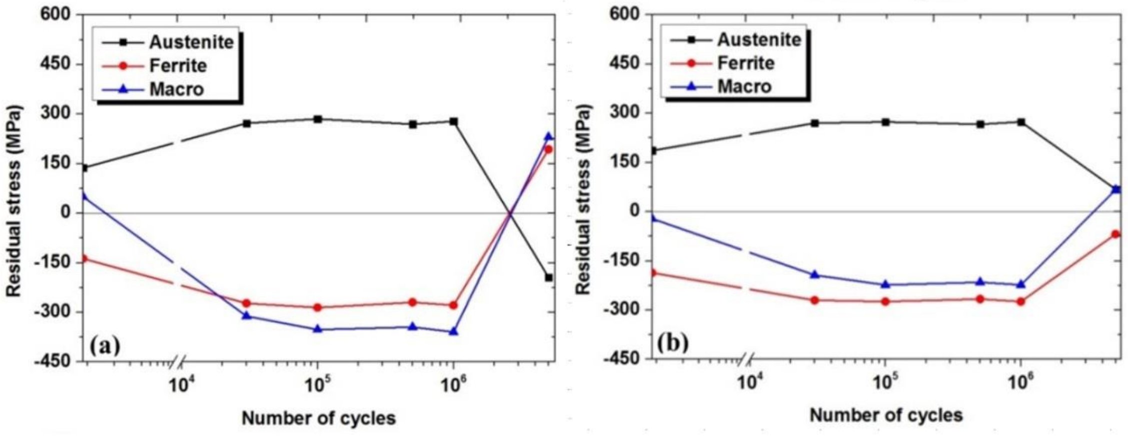

**Fig. 4.1.8:** Residual stress evolution measured by synchrotron radiation XRD a) longitudinal direction, $\sigma_{11}$ and b) transverse direction, $\sigma_{22}$ (Δσ/2=400 MPa).

The development of residual stresses in HCF exhibits similar behaviour as that measured by laboratory XRD (Fig. 4.1.7). However, the initial micro residual stresses in both phases exhibit different values. This is likely due to the different sample geometries. Specimens used for the servo-hydraulic fatigue machine have a diameter of 7 mm, while specimens for the ultrasonic fatigue machine have a diameter of 2.5 mm. The two types of specimen underwent different cooling speeds during quenching. Although the raw rolling bars have the same diameter, the different cooling speeds in different parts of the specimen yield distinct residual stresses.

### 4.1.3 Discussion on residual stress development

Micro residual stress variation is directly related to microstructural changes, e.g., dislocation multiplication, annihilation or rearrangement. When a material deforms, micro residual stresses in terms of the second type and the third type build up. The second type of residual stress is actually the result of back stresses due to dislocation pile-ups at grain or phase boundaries and elastically strained the second phase of heterogeneous materials. If these dislocations move in the reverse direction during localised plastic deformation, the back stresses and as such the directed micro residual stresses are initially reduced. Further deformation causes renewed build-up of back stresses in the opposing direction accompanied with dislocation multiplication and hardening, which again increases the micro residual stresses. Dislocation rearrangement in tangles or cell structures results in inhomogeneous micro residual stresses. Such arrangements are in a lower energy state and lead to micro residual stress relaxation. If new dislocations are generated, the build-up micro residual stresses are a superposition of the original and the newly generated micro residual stresses [68]. During dislocation multiplication, dislocations glide and interact with each other. The annihilation of dislocations gives rise to voids, causing distortions of the lattice structures. Eventually, a third type of residual stress is generated.

According to the above description, the development of micro residual stresses investigated in this study is related to dislocation behaviour. In macroscopic respective, the development of residual stresses should occur at the cyclic hardening and cyclic softening transitions. In HCF, an initial hardening of the material is observed as noted by the black and red symbols in Fig. 4.1.5. Correspondingly, an increase in internal residual stresses is shown in Fig. 4.1.7. Subsequently, cyclic softening takes place, during which plasticity transmission frequently occurs. Moreover, dislocations rearrange themselves into a lower energy state. The two reasons lead to a decrease in the difference of internal residual stresses between the two phases.

The measured micro residual stresses actually consist of two parts: an increase in the micro residual stresses caused by dislocation pile-ups, and a decrease in the micro residual stresses induced by dislocation transmission or rearrangement. The two factors determine the development of the micro residual stresses.

At a stress amplitude of 450 MPa, an increase in the internal residual stresses is observed within the first 100 cycles. As described, this is likely due to the dislocation pile-ups at the phase boundary. At a stress amplitude of 500 MPa, identical behaviour of the micro residual stresses is observed; however, the increase in the internal residual stresses is limited to the first 50 load cycles. The change of the micro residual stresses is likely due to the dislocations rearranging in a low energy state. This anticipations regarding the dislocation arrangement are confirmed by TEM as shown in Fig. 4.1.9. At both stress amplitudes, strong dislocation pile-ups are observed in austenite. At the stress amplitude of 500 MPa however, dislocation pile-ups in austenite begin to form cell structures to decrease the energy state. In ferrite, randomly distributed dislocations start to form cell structures for the first case while for the latter dislocations exist as cell structures in a low energy state.

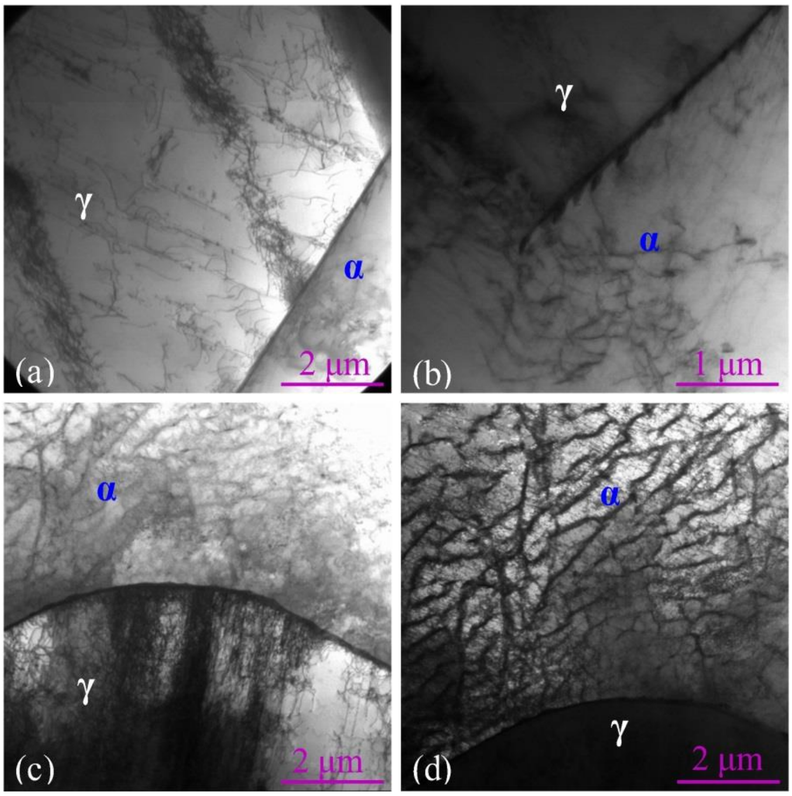

**Fig. 4.1.9:** TEM micrographs in HCF showing a) dislocation pile-ups in austenite, b) randomly distributed dislocations start to form cell structures, c) strong dislocation pile-ups in austenite and the beginning of cell structure formation, d) cell structures in ferrite. a) and b) were taken from the specimen at the stress amplitude of 450 MPa, c) and d) were taken from the specimen at the stress amplitude of 500 MPa.

It should be noted that in Fig. 4.1.9 no diffraction patterns are shown. The identification of both phases was done by means of light microscopy. Austenite and ferrite can be distinguished easily as the two phases exhibit different colours. A representation of the identification process is illustrated in Fig. 4.1.10.

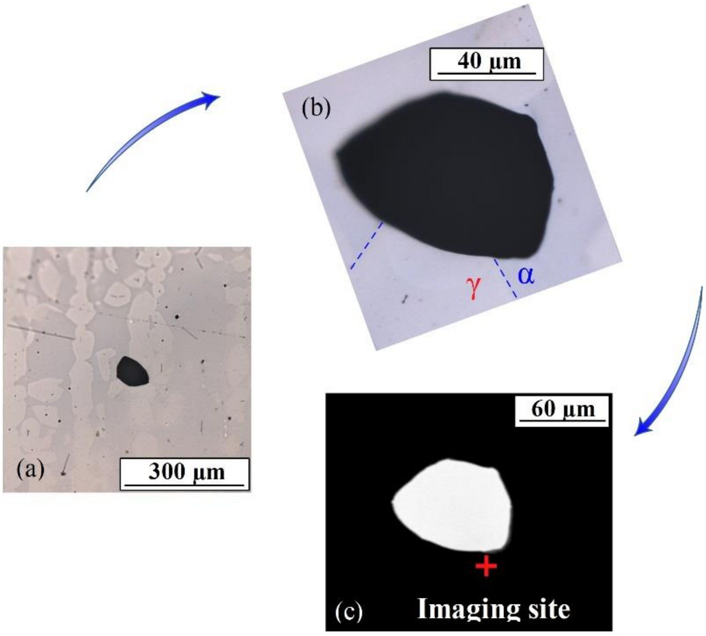

**Fig. 4.1.10:** Phase identification process: a) light microscopy image, b) larger magnification of a) with a 180° rotation angle, and c) TEM image taken from low magnification, the red mark showing the imaging site. By comparison with images b) and c), austenite and ferrite can be identified.

In the literature, fatigue experiments executed in HCF were mostly performed in strain control. Dislocation structures were subsequently characterised for such specimens in both the austenitic and ferritic phases. Kruml et al. [92] characterised two types of dislocation structures in the ferritic phase of the DSS DIN X2CrNiMoN22-5 at $\Delta\varepsilon=4.5\times10^{-3}$. Dislocations in vein and cell structures and a few short walls perpendicular to the direction of primary walls were identified, likely showing the initial stage of biaxial structure formations. Mateo et al. [93] observed cells, wall structures, dense loop patches and poorly defined channels in the ferrite of the DSS SAF 2507 at $\Delta\varepsilon_{pl}=6\times10^{-3}$. Dislocation structures in austenite of DSSs are influenced by two factors: 1) stress (strain) amplitude and 2) nitrogen content. The former promotes glide of secondary slip system and wavy slip. The latter is known to modify the substructure evolution. Higher nitrogen content decreases the stack fault energy of austenite, which promotes a planar slip behaviour of dislocations. The planar slip leads to an increase in fatigue strength inhibiting strain localisation.

Another reason for the decrease in micro residual stresses in HCF is likely the cyclic softening of the material, where dislocation transmission or crack formation is expected. Microstructural feature evolution was therefore characterised for HCF. The stress amplitude applied was 450 MPa. Interruptions were executed at the same fatigue load cycles as that in the residual stress measurement experiments. In the first 200 fatigue cycles, no significant slip markings appear on the surface. At a fatigue load cycle number of N=400 however, relative strong slip markings emerge and micro-crack nuclei or micro-cracks are frequently present as shown in Fig. 4.1.11. This observation agrees well with the cause of residual stress development in HCF as shown in Fig. 4.1.7. Based on this, the micro-crack nuclei or micro-cracks lead to the disappearance of the micro residual stresses.

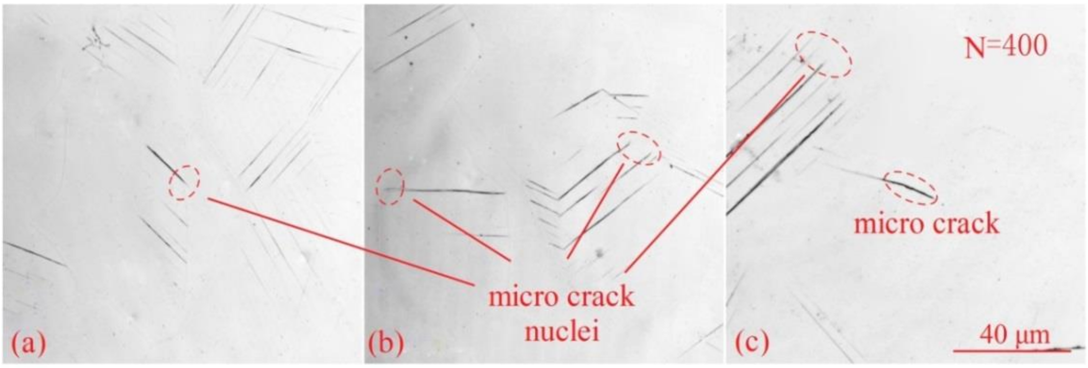

**Fig. 4.1.11:** Optical images showing micro-crack nuclei or micro-cracks existing in HCF at fatigue cycle N=400 ($\Delta\sigma/2$=450 MPa).

In VHCF, the DSS investigated in this study exhibits 'austenitic-like' behaviour, since austenite has a lower yield stress compared with ferrite. During cyclic loading, plastic deformation is mostly carried by the austenitic phase, which determines the plastic deformation behaviour of the DSS. As the plastic deformation in VHCF is very small, no observable cyclic hardening and cyclic softening were found for the whole material [94]. The internal residual stresses between the two phases, however, increase based on Fig. 4.1.3 and Fig. 4.1.4. The contradiction here is the scarce plastic deformation and the appreciable change of the micro residual stresses. Istomin et al. [95], however, have investigated the plastic deformation behaviour of austenite for the same material by means of high-energy synchrotron radiation XRD. A single peak shape of the austenite (131) of ten measured points along the loading axis was investigated during the fatigue process. The results are shown in Fig. 4.1.12.

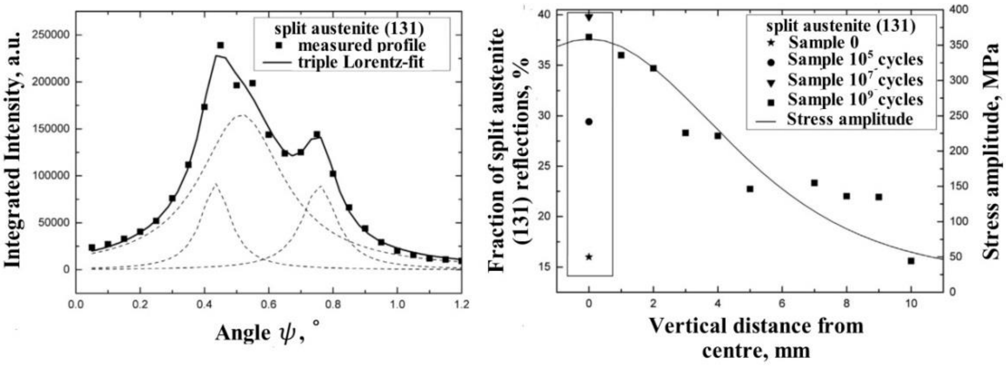

**Fig. 4.1.12:** a) Representation of peak split (131) of an austenite grain measured by means of high energy synchrotron radiation and b) fraction of the split of (131) austenite reflections as a function of vertical distance and comparison to other numbers of load cycles [95].

According to Istomin et al. [95], the split of the (131) diffraction peak is related to the small-angle grain boundary formed by the deformation-induced dislocations in the austenite grains. After $10^7$ fatigue load cycles, nearly 40% of the peaks have split up at the centre point of the specimen. This manifests in that a considerable volume fraction of the austenite grains carry plastic deformation. By increasing the distance from the centre point along the loading axis (vertical distance), the split fraction decreases as less plastic deformation occurs at such points, as shown in Fig. 4.1.12(b). This plastic deformation is directly visible in TEM micrographs however. The images in Fig. 4.1.13 are taken from a fatigued specimen at a lower stress amplitude and a small number of fatigue cycles (345 MPa, fatigue load cycle number of $N=2\times10^5$). Although no obvious slip traces are observed on the surface, dislocation pile-ups are present, indicating that plastic deformation occurs directly in the austenite grain. The invisible volume plastic deformation caused by dislocation pile-ups leads to the development of micro residual stresses in VHCF.

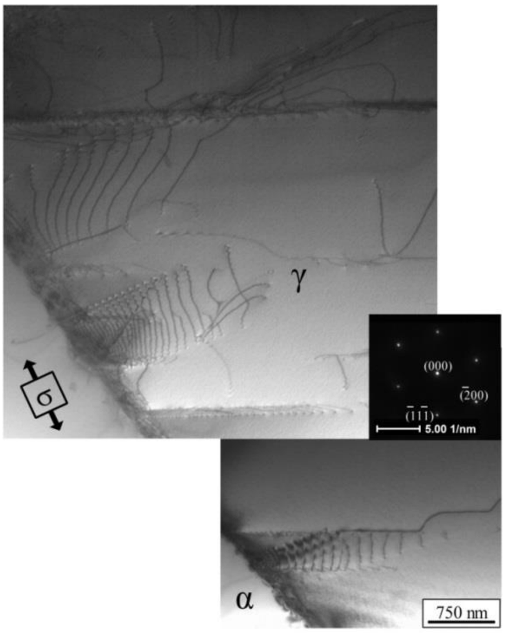

**Fig. 4.1.13:** TEM images taken from the specimen fatigued at a stress amplitude of 345 MPa, $z_\gamma=[011]$.

## 4.2 Damage evolution

### 4.2.1 Formation of slip markings

In this section, fatigue damage in the form of slip markings is considered in order to investigate the fatigue behaviour of the DSS in the VHCF regime. An hourglass specimen with a shallow notch was fatigued up to $2\times10^9$ cycles at a stress amplitude of 345 MPa. Interruptions were performed during the whole fatigue procedure. Confocal laser microscopy providing nanometre scale resolution was used to observe the damage evolution. After $8\times10^4$ fatigue load cycles (the first interruption), six austenitic grains exhibit slip traces, and the width of the slip markings of two grains was quantitatively measured. Subsequently, the specimen was fatigued to different load cycles and interruptions were again performed. The two slip traces were measured after each interruption to determine the slip trace evolution. The result in terms of the width of the slip band versus the number of cycles is shown in Fig. 4.2.1(a) and (b). The depth of slip marking (extrusion and intrusion) is expected to depend on the tilt angle of the specimen (cylindrical) which leads to a large scatter, and thus is not within the scope of the present study.

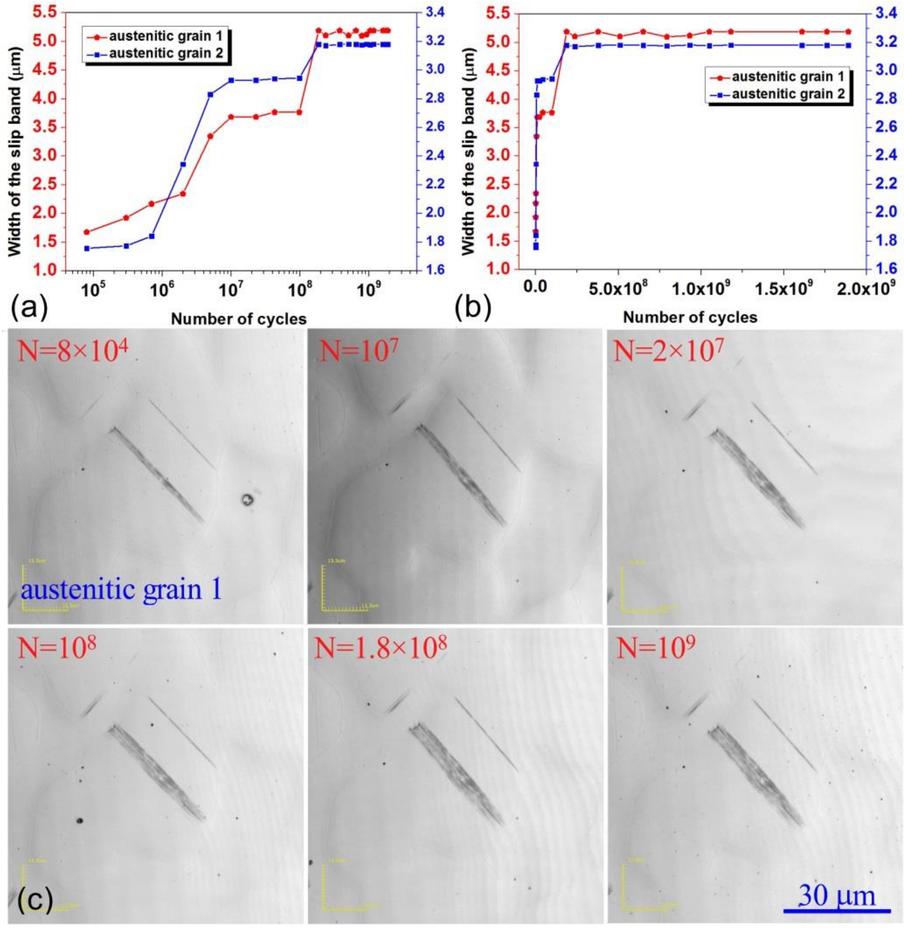

**Fig. 4.2.1:** Evolution of slip markings, with a) and b) showing quantitative plots for two activated grains in logarithmic and linear scales and c) micrographs of the austenitic grain 1 taken by means of confocal laser microscopy.

Fig. 4.2.1(a) shows the growth of two slip markings in width, exhibiting similar damage evolution behaviour. At the very early stage, the two slip markings broaden continuously in the first $10^7$ load cycles. Subsequently, they stay unchanged until $10^8$ load cycles, followed by broadening again for almost another $10^8$ load cycles. At a fatigue load cycle number of N=1.8×$10^8$, the growth stops and the width remains constant for the remaining load cycles. Optical images of one slip marking in Fig. 4.2.1(c) show the two transitions clearly.

As outlined in section 4.1, dislocation pile-ups are characterised as the main features of the DSS in VHCF. Dislocations pile against the phase boundaries, leading to nearby stress concentration. Hence, an increase in internal residual stresses is expected. In Fig. 4.2.1, the two slip markings at the same stage (at the load cycle number of $N=2\times10^7$) are observed to stop growing, i.e., no further plastic deformation in the austenite grain occurs afterwards. It appears that the yield stress for austenite becomes higher, indicating that cyclic hardening takes place. After $10^8$ fatigue load cycles, slip traces become broader, likely due to the cyclic softening of the austenite.

To confirm the evolution of the slip traces of the DSS in VHCF, two more specimens were tested at different stress amplitudes. In order to verify that such behaviour belongs to the DSS intrinsically, the two specimens were fatigued in an electromagnetic resonance system (stress control). Evolution of the slip traces is shown in Fig. 4.2.2 and Fig. 4.2.3.

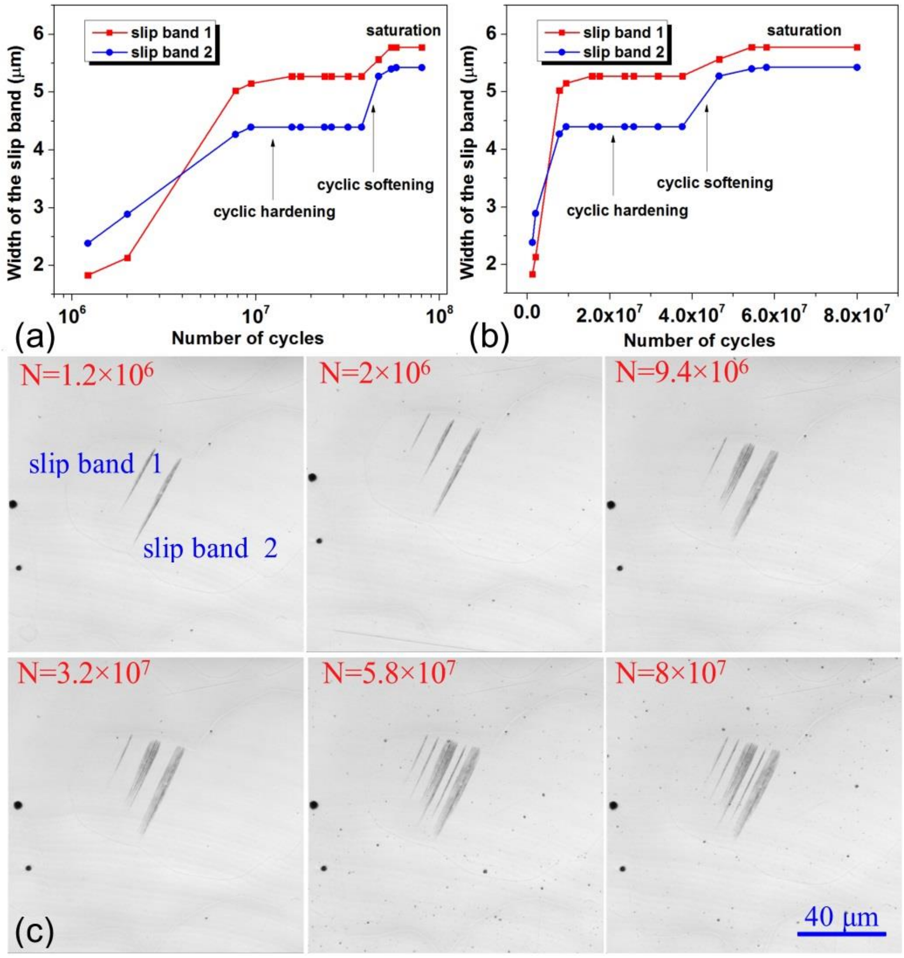

**Fig. 4.2.2:** Evolution of slip markings in the second specimen; a) and b) show quantitative plots in logarithmic and linear scales, while c) shows micrographs taken by means of confocal laser microscopy ($\Delta\sigma/2=330$ MPa).

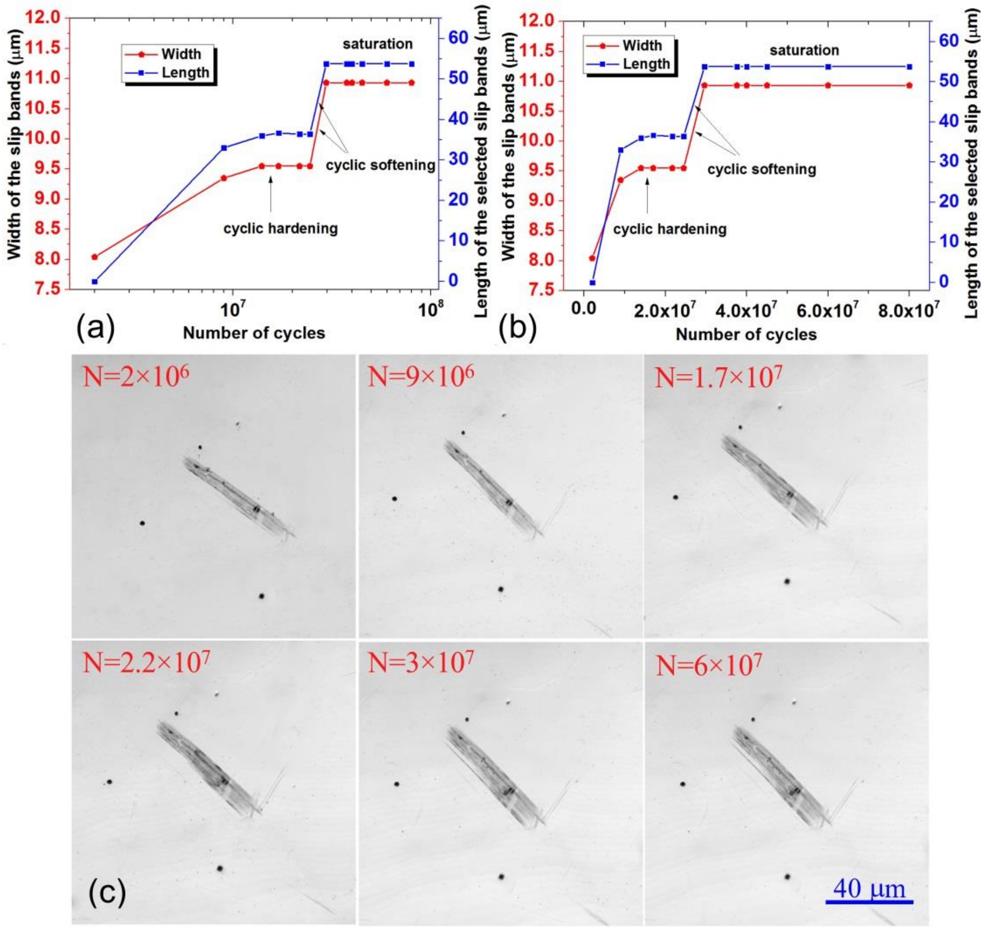

**Fig. 4.2.3:** Evolution of slip markings in the third specimen; a) and b) show quantitative plots in logarithmic and linear scales, and c) shows micrographs taken by means of confocal laser microscopy ($\Delta\sigma/2$=340 MPa).

Slip markings in Fig. 4.2.2 and Fig. 4.2.3 exhibit similar growth behaviour compared with Fig. 4.2.1. Additionally, the length of one slip marking is also investigated in Fig. 4.2.3. The growth tendency is identical with that of the width of the slip marking. Cyclic hardening and cyclic softening in the two cases appear at different numbers of cycles, which are a function of the applied stress (330 MPa and 340 MPa).

Development of slip markings indicates that the cyclic deformation behaviour of the austenite is noticeable in VHCF. No appreciable changes are observable in ferrite. The whole material thus exhibits austenite-like behaviour. Evolution of slip markings can be attributed to cyclic hardening and cyclic softening of austenite. Such cyclic behaviour is directly linked to dislocation motion and multiplication in nature. In this case, dislocations pile-ups at the phase boundary are expected to cause cyclic hardening of the austenite grains, whereas dislocation transmission through the phase boundary in the later stage of fatigue likely leads to cyclic softening of the austenite grains.

### 4.2.2 Characterisation of micro-hardness

As discussed, cyclic hardening and cyclic softening of austenite are the main phenomena of the DSS investigated in VHCF. It is well known that hardening of one phase is directly related to the specific hardness. Therefore, confirmation of the hardness of the austenite in VHCF is essential for further studies. In this section, the micro-hardness of the austenite was determined by means of nanoindentation tests. Three austenite grains with slip markings were randomly selected initially. Subsequently, the specimen was cyclically fatigued to different load cycles, after which micro-hardness tests were performed. Eventually, micro-hardness evolution of the three austenite grains was revealed.

Conventional indentation hardness tests involve the measurement of the size of a residual plastic indentation in the specimen as a function of the indenter load. In a nanoindentation test, the relationship between the depth of the indenter and the load applied is considered. A representation of the loading-unloading curve of the nanoindentation test is shown in Fig. 4.2.4.

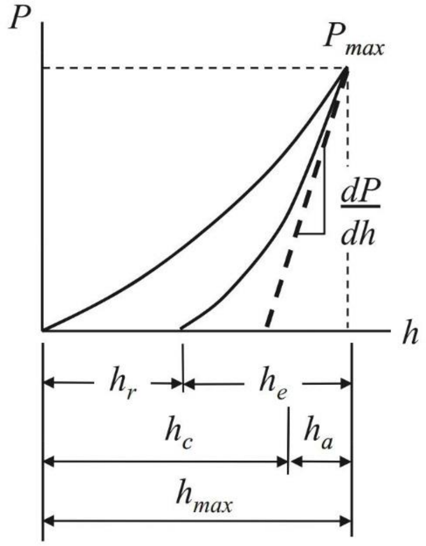

**Fig. 4.2.4:** Compliance curves (loading and unloading) from a nanoindentation experiment with maximum load $P_{max}$ and depth beneath the specimen free surface $h_{max}$. The depth of the contact $h_c$ and slope of the elastic unloading $\mathrm{dP/dh}$ allow the specimen modulus and hardness to be calculated, $h_r$ is the depth of the residual indentation, and $h_e$ is the displacement associated with the elastic deformation during unloading [96].

Micro-hardness can be calculated according to the equations below:

$$\mathrm{H} = \frac{P_{max}}{A} \tag{4.1}$$

$$\mathrm{A} = 24.65 h_c^2 \tag{4.2}$$

In practice, however, different maximum load forces lead to diverse values, resulting in scattered testing. In the present study, a seven-step measurement was implemented in order to acquire more realistic values of the tested grains. A representative loading-unloading curve and a representation of the impression area are illustrated in Fig. 4.2.5.

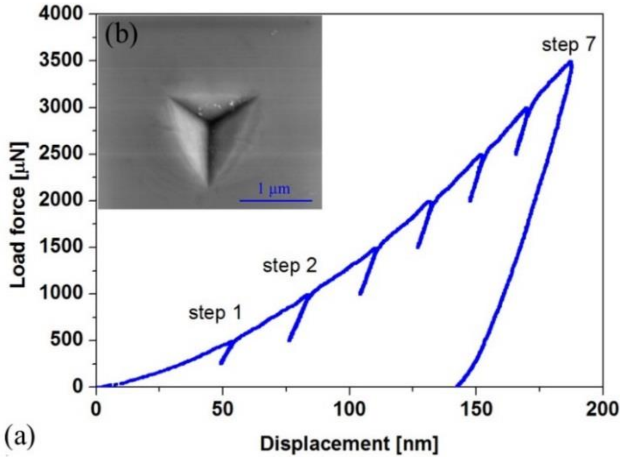

**Fig. 4.2.5:** Representation of a) the seven-step loading-unloading curve of the nanoindentation test and b) indentation area of the nanoindentation test.

Fig. 4.2.6 shows the micro-hardness development of the seven step values of one austenite grain as a function of the cycle numbers. The tendency of the seven curves is almost identical except an unexpected point in the step 4 case at $10^6$ cycles, as marked by a green arrow. All step values at $10^6$ cycles are smaller than at $2\times10^4$ and $2\times10^7$, while the point in step 4 exhibits a larger value than that at $2\times10^7$. Points in such conditions are defined as abnormal points. To confirm the measured values, the abnormal points were statistically analysed.

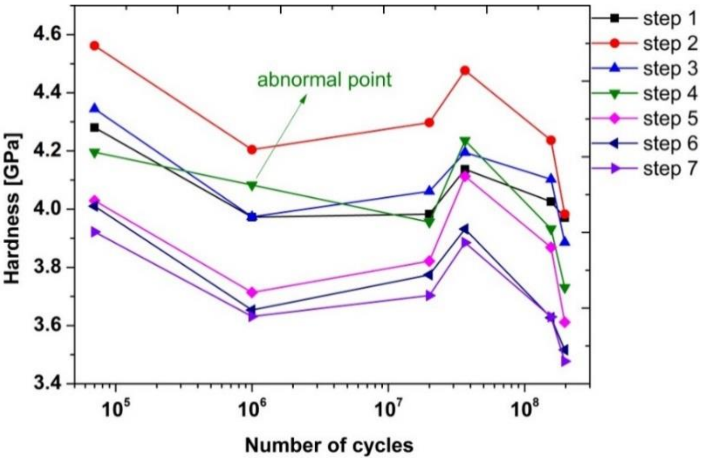

**Fig. 4.2.6:** Development of micro-hardness of one austenite grain measured by the seven-step program as a function of fatigue load cycle number.

It is well known that dislocations strongly affect the hardness of a material. When a hardness test is performed, the plastically deformed indentation area formed by the indenter contains a large number of newly generated dislocations and influences the surroundings. Measurements performed in this zone lead to incorrect results. In the present study, individual measurement was employed (i.e., the newly generated dislocation zones were avoided), when new indentation tests were performed. The micro-hardness evolution of austenite was then determined.

Another factor affecting the hardness measurement is the measuring position, especially when the variations are scarce. In order to assess the position influence and the dependence of the load cycle number, three measurements were performed in an arbitrary austenitic grain at an arbitrary cycle number (the load cycle number selected was $N=1.56\times10^8$). Fig. 4.2.7 shows that the three tested positions give identical values. The standard deviation errors of the three tests are in the range of 0.025 GPa which is negligible compared with the changes caused by cyclic loading (Fig. 4.2.8). Hence, the conclusion can be drawn from the analysis that the change of the micro-hardness does not depend on position, but on cyclic changes.

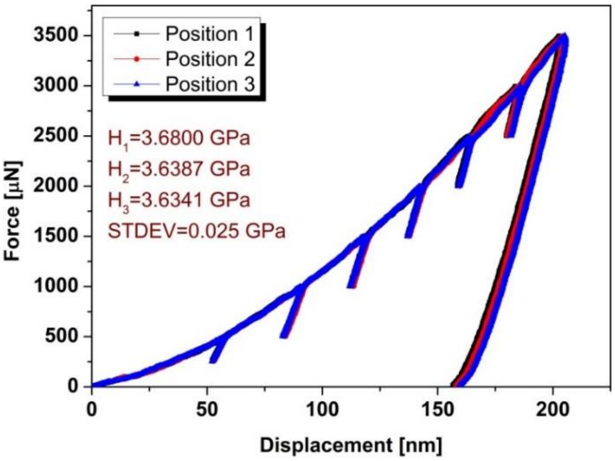

**Fig. 4.2.7:** Micro-hardness of an arbitrary austenitic grain at an arbitrary cycle (at cycle number $N=1.56\times10^8$).

Eventually, the micro-hardness of the three distinct austenite grains was evaluated. The results are illustrated in Fig. 4.2.8(a) where the black, red, blue and pink lines represent the hardness of the first, second, third austenite grain and the mean value of the three grains, respectively. As illustrated, the mean micro-hardness drops considerably from an initial value of 4.29 GPa to 3.91 GPa after $2\times10^7$ fatigue load cycles at the first stage. The tendency for the austenitic grain 3 is more obvious, dropping from 4.53 GPa to 3.82 GPa. Afterwards, the micro-hardness tends to increase up to $3.65\times10^7$ cycles followed again by a decrease. The two transitions shown here are identical with the evolution of slip markings. The increase/decrease in micro-hardness can again be explained by the cyclic hardening/softening of austenite.

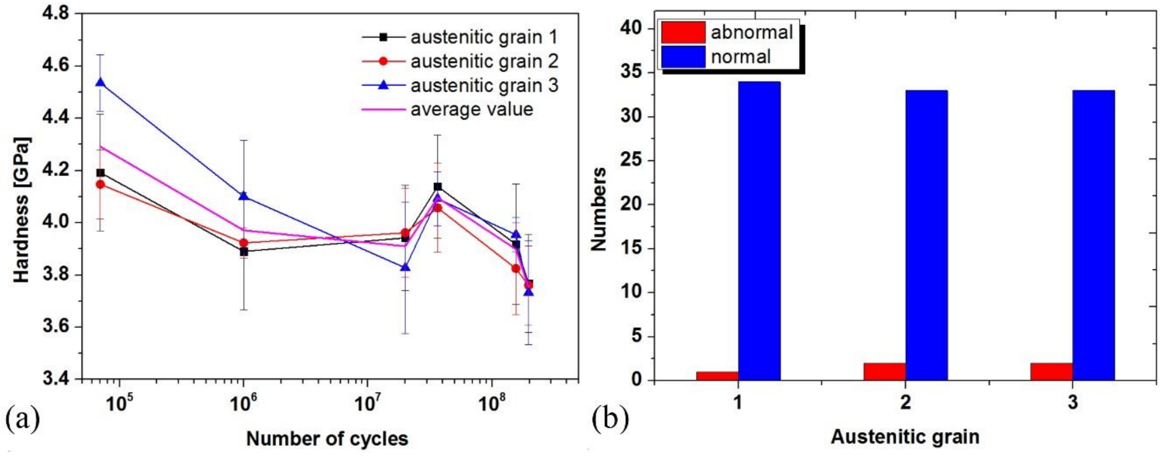

**Fig. 4.2.8:** a) Development of the micro-hardness of the three measured austenite grains and b) number of abnormal points in comparison to normal data points in the three test groups.

Fig. 4.2.8(b) shows the number of abnormal points appearing in the three test groups. The number of abnormal points are negligible (only one or two in each group), indicating that the profiles in Fig. 4.2.8(a) are representative.

The development of micro-hardness in the adjacent ferrite grains was also evaluated. The results plotted in Fig. 4.2.9(a) show no comparable changes of the three ferrite grains. It appears that the development of the micro-hardness in ferrite is irregular, and the abnormal points in the three test groups are more significant than those in austenite. However, it is interesting to see that the micro-hardness values of the measured austenitic and ferritic grains are very similar (3.7–3.8 GPa) after $2\times10^8$ fatigue load cycles. It seems that the material transforms from an inhomogeneous to a homogeneous state after cyclic hardening and cyclic softening transitions.

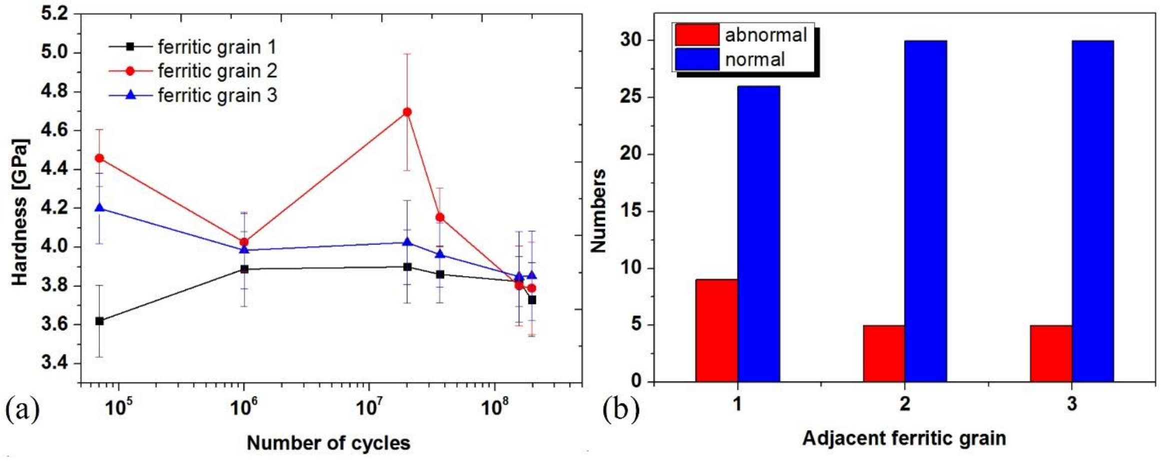

**Fig. 4.2.9:** a) Development of the micro-hardness of the three adjacent ferrite grains and b) abnormal points in the three test groups.

The observations and their discussion presented above confirm that the cyclic hardening and cyclic softening of austenite take place continuously during fatigue loading. The cyclic deformation behaviour of ferrite is more complicated and depends on the interaction with austenite grains and other factors. It is interesting to note however that after cyclic hardening and cyclic softening of austenite, the material establishes a homogeneous state which determines the micro-crack formation in VHCF and will be discussed in section 4.5.

### 4.2.3 Variation of dislocation densities and arrangements

The intrinsic behaviour of plastic deformation is directly related to dislocation motion. Dislocations glide back and forth during symmetric loading. In practice, irreversible dislocation motions occur due to physical interactions between the material, the surrounding conditions, and the complexity of dislocation motion itself, as described in the introduction section. As long as the irreversible dislocation motion is not completely eliminated, accumulation of plastic slip takes place. Moreover, dislocation multiplication occurs during cyclic loading, giving rise to an increase in dislocation density. The newly generated dislocations cross glide or interact with each other, leading to hardening of the materials. As discussed previously, cyclic hardening and cyclic softening of austenite caused by dislocation motion were observed. In VHCF, slight damages are frequently identified as typical characteristics. Catastrophic failure can be caused by the accumulation of slight variations. Thus, the detection of such slight variations in terms of dislocation density and arrangement is necessary. In this section, the dislocation density of austenite and ferrite during fatigue was assessed by a modified Williamson-Hall method. Experiments were carried out at PETRAIII in Hamburg by means of high energy synchrotron radiation XRD. Dislocation arrangements were investigated by means of TEM.

Line profile analysis is an indirect method for determination of microstructure in terms of dislocation density and subgrain size in crystalline materials [97, 98]. Williamson-Hall peak analysis suggests that broadening of peak profiles is related to small subgrains or lattice distortions, especially dislocations. Their contributions can be evaluated separately on the basis of their different (*hkl*) dependences. However, this becomes less accurate for highly anisotropic materials. Dislocation determination in the present work was calculated using the modified Williamson-Hall plot. The calculation details can be found in the appendix. The dislocation density in the longitudinal and transverse directions of austenite and ferrite are assessed, as illustrated in Fig. 4.2.10.

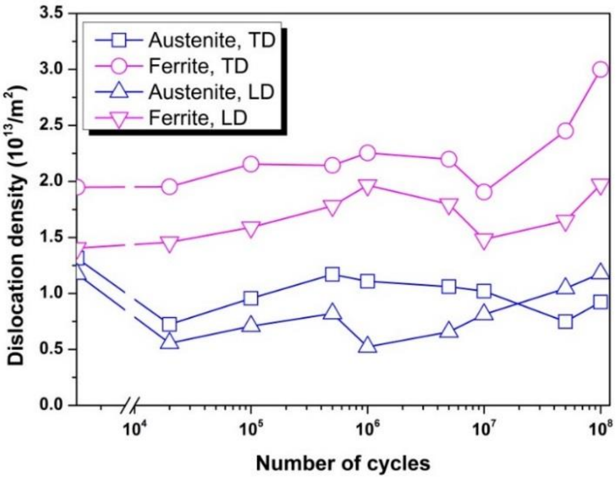

**Fig. 4.2.10:** Development of the dislocation density of austenite and ferrite in the longitudinal direction (LD) and transverse direction (TD).

The following conclusions can be drawn from Fig. 4.2.10:

- The dislocation density in austenite decreases after the initial $10^3$ cycles in both directions. An increase in dislocation density is observed at a fatigue load cycle number of $N=2\times10^4$, followed by a slight decrease. After $10^8$ load cycles, the dislocation density in austenite has increased to an identical level compared to the initial state.
- Dislocation density in ferrite in both directions increases slightly until $5\times10^6$ cycles followed by a slight decrease. After $10^7$ fatigue load cycles, dislocation density in both directions increases again. In transverse direction, this tendency is more pronounced.

In VHCF, plastic deformation is scarce and is distributed inhomogeneously. The formation of dislocation is not as pronounced as in HCF, which is why the dislocation density in the material varies slightly. However, as outlined in the first section, a large volume fraction of austenite grains yield due to the low yield stress and preferred crystallographic orientations. Dislocations can however annihilate during the back and forth glide, cross slip and interaction (with each other) processes. At the same time, new dislocations can be generated from Frank-Read sources. The two factors lead to an increase or decrease in dislocation density. Under repeated loading, free dislocations in the out layer of the bulk material glide to the surface, leading to dislocation annihilation associated with the formation of slip markings. In this case, a decrease in dislocation density is observed (Fig. 4.2.10), which in turn reduces the micro-hardness of austenite, as shown in Fig. 4.2.8. As long as the dislocations are hindered by phase boundaries, cyclic hardening of austenite occurs which leads to a multiplication of dislocations. At this stage, an increase in dislocation density in austenite is observed. Hardness measurements performed in this period trend towards higher values. Further repeated loading cycles lead to significant amounts of dislocation pile-ups, increasing the internal stresses between the two phases and promoting the dislocation motion in the adjacent ferrite grain. If plasticity transmission (cyclic softening) takes place, a decrease in both dislocation density and micro-hardness of austenite is again observed. A similar explanation can be found in [99] where a solute annealed (SA) and a cold worked (CW) 316L steel in VHCF were tested. In the case of SA, the universal hardness increases as a function of the number of cycles and cyclic hardening was recognised. In contrast, the hardness of the 10% CW decreases when cycle numbers <$10^6$, explained by cyclic softening. Afterwards, the micro-hardness increases, indicating that cyclic hardening occurs. In the case of 20% CW, the transition stage lies at $10^7$ cycles. The cyclic hardening and cyclic softening were interpreted to be caused by dislocation densities. The development of micro-hardness and its interpretation are shown in detail in Fig. 4.2.11.

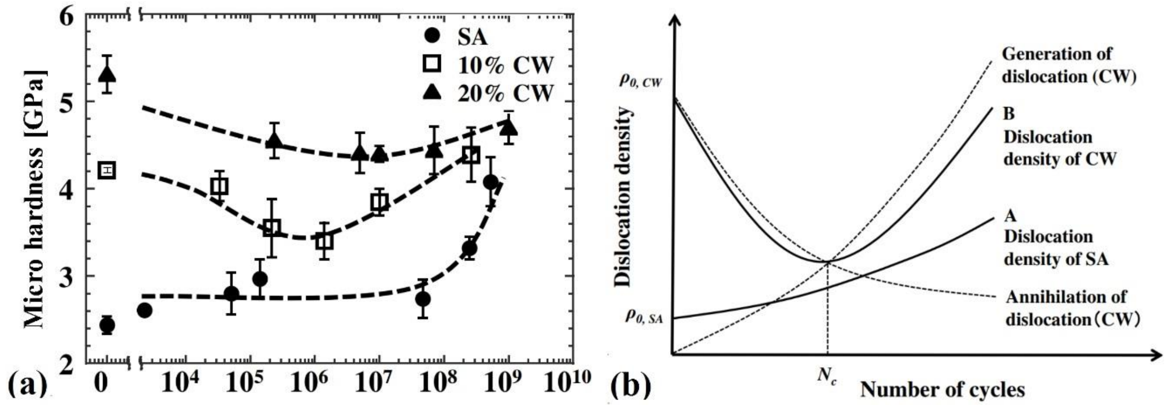

**Fig. 4.2.11:** a) Relationship between micro-hardness and number of cycles and b) schematic diagram of dislocation density development during cyclic loading [99].

The development of dislocation density and micro-hardness in the present study behave in a similar manner as that in the CW conditions in [99]. Considering the specimens studied were quenched in cold water (25 °C) after heat treating at 1050 °C, a moderate dislocation density is expected due to material shrinkage. The quenching process distributes residual stresses across the entire specimen as well. When a specimen is subjected to fatigue loading, repeated loading cycles lead to dislocation gliding. On the surface of the specimen, as described, dislocations in the form of slip markings emerge, resulting in a decrease in dislocation density and cyclic softening of the austenite. At the phase boundary, dislocation gliding may be blocked, leading to cross slip and multiplication of dislocations. The blocking effect and multiplication process are considered as the main reasons for the cyclic hardening of austenite in the present study. Experiments carried out at this stage show increasing in dislocation density and micro-hardness.

Dislocation density variation in ferrite is not so pronounced at first, since the applied stress amplitude is less than the yield stress of ferrite. When the cyclic hardening of austenite occurs, dislocation pile-ups at the phase boundary lead to stress concentration which promotes dislocation motion in the adjacent ferrite grain. Peculiarly, when the ferrite grain lies at the surface, crack nuclei are formed by the dislocation gliding, and a decrease in dislocation density is expected. Dislocations that generate from Frank-Read sources lead to an increase in dislocation density.

Dislocation arrangement in VHCF was identified by means of TEM. As expected, dislocations in both phases are observed. Fig. 4.2.12 shows dislocation distribution in both phases of the DSS in the initial state. From the TEM micrographs, the following conclusions can be drawn:

- In austenite, dislocations are visibly aligned in a planar manner. Some zones are enriched with planar dislocation arrangement, while some zones are not as shown in Fig. 4.2.12(a), (c) and (e).
- The ferritic microstructure is characterised by small precipitates dispersed in the matrix. The needle-like precipitates are $Cr_2N$ particles which align along low index crystal planes.
- Fig. 4.2.12(b) and (d) show a relatively higher dislocation density while no dislocation is found in (f). Dislocation segments in (d) exhibit a straight line or bow form.

A similar dislocation characterisation for the same material was presented by Knobbe et al. [100] who claimed that the initial dislocations in both phases are a result of heat treatment, formed in particular during fast cooling by water quenching. No evidence of nitrogen precipitates was found in austenite. This is mainly due to the higher nitrogen solubility in fcc crystal structures exceeding that in bcc structures. Nitrogen in austenite changes the slip character of austenite from wavy to planar.

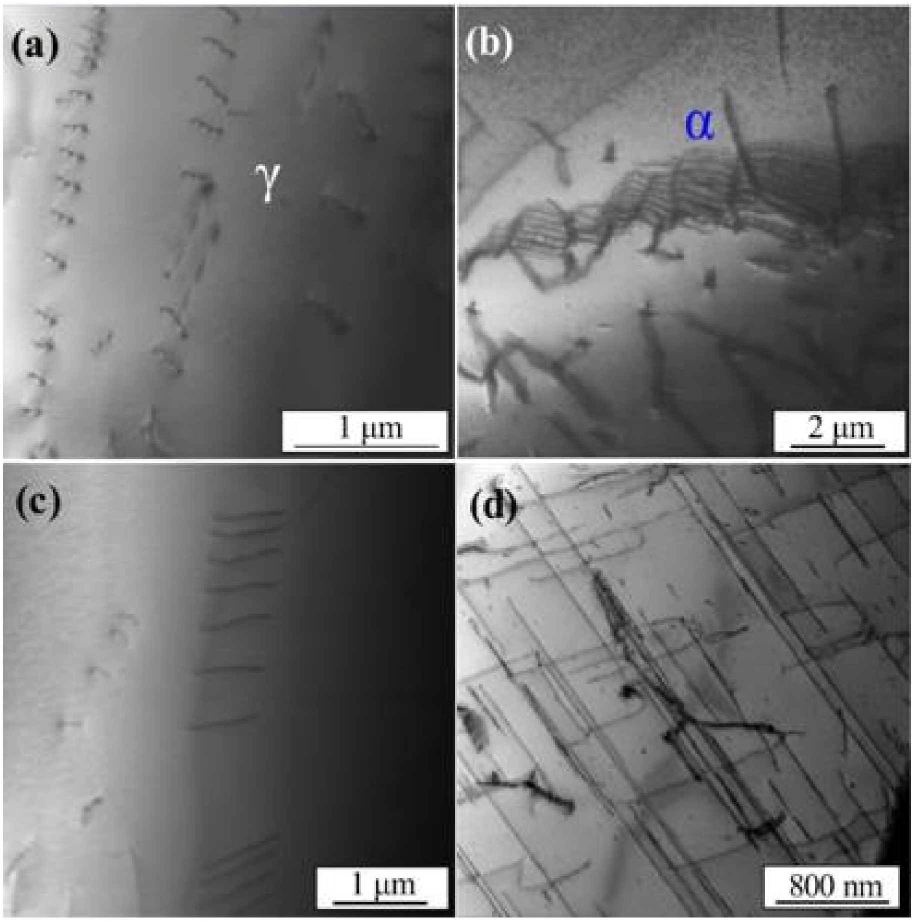

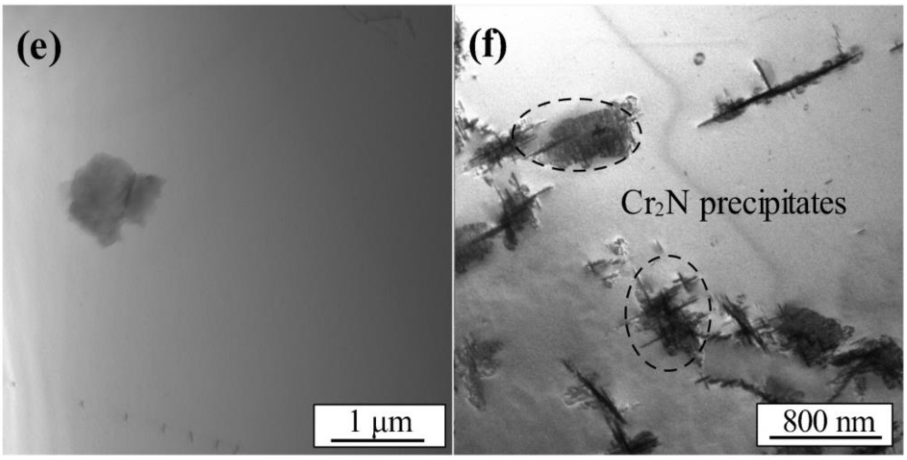

**Fig. 4.2.12:** Dislocation arrangements in the initial state of the DSS: a) and c) are randomly distributed planar dislocation arrangements in austenite, and e) dislocation-poor zone in austenite, b) and d) are zones of high dislocation density in ferrite and f) dislocation-poor zone in ferrite.

Dislocation arrangements after fatigue in the VHCF regime are shown in Fig. 4.2.13 and Fig. 4.2.14. Dislocation pile-ups are the main characteristics of the austenite in VHCF. Such pile-ups against the phase boundary lead to stress concentration and result in dislocation transmission or dislocation generation in the ferrite grain, as shown in Fig. 4.2.14(a) marked with white ellipse and arrow. Some bowed dislocation segments of austenite are observed in Fig. 4.2.13(a) and Fig. 4.2.14(c). Dislocations in ferrite, however, show a higher density which confirms the former calculated dislocation densities in both phases. The type of dislocation structure in ferrite was investigated by Mateo et al. [101], who described that structures consisting of primary dislocations exhibits predominantly screw characteristics, either completely straight or bowed segments with small loops. These microstructural features are confirmed in Fig. 4.2.13(c) and (d), and Fig. 4.2.14(b) and (d).

These TEM images indicate that phase boundaries act as strong barriers for dislocation motion. Stress concentration caused by dislocation pile-ups may lead to crack initiation in the later stage of the fatigue process. On the contrary, twin boundaries in austenite exhibit no blocking effects. Dislocations can transmit the twin boundaries easily, resulting in a release of internal stresses. Hence, no cracks are found in austenite in the regime of VHCF. The ‘no-blocking’ effect is evidenced by the example shown in Fig. 4.2.15.

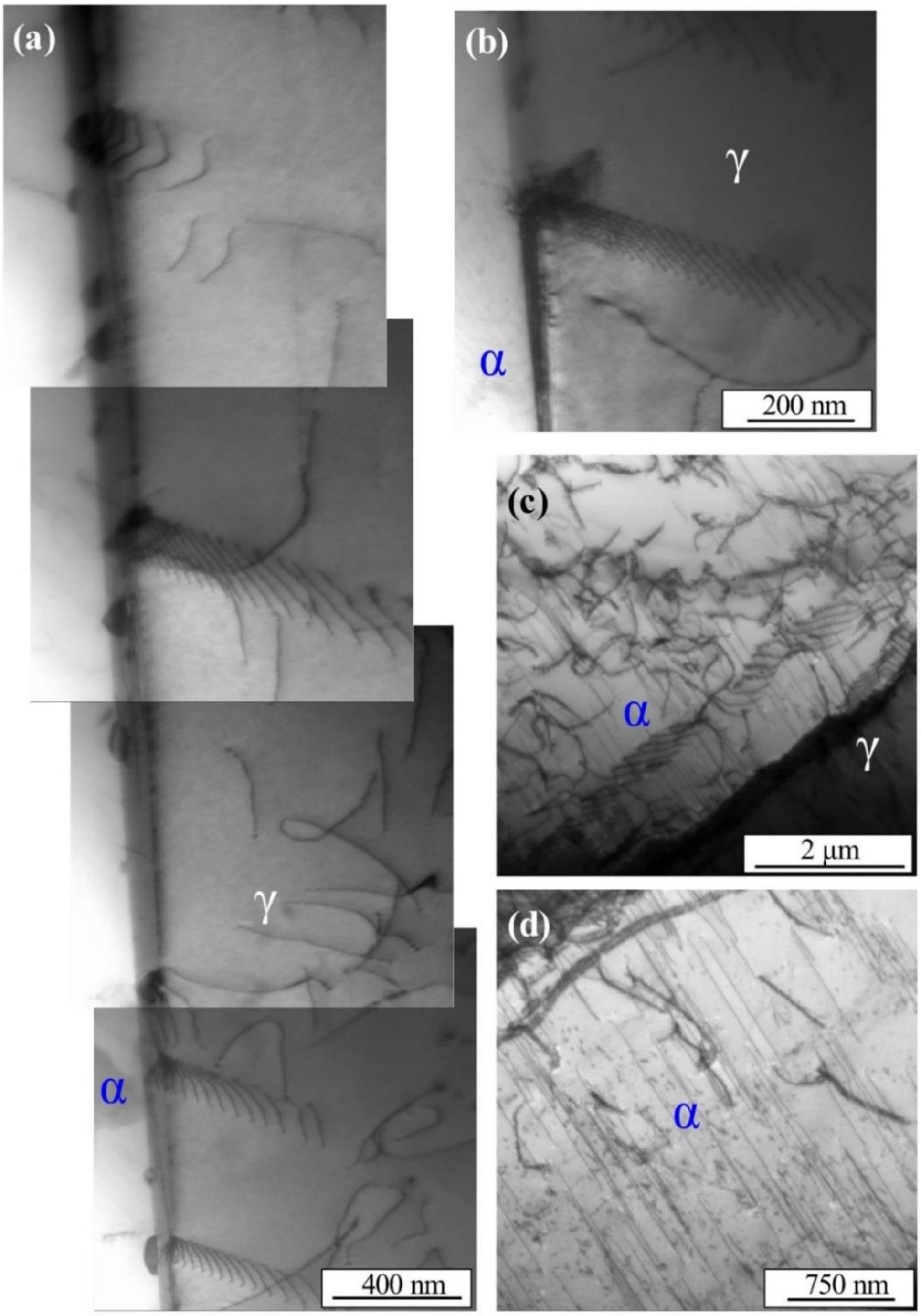

**Fig. 4.2.13:** Dislocation arrangements in a fatigued sample of the DSS ($\Delta\sigma/2=345$ MPa, $N=5\times10^8$): a) and b) are dislocation pile-ups and randomly distributed dislocations in austenite, while c) and d) higher dislocation density in the plastic deformation zone of ferrite.

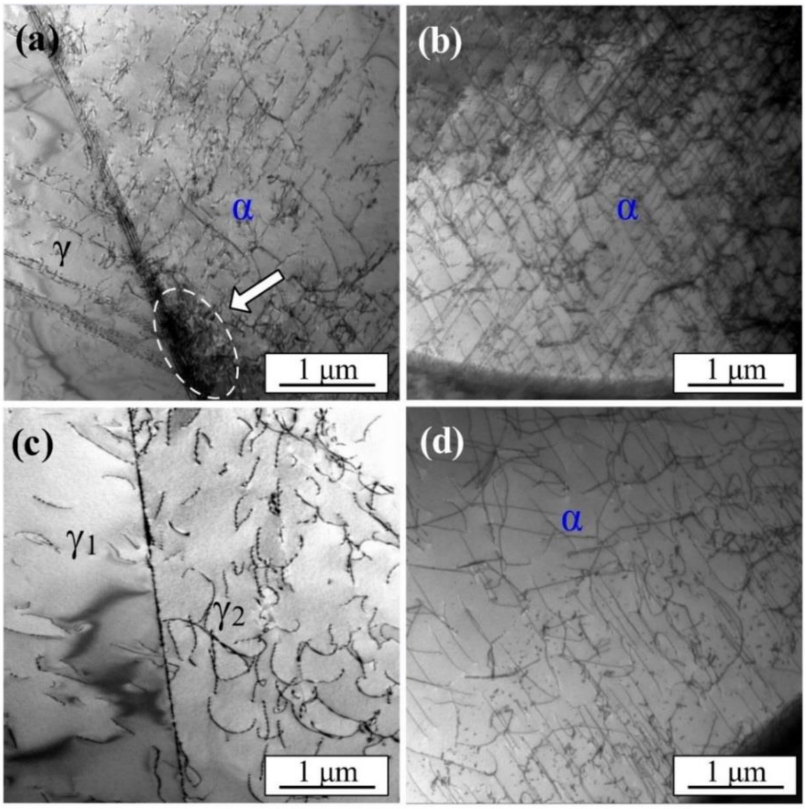

**Fig. 4.2.14:** Dislocation arrangements in a fatigued sample of the DSS ($\Delta\sigma/2$=345 MPa, N=5×$10^9$): a) shows dislocation pile-ups in austenite and dislocation transmission or dislocation generation in ferrite due to stress concentration caused by dislocation pile-ups (marked by white ellipse), c) is randomly distributed bowed dislocation segments and b) and d) show higher dislocation density in the plastic deformation zone of ferrite.

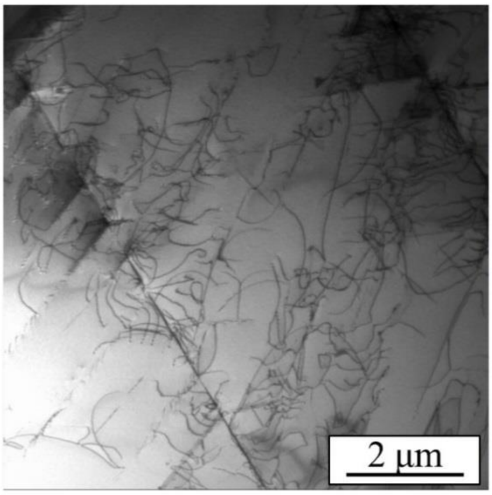

**Fig. 4.2.15:** TEM micrograph showing that a twin boundary acts as a weak barrier during fatigue process ($\Delta\sigma/2$=345 MPa, N=5×$10^9$).

### 4.2.4 Observation of micro-cracks

Micro-crack identification of the DSS in VHCF was already performed by Dönges et al. [22] and Krupp et al. [83]. Phenomenological observations show two types of micro-cracks: 1) intergranular cracks caused by massive slip band impingement into the respective grain boundary and 2) transgranular cracks along crystallographic directions or pencil-glide cracking or by alternating operation of slip systems. Both crack initiation mechanisms can be described by the model of Tanaka and Mura [32], and the two types of cracks and related models are presented in Fig. 4.2.16.

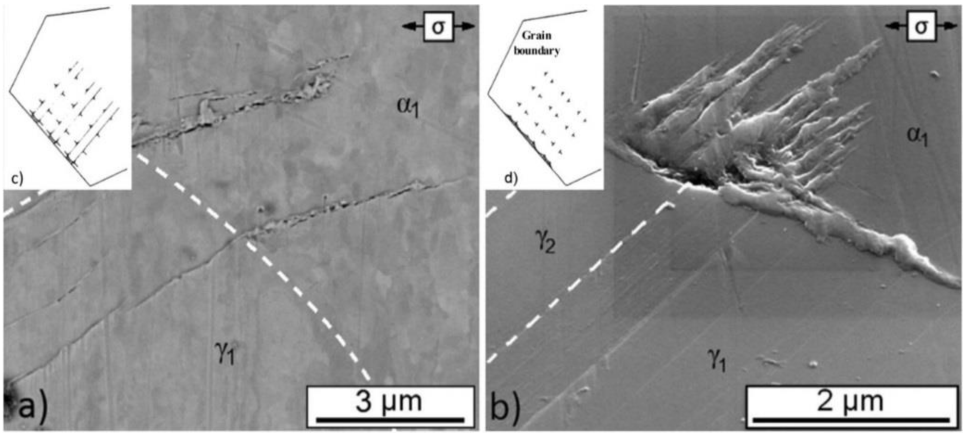

**Fig. 4.2.16:** Representation of the two type micro-cracks presented in VHCF: a) transgranular, b) intergranular and Tanaka-Mura dislocation model (c) and (d) for the two conditions, respectively [22].

Moreover, the critical number of cycles for crack initiation can be quantitatively calculated according to this dislocation model. Micro-cracks are attributed to a local accumulation of dislocation dipoles caused by cyclic irreversible plastic deformation. The dislocation dipoles increase the stored energy stepwise until a critical value is achieved. Crack initiation taking place after a number of load cycles $N_i$ can be calculated from equation 2.4.

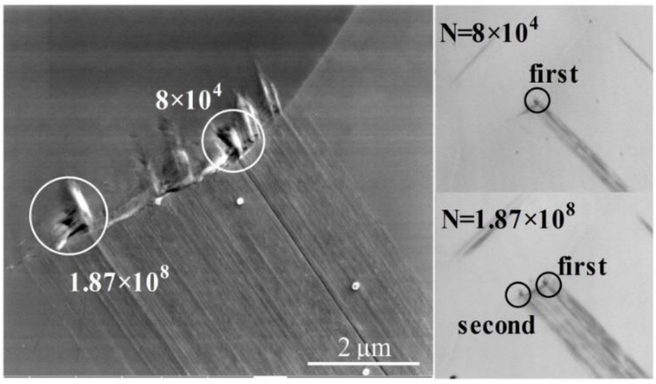

**Fig. 4.2.17:** SEM image showing two crack nuclei (left) and images were taken by confocal laser scanning microscopy at the same position showing the two crack nuclei formed at different load cycles (right).

However, the crack initiation process in VHCF is not straightforward. Fig. 4.2.17 shows that micro-cracking can take place in a very early stage or in a relatively late stage. The first crack nucleus forms at about $8\times10^4$ cycles while the second one initiates after about $1.87\times10^8$ cycles. The two micro-crack nuclei exhibit different plastic deformation extent as well. The reasons for these experimental findings of the DSS in VHCF, however, are not yet clear.

For the same specimen, besides the two small transgranular micro-crack nuclei, an intergranular micro-crack beneath the surface is observed. The crack is detected by means of FIB-cutting and the FIB slices are shown in Fig. 4.2.18. The micro-crack is about 100 nm deep and 1.2 µm long, and situated along a phase boundary. A plastic deformation zone, located in the austenite and formed by dislocation arrangement, is also discovered. Interestingly, a 'squeezed zone' on the surface of the ferrite is identified. Unlike the extrusion, this zone has only partial plastic deformation of the slip plane. On the edge of the 'squeezed zone' (left side), more plastic deformation is present. It seems that a force lying at an angle to the surface pushes this part out of the matrix. The mechanism of this 'squeezed zone' will be discussed in section 4.5.

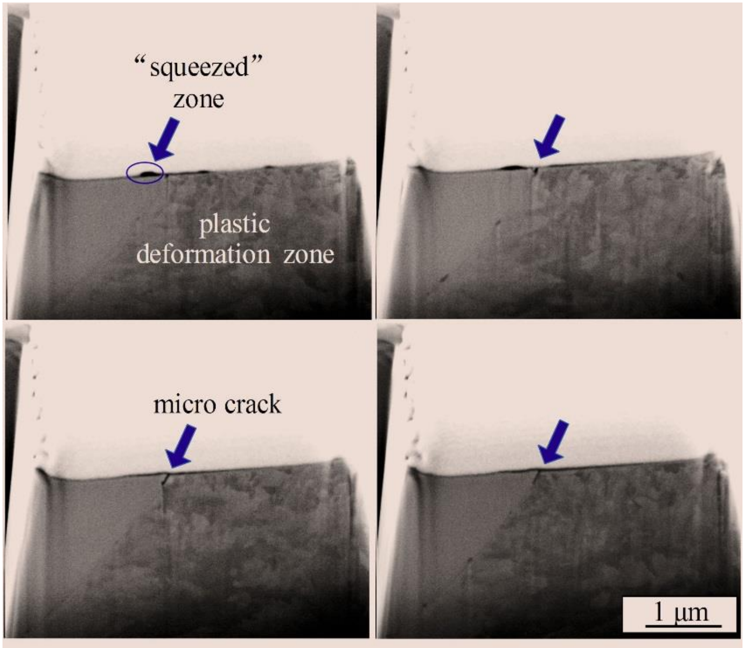

**Fig. 4.2.18:** FIB slices showing the micro-crack along the phase boundary beneath the surface.

Experimental observations illustrate that not all of the activated austenite grains (grains showing slip markings) can induce plastic deformation in the adjacent ferrite grains. Slip markings in austenite can be completely restricted by a phase boundary. One example can be seen in Fig. 4.2.19(b). After $2\times10^7$ fatigue cycles, no plastic deformation is created in ferrite. Conversely, at another site of the same specimen, Fig. 4.2.19(a), a micro-crack is discovered after 6000 fatigue load cycles, indicating that formation of micro-cracks is not solely dependent on fatigue load cycle number.

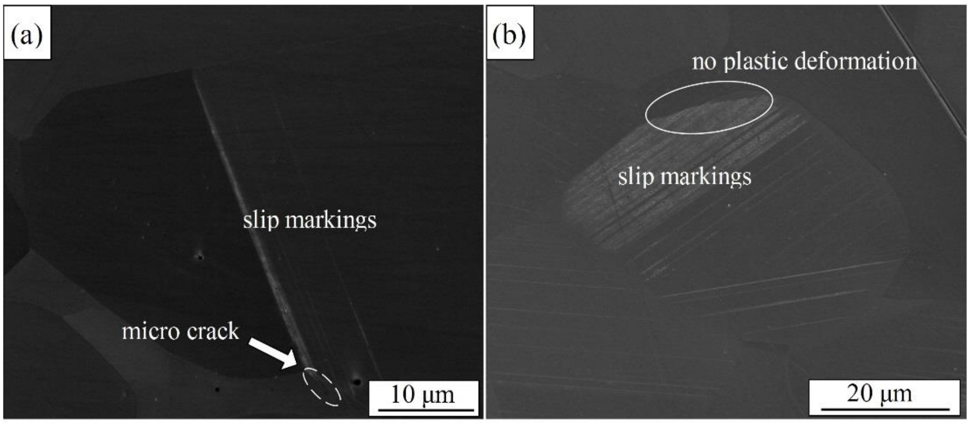

**Fig. 4.2.19:** Two different sites of the specimen showing a) a micro-crack after 6000 cycles and b) no plastic deformation after $2\times10^7$ cycles.

The diverse phenomena of the micro-cracks reveal that different crack initiation mechanisms are concealed. This leads to the main objective of this thesis: the original crack initiation of the DSS 1.4462 in VHCF. In section 4.5, a new crack initiation concept will be proposed and discussed, based on the experimental findings.

## 4.3 In-situ stress distribution

The observed crack initiation sites are normally expected to be stress raisers where inhomogeneity of the microstructures, such as sharp corners, is usually present. This can be confirmed by FEM simulations [102]. Experimental confirmations, however, are more complicated, especially when the material contains two phases with different elastic and plastic properties. The inhomogeneity of the two phases unevenly distributes the applied stress [103]. Accordingly, cracks initiate at microstructural stress raisers. Thus, understanding the interactions between the applied load and the microstructure is necessary for the DSS studied. In the observed cyclic hardening and cyclic softening stages in particular, the interactions are becoming much more interesting. In this section, stress partitioning obtained by in-situ XRD will be presented and discussed.

In order to monitor the stress distribution of the DSS in-situ during tensile loading, a small push-pull rig was placed in the Euler cradle of the laboratory XRD setup. Much effort has been spent to modify and align the rig to ensure that the measured specimen was in the exact centre of the cradle. Subsequently, the specimen was loaded to a strain of 0.17% step by step, during which the applied stress in both phases was measured by means of XRD. The measuring principle has already been described in the experimental section. Stress measurements were executed by using CrKα radiation and extended up to $-50° \leq \psi \leq 50°$ for the ferritic phase and $-42° \leq \psi \leq 42°$ for the austenitic phase based on the $\sin^2\psi$ method. The (211)-plane was selected for the ferrite phase and the (220)-plane was selected for the austenite phase as they both have an anisotropic orientation factor close to the isotropic value. The additional reason is that they both have relative high $2\theta$ angles, which minimise the instrumental error. With considerable interruptions during loading, a stress-strain curve was achieved. After that, the specimen was fatigued to different load cycles (in the cyclic hardening and cyclic softening stages) and the same measurements were repeatedly performed. The load sharing of the external load and its related development were afterwards calculated according to equation 2.16. More experimental details can be found in [67]. The load sharing experiments were carried out at fatigue load cycles of N=1, $10^7$, $10^8$ and $5.8\times10^8$.

Fig. 4.3.1 illustrates the measured stress-strain curves at different fatigue load cycles, where the black, red and blue lines represent the measured stress in austenite, ferrite and the macro stress as a function of applied strain (measured by strain gauge), respectively.

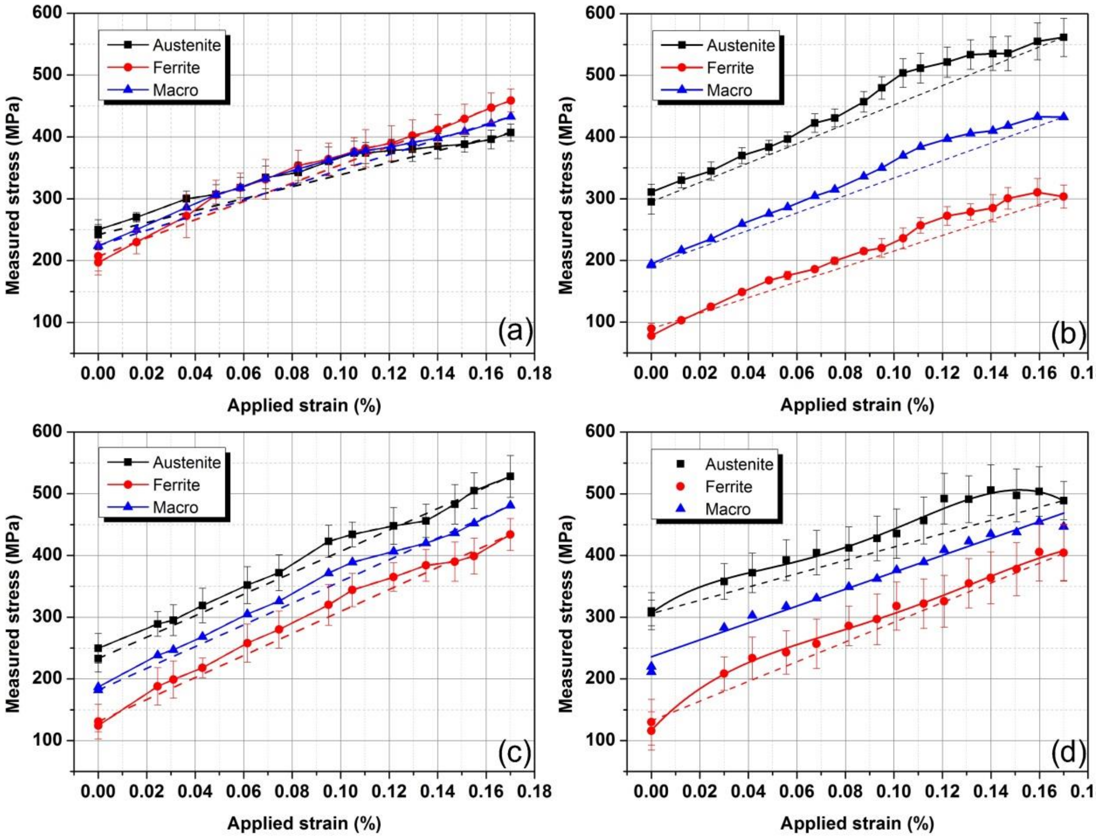

**Fig. 4.3.1:** Stress-strain curves obtained by in-situ XRD, showing the load distribution in the two phases after fatigue loading with a) N=1, b) N=$10^7$, c) N=$10^8$ and d) N=$5.8\times10^8$ cycles.

In-situ stress distribution after the first load cycle, as depicted in Fig. 4.3.1(a), reveals that both phases carry nearly an identical stress value up to an applied strain of 0.105%. Further tensile load appears to give a stress partitioning between the two phases, where the measured stress in the austenitic phase stays stable, while the stress in the ferritic phase increases. The unchanged stress in austenite (in the strain range of 0.105–0.13%) indicates that micro yielding occurs. This is in agreement with Düber's work [94] which pointed out that the external load, necessary for the austenitic phase of the same DSS to yield, lies between 200–250 MPa, as compared 207 MPa (the applied stress at the strain of 0.105%, i.e., $\sigma=197\times0.105\%\times1000=207$ MPa) in this study. The behaviour of the ferritic phase, however, remains elastic, so that a continuous increase in the measured stress is observed. The yield stress for ferrite is not shown in Fig. 4.3.1(a). According to Düber [94], it lies between 500–600 MPa. After yielding of the austenitic phase, load transfer takes place from the austenitic phase to the ferritic phase due to the different elastic-plastic properties. In this area, the more external load is carried by the ferritic phase, while the austenitic phase carries less. Moreover, the internal stresses (the difference between the macro stress and the phase stress) redistribute, i.e., the initial negative micro stress in the ferritic phase becomes positive, and the positive micro stress in the austenitic phase becomes negative. After unloading, a redistribution of the residual stresses is observed due to the micro yielding of the austenitic phase. With increasing of the number of the load cycles, an accumulation of the residual stresses is expected. At a fatigue load cycle of $N=10^7$, as shown in Fig. 4.3.1(b), the total residual stress in austenite becomes greater, being approximately 300 MPa as compared to the initial state of 250 MPa. The variation is more appreciable in ferrite, which drops from 197 MPa to 79 MPa. The difference of the residual stress between the two phases becomes larger, which agrees with the synchrotron radiation XRD results that the internal residual stresses increase after the very early fatigue load cycles. The micro yield stress of the austenite, however, seems to become higher at 0.13% of load strain, corresponding to 256 MPa of applied stress ($\sigma=197\times0.13\%\times1000=256$MPa, the micro yield point is approximately at the strain of 0.13%), indicating that cyclic hardening takes place. At a fatigue load cycle of $N=10^8$, no obvious micro yielding is observed and thus no load transfer occurs, as shown in Fig. 4.3.1(c). At a fatigue load cycle of $N=5.8\times10^8$, micro yielding of the austenitic phase is observed again taking place in the strain range of 0.13–0.16%; the ferritic phase, however, remains elastic.

In order to better demonstrate the load partitioning effect, the load sharing index $L_\gamma$ is plotted against the number of cycles according to equation 2.16. The results are depicted in Fig. 4.3.2. As illustrated in Fig. 4.3.2, the initial load sharing index is 0.39 which indicates that more applied stress is carried by ferrite. At a fatigue load cycle of $N=10^7$, a load sharing index $L_\gamma=0.527$ is achieved, meaning load transfer occurs, i.e., more applied stress is carried by austenite. As outlined in section 4.2, the DSS exhibits austenite-like behaviour, showing two transitions of cyclic softening and cyclic hardening. The occurrence of cyclic softening or hardening changes the external load partitioning in dual-phase materials [67]. The relatively harder phase carries more applied stress. Knowing that the austenite becomes harder in the cyclic hardening regime, the change of the load sharing index agrees well with Johansson’s work [67]. The influence of the initial cyclic softening of the austenitic phase on the load sharing index is not observed here due to the limited experimental data.

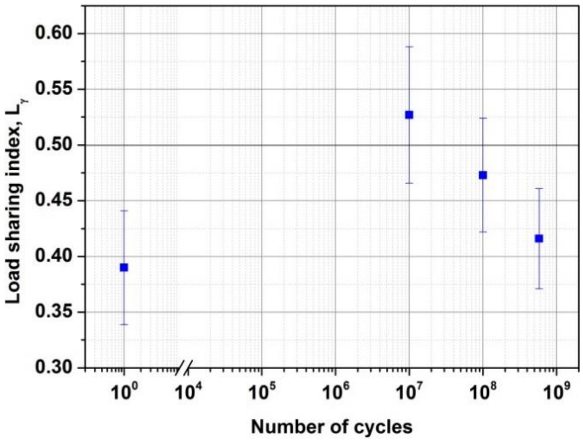

**Fig. 4.3.2:** Load sharing index of the austenitic phase as a function of load cycles.

It is noteworthy that even though cyclic hardening occurs, the micro-hardness of austenite is still lower than in the initial state (shown in Fig. 4.2.8 by means of nanoindentation tests). This should lead to a lower load sharing index. The higher load sharing index shown here is mainly attributed to the redistribution of the micro residual stresses from equation 2.16. The initial micro residual stress in austenite is about 40 MPa, but after $10^7$ load cycles, the micro residual stress is approximately 120 MPa.

When plasticity such as dislocation transmission or even small crack initiation proceeds to the ferritic phase, local internal residual stresses release (cyclic softening) and a decrease in the load sharing index is obtained.

The description above indicates that micro residual stresses strongly influence the load sharing index. The influence of the load sharing index on crack initiation will be discussed in section 4.5 in combination with other experimental findings.

## 4.4 Strain mapping and strain localisation

It is well known that plastic deformation in VHCF is restricted to several grains. Load sharing measured by in-situ XRD in the former section actually represents the measured area which is about 1 mm × 1 mm. To observe the local plastic flow and crack initiation in one single grain or a few grains, high resolution methods are greatly desired.

DIC method that utilises optical imaging or SEM imaging is readily available for measuring local plastic deformation. Experiments carried out by this method provide insight into mechanisms of crack initiation of materials. In this section, results from in-situ DIC experiments in terms of residual strain obtained after cyclic loading and in-situ strain partitioning during tensile loading between the two phases are demonstrated.

The patterning process of DIC can be performed with nanoparticles, chemical vapour thin film rearrangement and lithography methods. The speckle pattern applied on the surface should be anisotropic, of high contrast and randomly distributed. As pointed out by Kammers and Daly [104], the speckle size should cover approximately 3 pixels × 3 pixels and each subset should contain 3 speckles × 3 speckles. The technique employed in this investigation was FIB-etching by loading a 24 bitmap pattern produced by Matlab.

The in-situ DIC experimental details are as follows: a flat specimen was firstly fatigued for 6000 cycles at a stress amplitude of 300 MPa. Subsequently, a careful investigation was made on the surface to detect spots where slip markings or micro-crack nuclei are present. A noteworthy area was then selected and covered with the pattern created by means of FIB. The microstructure of this area and the pattern are illustrated in Fig. 4.4.1(a) and (d); a larger magnification is shown in Fig. 4.4.1(b). Additionally, in order to distinguish the two phases, EBSD was carried out and the result of phase mapping is illustrated in Fig. 4.4.1(c).

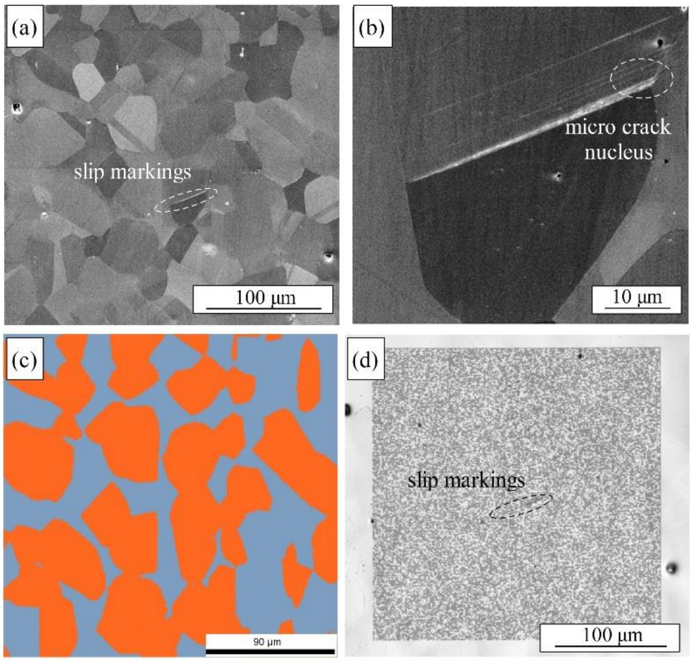

**Fig. 4.4.1:** a) Microstructure of the area in question, b) larger magnification of a), c) phase mapping by EBSD and d) optical image of the pattern applied on the surface of the specimen.

The specimen was loaded step-wise to a strain of 0.15%. Images were recorded by means of confocal laser microscopy in order to observe the in-situ strain partitioning of the two phases. Afterwards, the specimen was unloaded and fatigued to different load cycle numbers of $N=4.5\times10^5$, $N=5.2\times10^6$, $N=6.2\times10^6$ and $N=1.2\times10^7$. In-situ tensile experiments were repeatedly performed. Moreover, by comparing the pattern without the external load at different load cycles, the residual strain in this region was obtained. Results of the residual strain and the in-situ strain mapping are shown below.

### 4.4.1 Mapping of residual strains

Strain mapping for each grain was achieved by the following method. The grain/phase boundaries of the microstructure were firstly acquired by EBSD and then overlapped with the strain mapping obtained by DIC electronically. The residual strain distribution in the individual grains is illustrated clearly in the overlapped images, as shown in Fig. 4.4.2. The strain component $\varepsilon_x$ and von Mises $\varepsilon_{VM}$ were selected in this case. The stain component $\varepsilon_x$ gives the strain variations in the transverse direction perpendicular to the loading axis, reflecting the interactions between austenite and ferrite grains. The von Mises $\varepsilon_{VM}$ strain exhibits pronounced variations at such sites.

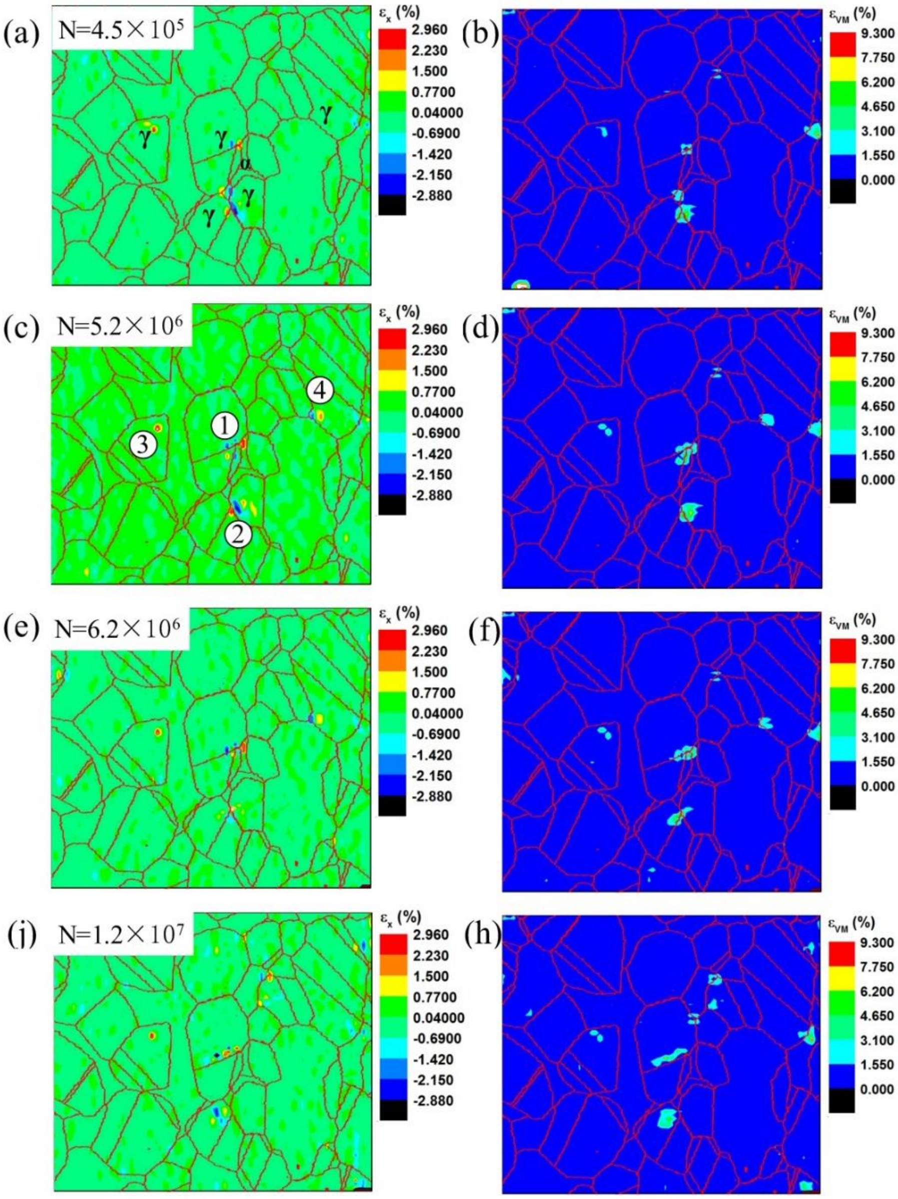

**Fig. 4.4.2:** DIC images showing residual strain distribution of the specimen at different cycle numbers. (a), (c), (e) and (j) present the strain component $\varepsilon_x$ and (b), (d), (f) and (h) give the von Mises strain $\varepsilon_{VM}$. The loading direction is vertical.

Fig. 4.4.2 illustrates the residual strain distribution of the measured area after different cycle numbers. It is interesting to note that at the site where slip markings exist and a micro-crack nucleus is found (position 1 in Fig. 4.4.2(c)), significant variations in the strain component $\varepsilon_x$ are present. The austenite grain with slip markings carries a compressive residual strain $\varepsilon_x$ while the adjacent ferrite grain exhibits a tensile residual strain $\varepsilon_x$. Taking the residual stress distribution measured by synchrotron radiation and laboratory XRD into account, the variation of residual strain can be interpreted as a relaxation of residual stresses. Initial repeated loading leads to dislocation pile-ups at the phase boundary, inducing tensile micro residual stress in austenite and compressive stress in ferrite. If, however, the dislocation pile-ups cause plasticity transmission to the adjacent ferrite grain, the residual stresses will be released. Therefore, a decrease in the strain component $\varepsilon_x$ in austenite is observed. This damage accumulates until a fatigue load cycle number of $6.2\times10^6$. Further fatigue loading leads to a relaxation of the residual strain (at site 1) which can likely be attributed to the newly generated dislocation-ups, producing tensile residual stress in austenite and compressive residual stress in ferrite, at the phase boundary again.

The intergranular residual strain between the austenite-austenite grains can be observed at site 2. The strain between the two grains accumulates until a fatigue load cycle of $5.2\times10^6$, and further fatigue loading appears to minimise the residual strain. Residual strain at the sites of 3 and 4, on the sharp corner of a single grain, is likely due to the stress concentration during loading and the incompatibility with the surroundings during unloading. Damage accumulations on these sites are much more pronounced for von Mises strains, as illustrated in Fig. 4.4.2(b), (d), (f) and (h).

### 4.4.2 In-situ strain variation

Fig. 4.4.3 shows the strain distribution of the two phases at a tensile strain of 0.15% (strain gauge) at different fatigue load cycles. The machine and artificial errors lead to strain scattering for all three cases. The average strains of the measured area are 0.149%, 0.146% and 0.14% (measured by DIC) at fatigue load cycle numbers of N=6000, $N=5.2\times10^6$ and $N=1.2\times10^7$, respectively. As the in-situ strain component $\varepsilon_y$ (parallel to the loading axis) is more pronounced and interesting, the strain distributions of $\varepsilon_y$ are illustrated in Fig. 4.4.3(a), (c) and (e). To better illustrate the localised strain, in-situ von Mises strains are presented in Fig. 4.4.3(b), (d) and (f). At a fatigue load cycle of N=6000, two local strain intensification sites (marked as 1 and 2 in Fig. 4.4.3 (b)) are observed. The strain concentration at the two sites is likely due to microstructure incompatibility. With increasing numbers of load cycles, the occurrence of plasticity transmission in terms of dislocation transmission or crack can ease these intensifications. Relatively homogeneous strain distributions at fatigue load cycles of $N=5.2\times10^6$ and $N=1.2\times10^7$ are observed, which is actually in good agreement with former investigations. After cyclic hardening-softening transitions, the two phases exhibit similar micro-hardness and carry almost the same amount of stress, meaning the material transforms from an inhomogeneous state to a homogeneous state to adapt to the external load.

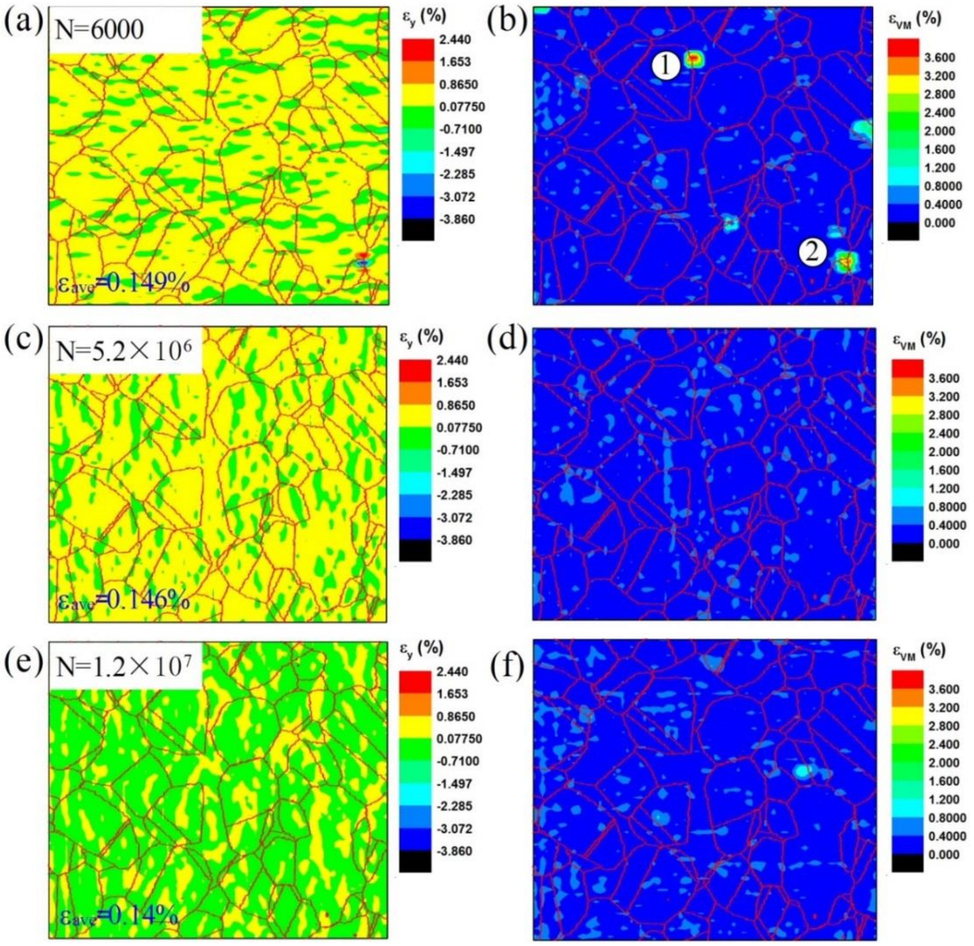

**Fig. 4.4.3:** DIC images showing strain distribution at a tensile strain of 0.15% (strain gauge). a), c) and e) show the strain component $\varepsilon_y$ and b), d) and f) show the von Mises strain $\varepsilon_{VM}$. The loading direction is vertical.

In order to better show the strain partitioning between the two phases at 0.15% tensile strain, the 6080 strain units of the strain component $\varepsilon_y$ were statistically analysed. Distribution of the strain units is plotted in Fig. 4.4.4. At an initial fatigue load cycle number of N=6000, a high portion of the load strain is carried by austenite, while ferrite carries relatively less load strain. As described, this behaviour may be attributed to the inhomogeneity with respect to the microstructure, different elastic-plastic behaviour and different residual stresses of the two phases in the initial state. During loading, the two phases carry different load strains to counterbalance the inhomogeneity. At the fatigue load cycle numbers of N=$5.2\times10^6$ and N=$1.2\times10^7$, an almost equivalent amount of load strain is taken by the two phases. This can be attributed to the elimination of the inhomogeneity during the cyclic hardening and cyclic softening processes.

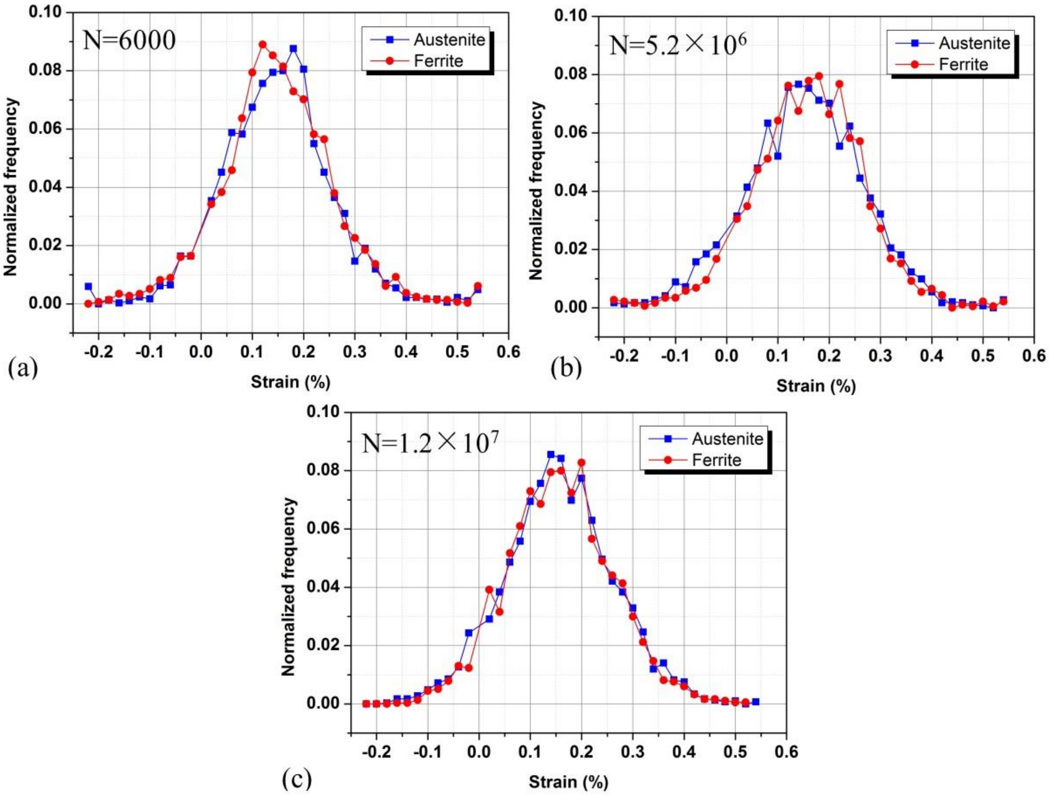

**Fig. 4.4.4:** Distribution of the strain units of the component $\varepsilon_y$ at the tensile strain of 0.15% at different number of cycles.

The in-situ strain partitioning of the two phases during the whole tensile tests is plotted quantitatively in Fig. 4.4.5 where the black, red and blue lines represent the strain in austenite, ferrite and the average strain of the measured area, respectively. X and Y axes correspond to the strain measured by strain gauge and DIC, respectively.

Again, the strain partitioning between the two phases is observable at a fatigue load cycle of N=6000. At an applied strain of 0.09%, the partitioning effect becomes considerably larger. This can be ascribed to the micro yield of austenite, leading to an obvious partitioning of the external load. The same phenomenon was also observed by the in-situ stress partitioning which was determined by means of XRD. The partitioning stays almost unchanged until the applied strain reaches 0.15%. It should be noted that the slight variations in strain between the two phases can correspond to significant differences in stress. The Young's modulus of the DSS investigated is approximately 197 GPa. At fatigue load cycle numbers of $N=5.2\times10^6$ and $N=1.2\times10^7$, the two phases carry nearly the same amount of load strain. No obvious strain partitioning is observed.

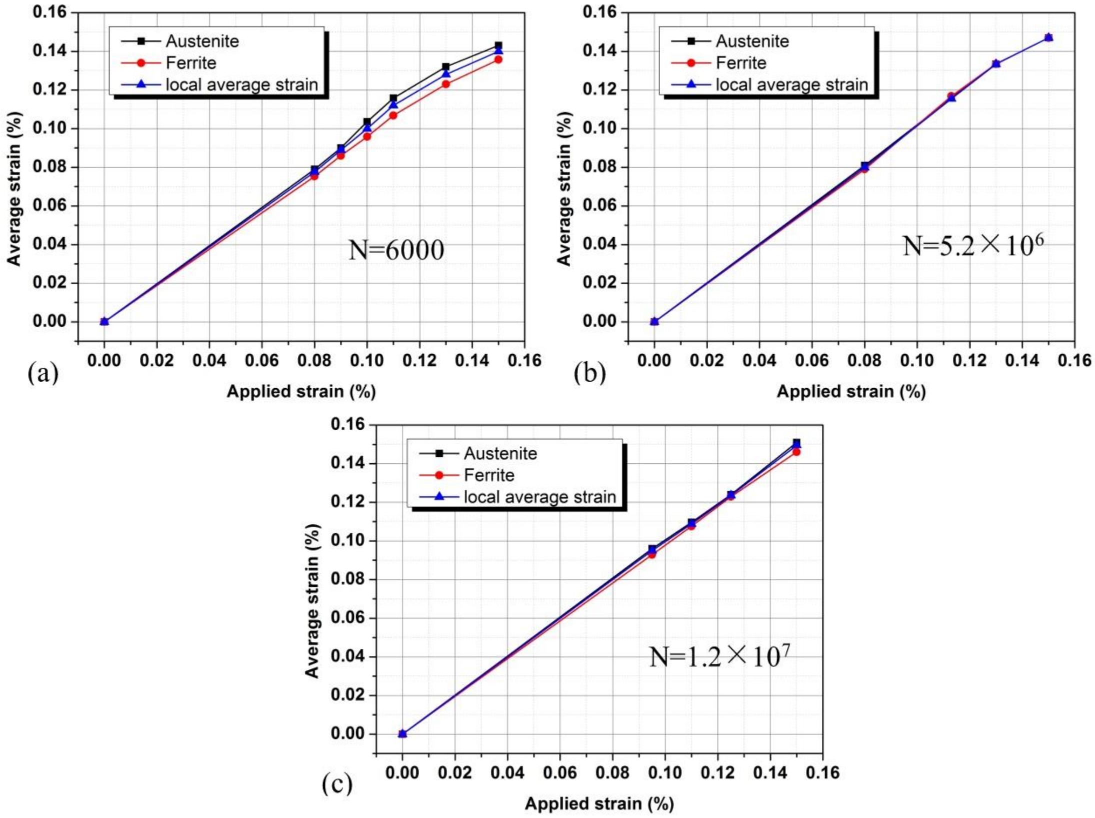

**Fig. 4.4.5:** Strain partitioning of the two phases after different numbers of fatigue load cycles.

## 4.5 Modelling of crack initiation

Although the mechanism of micro-crack initiation in DSS can be explained by the model of Tanaka and Mura [32], some physical observations are still not clearly explained:

- Micro-cracking takes place in ferrite accompanied by strong slip markings in the adjacent austenitic grain, while frequently no plastic deformation can be found under the same circumstance, as shown in Fig. 4.2.19;
- Plastic deformation in ferrite is distinctly extensive (Fig. 4.2.16 and Fig. 4.2.18), forming either intergranular micro-cracks continuously or transgranular micro-cracks suddenly.

These phenomena reveal that micro-crack initiation in VHCF is not straightforward. Therefore, discussions on the mechanisms of micro-crack initiation should be in conjunction with the above-mentioned observations.

### 4.5.1 Intergranular micro-crack

Prasad Reddy et al. [105] proposed that micro-crack transmission into the second grain is attributed to the tip displacement of the crack in the first grain. The active slip direction in the primary grain is roughly perpendicular to the free surface, yielding a fast extrusion growth in the second grain, as shown in Fig. 4.5.1.

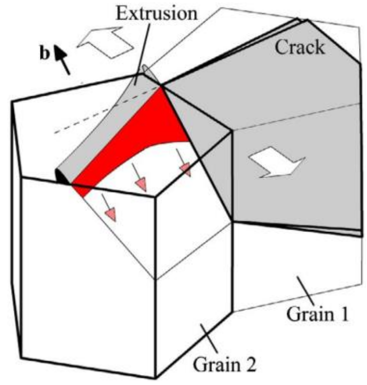

**Fig. 4.5.1:** Micro-crack in grain 2 caused by surface displacement accumulation of grain 1 [105].

Similarly, in VHCF, surface relief in the form of extrusion-intrusion pairs in austenite contributes to micro-cracking in the adjacent ferritic grain. The growth of extrusion-intrusion pairs of the DSS was investigated by Dönges et al. [106] who found that the extrusion-intrusion-height grows dramatically within the first $10^5$ load cycles, as shown in Fig. 4.5.2. The growth height is about 370 nm which inevitably leads to a shear stress in the adjacent ferritic grain.

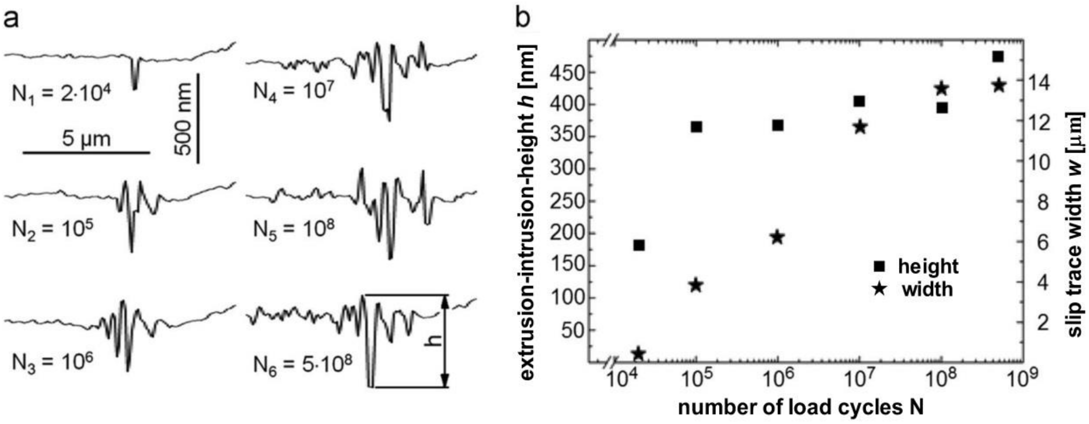

**Fig. 4.5.2:** a) Development of the roughness profile with the number of loading cycles and b) development of the height *h* and the width *w* of an extrusion-intrusion-pair [106].

Dislocation motion and dislocation pile-ups were considered widely by Fivel's group [107-111], and successfully explain various physical phenomena during fatigue processes including such as the formation of PSB, micro-cracks, dislocation density and arrangements and local stress, by means of discrete dislocation dynamics (DDD) simulation. When a slip system of a grain is activated by an external load, dislocations are generated from Frank-Read sources. These dislocation loops slide in planes during repeated loading. When the dislocations are blocked by a grain or phase boundary, dislocation pile-ups emerge in screw or edge types. When the dislocations glide to the surface of the grain, slip markings emerge. A representation of the formation of dislocation pile-ups and slip markings is shown in Fig. 4.5.3.

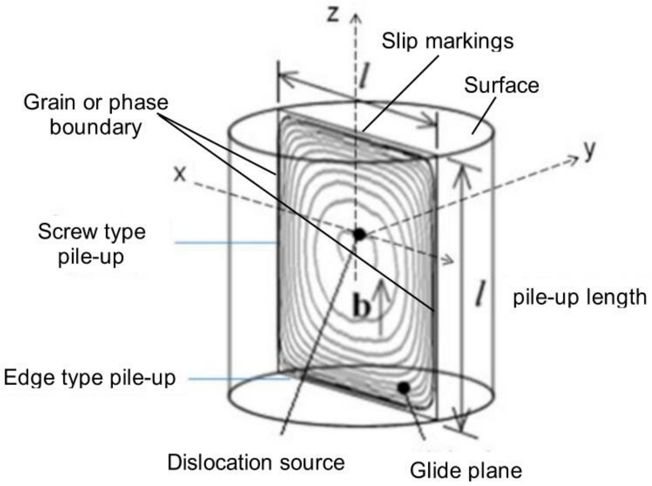

**Fig. 4.5.3:** Representation of the formation of slip markings on the surface and dislocation pile-ups at the grain or phase boundary [107].

According to Tanaka and Mura [32], dislocation pile-ups at the phase boundary results in stress concentration which also contributes to the plastic deformation in the ferritic grain. Additionally, when the specimen is loaded, different slip systems of the ferritic grains carry distinct load stresses, depending on the Schmid factors. It appears that the squeezed zone illustrated in Fig. 4.2.18 can be described as in Fig. 4.5.4:

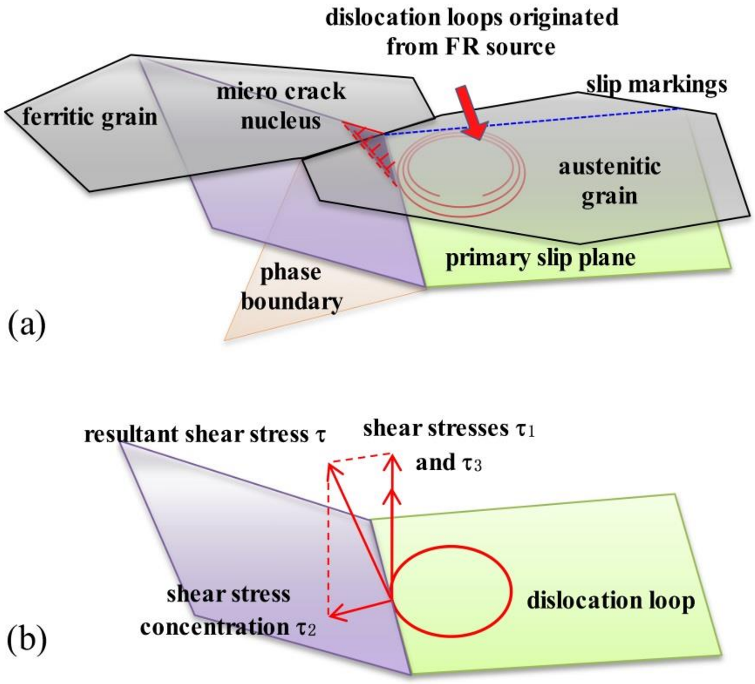

**Fig. 4.5.4:** Schematic figures showing a) micro-crack formation in ferrite and the geometry relationships between two slip systems in austenite and ferrite and b) the resultant force which drives dislocations in the ferritic grain gliding to the surface.

Fig. 4.5.4(a) shows two surface grains, i.e., one is an austenitic grain and the other one is a ferritic grain. When the specimen is subjected to an external load, the austenitic grain is activated. Dislocations originate from a Frank-Read source and glide in the primary slip plane. As described, slip markings and dislocation pile-ups come into being as a result of growing of dislocation loops. At the site where dislocations pile against the phase boundary, three shear stresses can be expected, resulting in micro-cracking in the ferrite grain. The three components are schematically illustrated in Fig. 4.5.4(b) and they are 1) shear stress $\tau_1$ due to the accumulation of intrusion-extrusion-height (slip of dislocations), 2) shear stress $\tau_2$ due to dislocation pile-ups and 3) shear stress $\tau_3$ due to external load stress. The complexity is that the three components vary during cyclic loading. The development of the shear stress $\tau_3$ can be observed from the in-situ stress and in-situ strain partitioning in sections 4.3 and 4.4. When austenite cyclically hardens, a more external load is transferred from ferrite to austenite. Conversely, cyclic softening of austenite leads to an increase in the load stress in ferrite. Stress concentration $\tau_2$ caused by dislocation pile-ups can be released due to plastic deformation or crack, leading to a change of the resultant shear stress both in amplitude and direction. That is why ferrite shows distinct plastic deformation during cyclic fatigue loading. To better show the variation of the resultant shear stress, a schematic drawing is presented in Fig. 4.5.5:

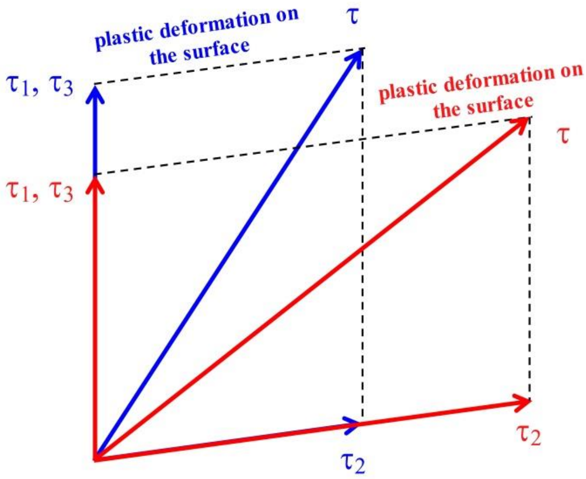

**Fig. 4.5.5:** A representation of the shear stresses showing that the newly formed resultant shear stress (red) leads to a larger plastic deformation on the surface than the initial resultant shear stress (blue).

Hence, the formation of an intergranular micro-crack, as shown in Fig. 4.2.17, can be explained as follows:

- Initially, after a short number of loading cycles, $\tau_1$ increases continuously due to accumulation of displacement caused by intrusions and extrusions. Additionally, dislocation pile-ups lead to stress concentration as $\tau_2$. According to the in-situ XRD results, ferrite carries a high fraction of the external load. The three factors lead to a high resultant shear stress and give rise to initiation of the first micro-crack nucleus in the ferritic grain.

- After the formation of this micro-crack nucleus, stress concentration is released at this site, resulting in a decrease in the resultant shear stress. Hence, no further plastic deformation occurs. However, dislocation multiplication keeps taking place, leading to increasing of slip markings and dislocation pile-ups.
- Subsequently, the accumulation of dislocation pile-ups leads to cyclic hardening of austenite, which causes a stop of slip markings growth.
- At the position where the slip marking stops, dislocations within this slip plane keep moving to the phase boundary and surface slowly. This motion drives an accumulation of the shear stress $\tau_1$ and the shear stress $\tau_2$. When the resultant shear stress reaches the critical resolved shear stress of the adjacent ferritic grain, micro-crack takes place again.
- The plastic deformation zones along the phase boundary coalesce with each other and finally form an intergranular micro-crack. The whole crack formation process is schematically illustrated in Fig. 4.5.6.

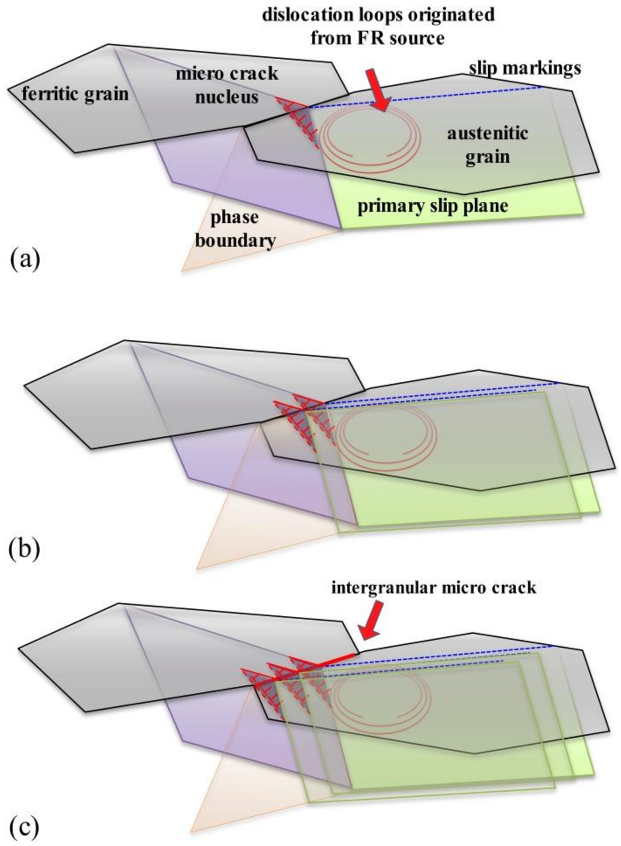

**Fig. 4.5.6:** Schematic figures showing the formation of an intergranular micro-crack along the phase boundary.

### 4.5.2 Transgranular micro-crack

Intergranular micro-cracks can initiate at the very early stage of VHCF life (after thousands of load cycles or earlier) and develop continuously for a long period, as described in the previous section. However, plastic deformation in austenite can frequently be arrested by phase boundary, i.e., no plastic deformation takes place in the adjacent ferrite grain. The barriers remain effective at least up to a number of $10^8$ cycles and hence a technical fatigue limit for the DSS is achieved. Krupp et al. [82] assumed that the arresting may be attributed to the strength of the barriers. The strength of grain boundary is often proposed to increase with an increasing misorientation angle between the neighbouring grains. A tilt grain boundary cannot arrest the dislocations and thus no long-range internal stress field arises. Twist misorientation of the grain boundaries acts as a barrier and block the dislocation transmission. A schematic representation is illustrated in Fig. 4.5.7.

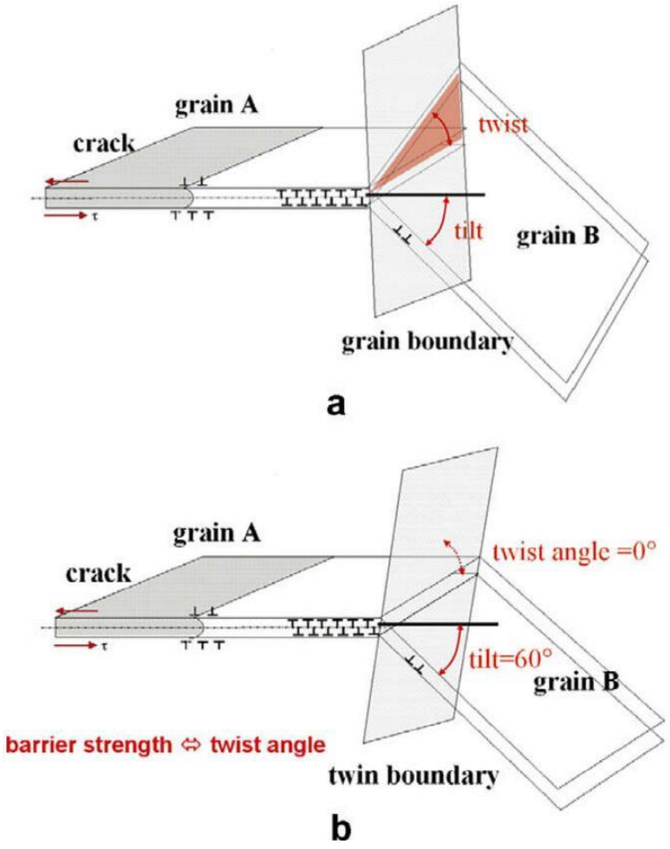

**Fig. 4.5.7:** Schematic representation of slip transmission between two neighbouring grains: a) random high angle grain boundary: the barrier strength is assumed to be proportional to the twist angle and b) twin boundary: the twist angle is equal to 0, correspondingly the barrier strength seems to be low [82].

The same observations of the blocking effect have already been illustrated in Fig. 4.2.2(c) and Fig. 4.2.3(c). After cyclic hardening and cyclic softening transitions, no plastic deformation or cracking is discovered in the ferritic grain. This condition can run for more than $10^8$ cycles and a fatigue limit is expected. However, observations on transgranular micro-cracks, as shown in Fig. 4.5.8 and in Fig. 4.2.16(a), reveal the complexity of crack formation in the DSS.

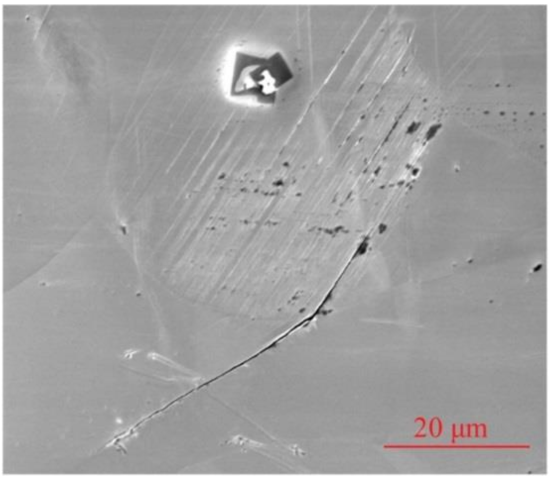

**Fig. 4.5.8:** SEM micrograph showing a transgranular micro-crack in ferrite.

As described in the previous section, the formation of the micro-crack nucleus is dependent on the resultant shear stress. The total shear stress is determined by three components: 1) shear stress $\tau_1$ due to the accumulation of intrusions and extrusions (slip of dislocations), 2) shear stress $\tau_2$ due to dislocation pile-ups and 3) shear stress $\tau_3$ due to external load stress. From a mechanical perspective, the resultant shear stress can vary over a wide range, even if they are constant, depending on the directions of the three components. Considering that the directions of $\tau_1$ and $\tau_3$ are restricted in small angles (in VHCF, only grains with high Schmid factor can be activated), the resultant shear stress is dominated by the direction of the shear stress $\tau_2$ which is directly related to the phase boundary orientations. A schematic drawing is shown in Fig. 4.5.9.

Fig. 4.5.9(a) shows a small plastic deformation zone occurring in ferrite when the angle between the phase boundary and the ferritic surface is less than 90°. As described in section 4.5.1, these small plastic deformation zones coalesce with each other and finally form an intergranular micro-crack. Conversely, when the angle is between 90° and 180°, almost no plastic deformation or transgranular micro-crack formation takes place, depending on the amplitudes of $\tau_1$ and $\tau_3$, as shown in Figs. 4.5.9(b) and (c). It should be noted that even in the first condition (Fig. 4.5.9(a)), there is still a possibility of forming a transgranular crack when the phase boundary lies close to 90°.

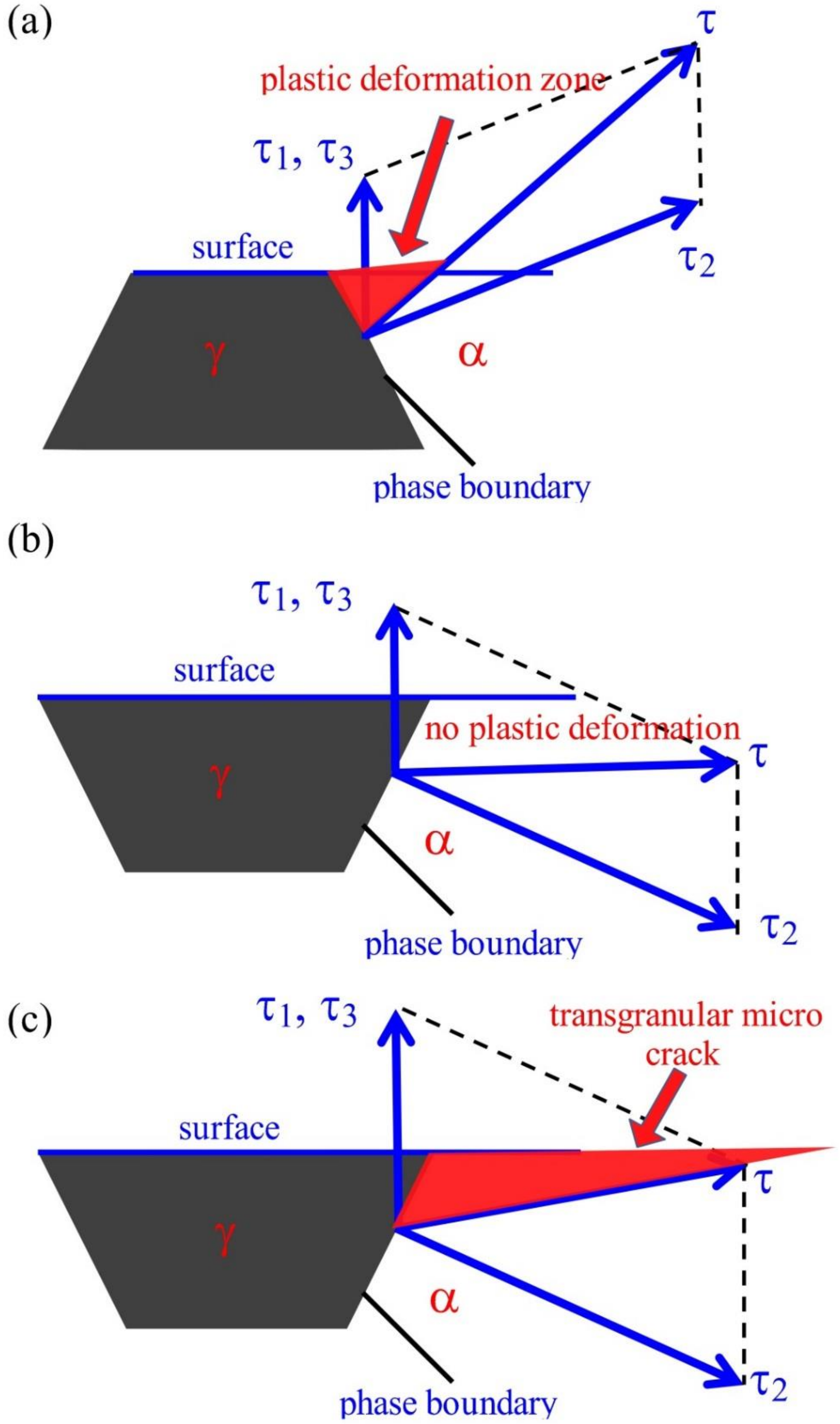

**Fig. 4.5.9:** Schematic figures show a) plastic deformation, b) no plastic deformation and c) transgranular cracking occurring in the adjacent ferritic grain depending on the phase boundary orientations.

In order to verify the description above, the phase boundary orientations were investigated by means of FIB-cutting at six randomly selected positions. The first three positions were selected from the sites where plastic deformation occurs in the ferritic grains. The SEM images are illustrated in Fig. 4.5.10. The last three positions were performed at the sites where no plastic deformation takes place in the ferritic grain. SEM micrographs of these are shown in Fig. 4.5.11.

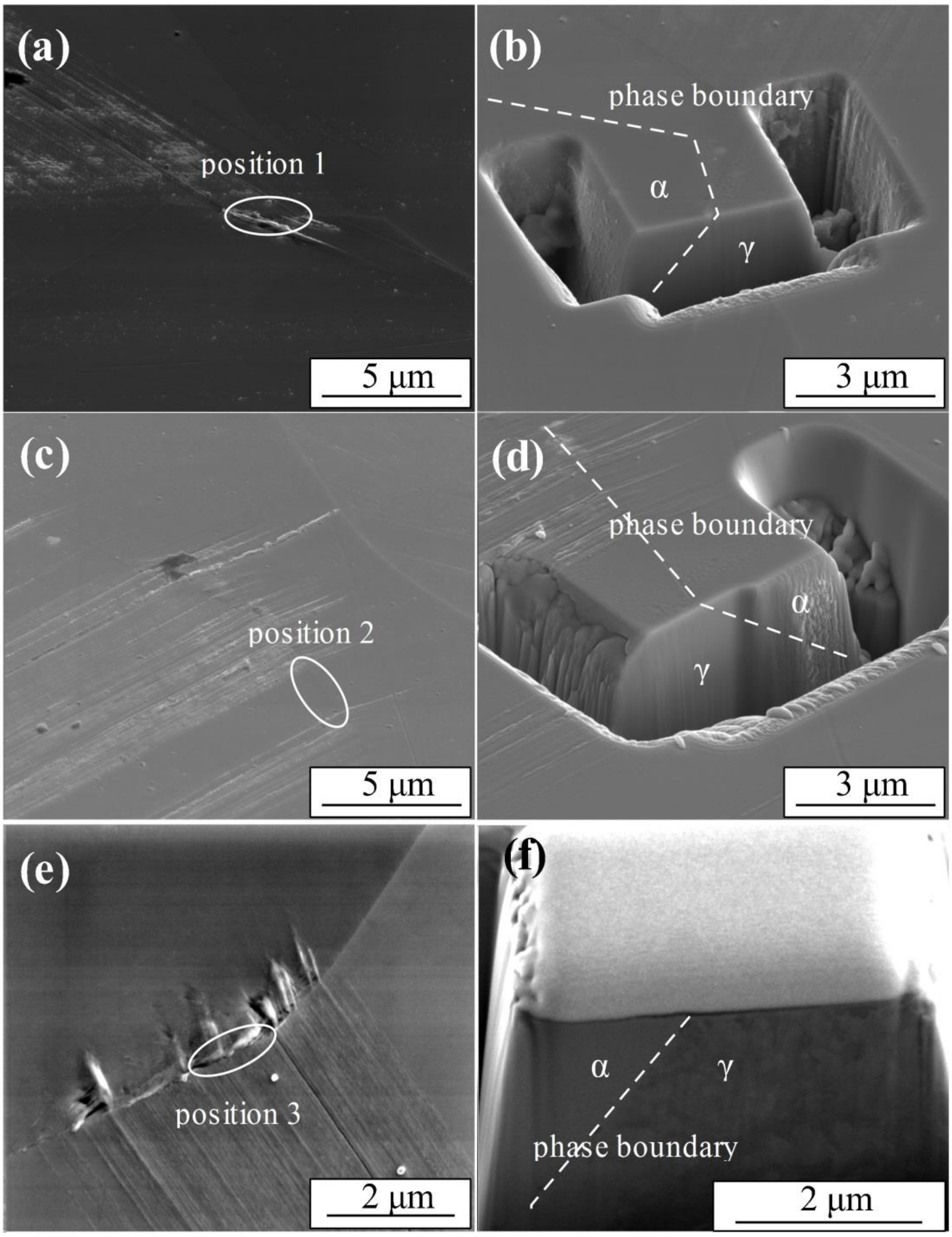

**Fig. 4.5.10:** Phase boundary orientation confirmed by FIB-cutting. (a), (c) and (e) are the selected positions where plastic deformation in both phases was found, while (b), (d) and (f) show the phase boundary orientations. The angles between the phase boundary and the ferritic phase surface are smaller than 90°.

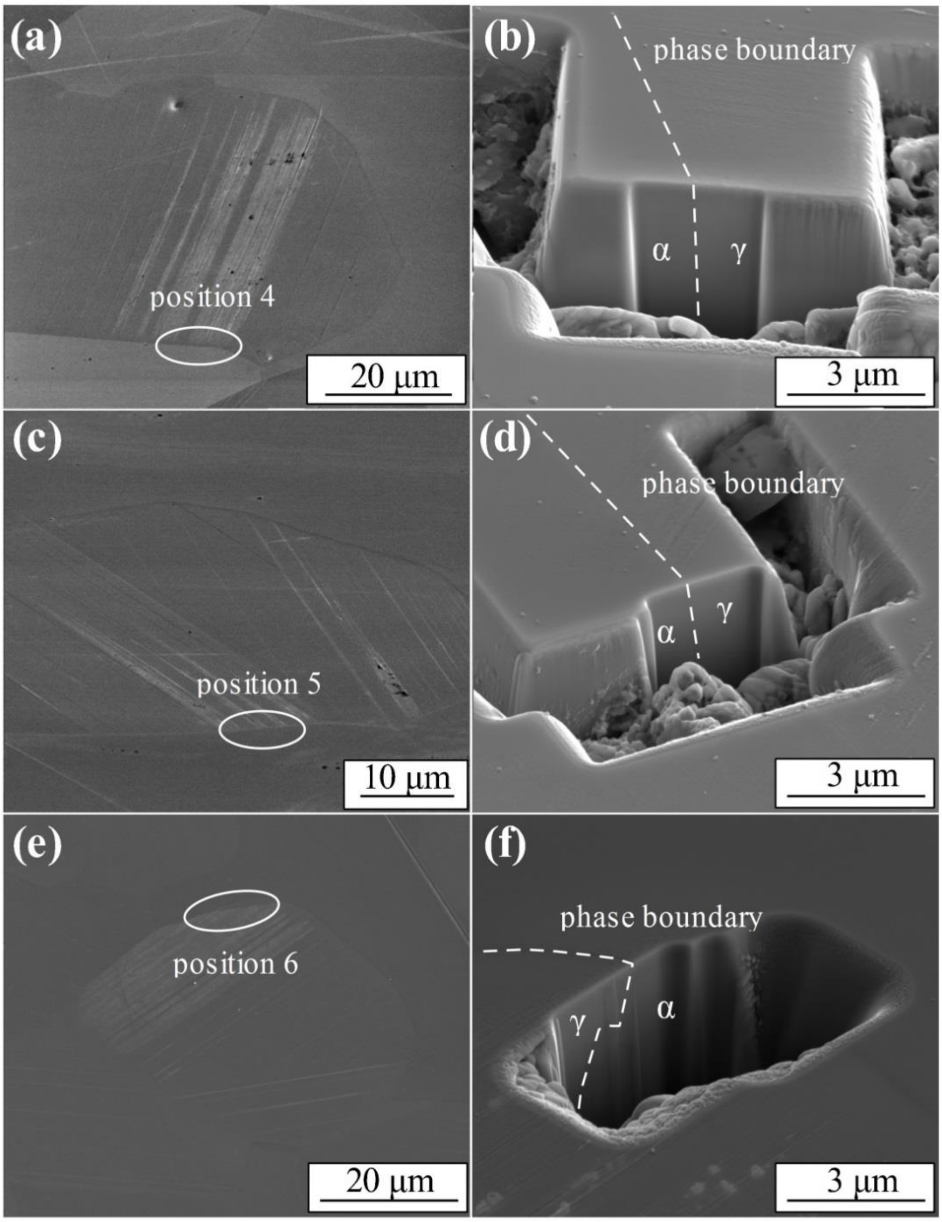

**Fig. 4.5.11:** Phase boundary orientation confirmed by FIB-cutting. (a), (c) and (e) are the selected positions where plastic deformation is arrested by the phase boundary, while (b), (d) and (f) show the phase boundary orientations. The angles between the phase boundary and the ferritic phase surface are between 90° and 180°.

Fig. 4.5.10 and Fig. 4.5.11 show an expected result and the importance of the phase boundary orientation is thus confirmed. The conclusions are summarised below:

- The morphology of the micro-crack formed on the surface is dependent on the phase boundary orientation below the surface.
- When the angle formed by the phase boundary and the ferritic surface is less than 90°, a large resultant shear stress forms. Plastic deformation easily takes place within the triangle zone formed

by the phase boundary, ferritic surface and the boundary where dislocations can glide to the surface. The intergranular micro-crack develops continuously with increasing number of fatigue load cycles.

- When the angle formed by the phase boundary and the ferritic surface lies between 90° and 180° or the phase boundary is perpendicular to the surface, the slip traces in austenite are frequently blocked and no plastic deformation occurs in the adjacent ferritic grain. In this case, transgranular micro-cracking occurs occasionally in ferrite, depending on the relationships among the shear stresses $\tau_1$, $\tau_2$ and $\tau_3$.

# 5 Concluding discussion

In this chapter, the typical elastic-plastic behaviour of the investigated DSS is summarised. Concluding discussions on crack initiation on the basis of all experimental findings will be presented.

The fatigue process can be explained by the motion and arrangement of dislocations which lead to changes with respect to residual stresses, slip markings and micro-hardness. When a DSS specimen is subjected to cyclic loading, austenitic grains with preferred orientations can be activated for plastic deformation. Dislocations in the austenitic phase glide to the surface of the specimen, forming slip markings and resulting in cyclic softening of the austenitic grains. Hence, an increase in the width of slip markings and a decrease in micro-hardness are observed.

Additionally, dislocation motion can be hindered by grain boundaries or phase boundaries. Further motion requires more driving force, which from a macroscopic perspective is termed as cyclic hardening. It is known that bcc metallic materials exhibit preferential cyclic hardening of the surface under high cycle fatigue conditions. This is caused by the emergence and loss of mobile non-screw dislocations. Such dislocations on primary glide planes are compensated by activation of secondary glide systems, leading to a hardening of the surface [112]. Measurements of cyclic hardening and cyclic softening of the whole DSS in the VHCF regime were performed by Düber [94] who monitored displacement changes of two points lying in the centre of a specimen along the loading axis as a function of the number of the cycles at stress amplitudes of 325 MPa, 350 MPa, 370 MPa and 400 MPa. The displacement over 20000 cycles applied in each test was found to be constant. No considerable cyclic hardening or cyclic softening was observed. Actually, as described, DSS in VHCF exhibits austenite-like behaviour as only the austenitic phase is plastic deformed. The cyclic hardening or cyclic softening behaviour described in this thesis, therefore, concerns only the austenitic phase. The ferritic phase remains inactivated and exhibits elastic behaviour.

With further fatigue loading, plastic deformation spreads into the adjacent ferritic grain. Again, cyclic softening occurs, which can be revealed by an increase in the width of slip markings and a decrease in the micro-hardness of austenite grains.

In summary, the austenite of the DSS in VHCF shows a continuous softening interrupted by a hardening, as documented in chapter 4. In order to better illustrate the concealed phenomena, four figures from chapter 4 are comparatively presented in Fig. 5.1.

The initial cyclic softening of austenite cannot change the lattice spacing of the materials. Hence, no appreciable development of micro residual stresses can be observed in Fig. 5.1(d). During this process, multiplication of dislocations occurs as well but is less significant compared with annihilation. According to the load partitioning results (Fig. 4.3.2), the ferritic phase carries more external load, meaning that the component shear stress $\tau_3$ is considerably larger in comparison to the value at the cyclic hardening stage. Early cracking dominated by this component can be found in Fig. 4.2.17 (at the load cycle number of $N=8\times10^4$).

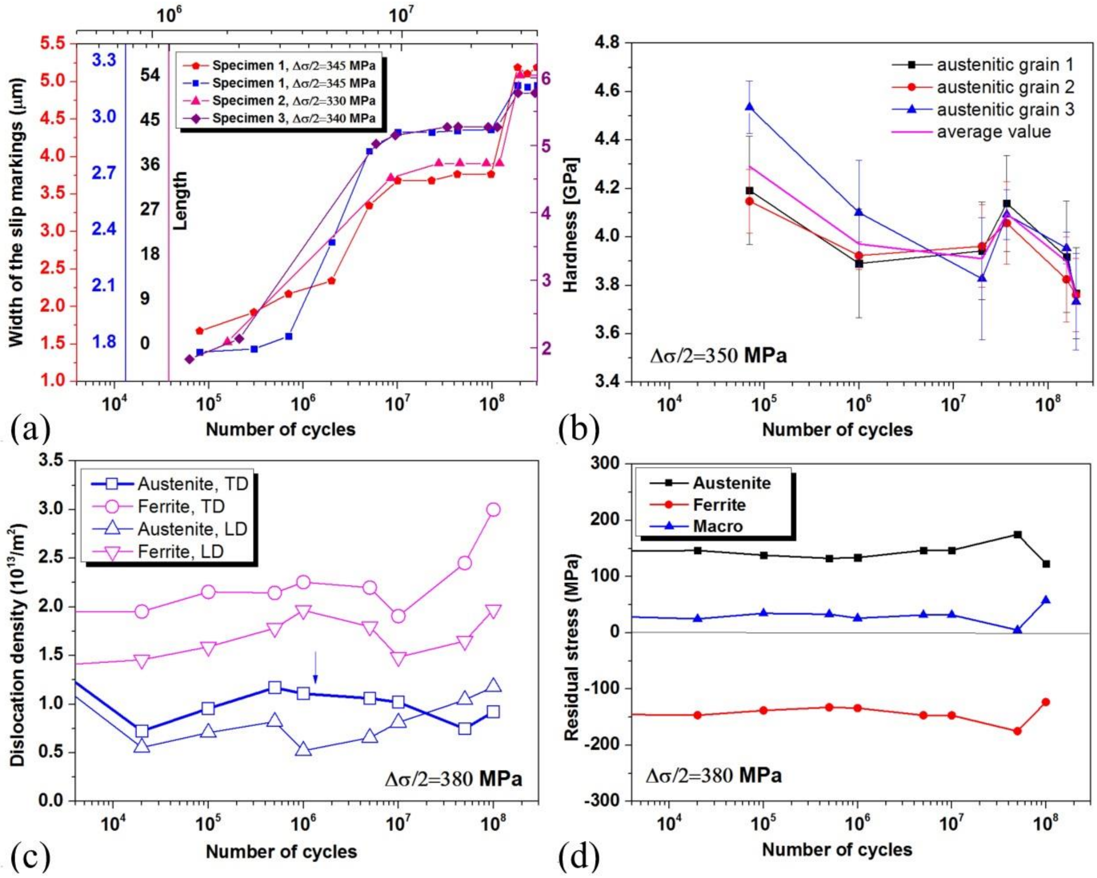

**Fig. 5.1:** The first three figures show a continuous cyclic softening interrupted by a short stage of cyclic hardening, the last figure shows only the cyclic hardening and cyclic softening stages (the initial cyclic softening cannot change the lattice spacing of the material and no obvious variation of the residual stresses is observed). The four figures represent a) development of slip markings, b) variation of micro-hardness, c) evolution of dislocation densities and d) changes of residual stresses.

Cyclic loading applied afterwards leads to accumulation of dislocation pile-ups at the phase boundary, resulting in nearby stress concentration. This stress in austenite acting as an obstacle for dislocation motion increases steadily with the accumulation of dislocation pile-ups. Subsequently, a hardening of the austenite can be observed, as shown in Fig. 5.1(b) from $N=2\times10^7$ to $N=3.5\times10^7$. Correspondingly, growth stop of slip markings, an increase in dislocation density and an increase in internal residual stresses are detected in this regime, as shown in Fig. 5.1(a), (c) and (d), respectively. At this stage, the shear stress $\tau_2$ increases continuously while the component $\tau_3$ decreases, leading to a change of the resultant shear stress both in amplitude and direction. When the resultant shear stress value reaches the critical resolved shear stress of the ferritic phase, dislocations start to move and micro-cracks can possibly form. A crack nucleus forming at this stage (at a load cycle number of $N=1.87\times10^8$) can be observed in Fig. 4.2.17. The plastic deformation taking place in ferrite releases the internal stresses between the two phases, leading to cyclic softening of the austenite. Again, slip markings then become broader and the micro-hardness decreases. Internal residual stresses at this stage are also observed to decrease. Such changes are illustrated in Fig. 5.1 at the relatively late stage of the fatigue process. The austenite of this DSS thus exhibits, as outlined, cyclic softening-hardening-softening behaviour, during which micro-cracks emerge and the material becomes 'homogeneous'. Repeated loading applied afterwards induces no micro-cracks. The already formed micro-cracks are frequently arrested in the ferrite grain and thus a true fatigue limit of this DSS is achieved.

# 6 Conclusions and future aspects

This work focused on the original crack initiation mechanisms of a DSS in the VHCF regime. Several high-resolution techniques were employed for investigation, in an attempt to explore the mechanisms of micro-crack formation. The separate results obtained are in good agreement with each other. The foremost important experimental findings are the cyclic hardening and cyclic softening of austenite that occur during the fatigue process. The cyclic behaviour of the austenite leads to the growth of slip markings, variation of micro-hardness and arrangement of dislocations. Micro-cracking that occurs in this period determines the fatigue lifetime of the DSS. The concluding remarks for the whole thesis are given below in detail.

Results from optical microscopy, nanoindentation tests and synchrotron radiation diffraction studies are in good agreement with each other and lead to the following conclusions:

- In the initial state of the DSS (after heat treatment), austenite contains a tensile micro residual stress, while ferrite carries the same amount of compressive micro residual stress to fulfil the mechanical equilibrium condition. TEM investigations show a moderate dislocation density in both phases.
- Cyclic loading applied afterwards leads to dislocation motion and annihilation, causing the initial cyclic softening of the austenite. Micro-hardness tests and optical studies performed in this stage show a decrease in micro-hardness and an increase in slip markings. The initial cyclic softening, however, cannot change the lattice spacing of the DSS and thus no development of residual stresses is observed.
- With further cyclic loading, dislocation pile-ups originating from the multiplication process prevail, leading to cyclic hardening of the austenite. Correspondingly, slip markings in austenite stop growing and the micro-hardness increases. Dislocation pile-ups at the phase boundary lead to an increase in internal residual stresses.
- Cyclic softening of austenite caused by the spread of plastic deformation into adjacent ferritic grains releases the internal residual stresses between the two phases. In this period, the micro-hardness of austenite becomes smaller and the slip markings grow again. TEM investigations performed in this stage show dislocation transmissions.
- The increase in internal residual stresses during cyclic hardening in VHCF is supported by the experiments executed in HCF which show a more pronounced increase in the early stage. TEM micrographs taken in HCF show strong dislocation pile-ups.

To investigate the plastic incompatibility and interactions between the two phases during cyclic loading, load sharing experiments were performed by means of in-situ XRD and in-situ DIC techniques at different fatigue load cycle numbers. The results obtained from the two methods lead to the following conclusions:

- Initially, austenite carries 39% of the external load stress. The percentage increases with the number of cycles due to the cyclic hardening of austenite. At a fatigue load cycle of N=$10^7$, austenite carries about 53% of the external load stress. Cyclic softening of austenite taking place subsequently leads to a decrease in the load sharing index. The development of the load sharing index indicates that the relative harder phase carries more external load stress.
- The micro yield stress of the austenite of the DSS is approximately 207 MPa. For load stress below this amplitude, no plastic deformation is expected to occur.
- The micro yielding of austenite leads to a redistribution of the micro residual stresses. With an increase of load cycles, internal residual stresses accumulate gradually.
- Cyclic loading leads to an increase in the micro yield stress of austenite. At a fatigue load cycle number of N=$10^7$, the micro yield stress of the austenite is about 256 MPa, indicating a cyclic hardening of this phase takes place. This agrees well with the ex-situ experimental findings.
- In-situ strain partitioning studied by DIC indicates that the initial inhomogeneity leads to strain partitioning of the material.
- The cyclic softening-hardening-softening process causes a ‘homogenization’ process. Plastic deformation occurring in ferrite releases the internal residual stresses at stress intensification sites, resulting in localised residual strain.
- After the cyclic softening-hardening-softening process, the two phases carry almost the same amount of applied strain, which is in accordance with the in-situ XRD experiments. These experimental findings suggest that the initial cyclic loading cycles ($<10^8$) are significant for the micro-crack initiation of the DSS.

The formations of two kinds of micro-cracks were discussed based on both the experimental findings and theoretical concepts. It is established that crack initiation in this study is dependent on the resultant shear stress near the phase boundary which is composed of 1) shear stress $\tau_1$ due to the accumulation of intrusions and extrusions (slip of dislocations), 2) shear stress $\tau_2$ due to dislocation pile-ups and 3) shear stress $\tau_3$ due to external load stress. Of the three components, the shear stress $\tau_2$ which is strongly dependent on phase boundary orientation determines the morphology of the micro-cracks. The phase boundary orientations were determined by means of FIB-cutting and the following conclusions are drawn from the results of the investigation:

- When the angle formed by the phase boundary and the ferritic surface is less than 90°, slip traces in austenite trigger frequently plastic deformation in ferrite. In this case, an intergranular micro-crack forms continuously with an increasing number of cycles.
- When the angle formed by the phase boundary and the ferritic surface is between 90° and 180° or the phase boundary lies perpendicular to the surface, the slip traces in austenite are mostly

blocked and no plastic deformation takes place in the adjacent ferritic grain. Under the same circumstances, transgranular micro-cracks form occasionally, depending on the mechanical relationships among the shear stresses $\tau_1$, $\tau_2$ and $\tau_3$.

The future aspects of a continuation of this thesis can be focused on:

- A quantifying study of the shear stresses $\tau_1$, $\tau_2$ and $\tau_3$ is an essential first step. The determination of the local residual stresses (corresponding to the shear stress $\tau_2$ in this thesis) in micro scales can be achieved by a combination of FIB-milling, SEM imaging, DIC analysis and FEM modelling [113-115]. A nanoindentation testing method which presumes an isotropic stress field at the measured location provides an alternative way to determine the local residual stresses [116, 117]. FEM modelling of the shear stresses $\tau_1$ and $\tau_3$ is also significant and interesting.
- The more sophisticated technique of positron annihilation microscopy could provide a higher resolution for developing new insights into the mechanisms of VHCF.
- The micro-cracks are frequently arrested by the second grain and an infinite fatigue lifetime is achieved within $10^9$ cycles. Investigations applying a very high number of load cycles would be significant in both theoretical and practical aspects.

# 7 Appendix

The classic Williamson-Hall plot was modified [118] where $K$ is replaced by $K\bar{C}^{1/2}$ based on the following equation, as shown in equation 7.1. Its quadratic form is equation 7.2.

$$\Delta K \cong \frac{0.9}{d} + \left(\frac{\pi M^2 b^2}{2}\right)^{1/2} \rho^{1/2}\left(K\bar{C}^{1/2}\right) + O\left(K^2\bar{C}\right) \tag{7.1}$$

$$(\Delta K)^2 \cong \left(\frac{0.9}{d}\right)^2 + \left(\frac{\pi M^2 b^2}{2}\right)\rho\left(K^2\bar{C}\right) + O\left(K^4\bar{C}^2\right) \tag{7.2}$$

where $\Delta \mathrm{K} = \cos\theta(\Delta 2\theta)/\lambda$, $\mathrm{K} = 2\sin\theta/\lambda$, $\theta$ is the diffraction angle, $\Delta 2\theta$ is the integral breadth (FWHM) of the diffraction peak , $\lambda$ is the wavelength of the X-rays, d is the average subgrain size, b is the magnitude of the Burgers vector of the dislocations and $\rho$ is the average dislocation density. O is the noninterpreted higher-order term. $M$ is a constant depending on both the effective outer cut-off radius of the dislocations and the dislocation density. The value of M varies in between 1 and 2 for the deformed materials and is less than 1 for low dislocation density materials [119, 120]. In this study, as the experiments were carried out in the regime of VHCF, dislocation generation is scarce. A value of $\mathrm{M} = 0.8$ was applied to reveal the relative changes of the dislocation densities. $\bar{C}$ represents the average contrast factor of the dislocations for all the reflections. The averaged value can be calculated as follows:

$$\bar{C} = \overline{C_{h00}}\left(1 - qH^2\right) \tag{7.3}$$

$$H^2 = \left(h^2k^2 + h^2l^2 + k^2l^2\right)/\left(h^2 + k^2 + l^2\right)^2 \tag{7.4}$$

$\overline{C_{h00}}$ is the average dislocation contrast factor for the $h00$ reflection and is dependent on the anisotropic factor of the material. $q$ is the parameter depending on the elastic constants and on the character of dislocations in the crystal. It denotes the ratio of screw dislocation and edge dislocation in the material. Ungár et al. [121] suggested methods for calculating both the theoretical and experimental factors $q$ and $\overline{C_{h00}}$ using simple analytical functions. The experimental method is to plot the values of $[(\Delta K)^2 - \alpha]$ against $H^2$ by combining equations 7.2, 7.3 and 7.4.

$$[(\Delta K)^2 - \alpha]/K^2 \cong \beta\overline{C_{h00}}\left(1 - qH^2\right) \tag{7.5}$$

where $\alpha = (0.9/d)^2$ and $\beta = \frac{\pi \mathrm{M}^2 \mathrm{b}^2 \rho}{2}$. The intersection of the fit line with the x-axis is the reciprocal of $q$. In the present study, the values of $q$ for the austenite and ferrite were determined for each interruption. The results are listed as below:

**Table 7.1:** Value of $q$ of austenite and ferrite during fatigue.

| cycles | 0 | $2\times10^4$ | $10^5$ | $5\times10^5$ | $10^6$ | $5\times10^6$ | $10^7$ | $5\times10^7$ | $10^8$ |
|---|---|---|---|---|---|---|---|---|---|
| austenite | 2.07 | 2.12 | 2.01 | 2.1 | 2.13 | 2.14 | 2.09 | 2.07 | 2.07 |
| ferrite | 1.45 | 1.44 | 1.4 | 1.44 | 1.45 | 1.42 | 1.45 | 1.39 | 1.4 |

The factor $q$ in table 7.1 varies slightly and can be considered as a constant. The related parameter $\overline{C_{h00}}$ during fatigue were calculated from the figures listed in [121] when the anisotropic factor $A_i$ is known.

**Table 7.2:** Average $\overline{C_{h00}}$ values of the austenite and ferrite used in the present investigation.

| | $C_{11}$ (GPa) | $C_{12}$ (GPa) | $C_{44}$ (GPa) | $A_i=2C_{44}/(C_{11}-C_{12})$ | $\overline{C_{h00}}$ |
|---|---|---|---|---|---|
| austenite | 205 | 135 | 125 | 3.57 | 0.31 |
| ferrite | 233.1 | 135.4 | 117.8 | 2.41 | 0.2 |

Actually, the parameters can be acquired in a more simple manner as described in [98]. This can be either done through a web frontend or from the free downloaded software developed by the authors. Eventually, the modified Williamson-Hall method can be employed according to equation 4.4. A representation of the modified Williamson-Hall plot is shown in Fig. 7.1.

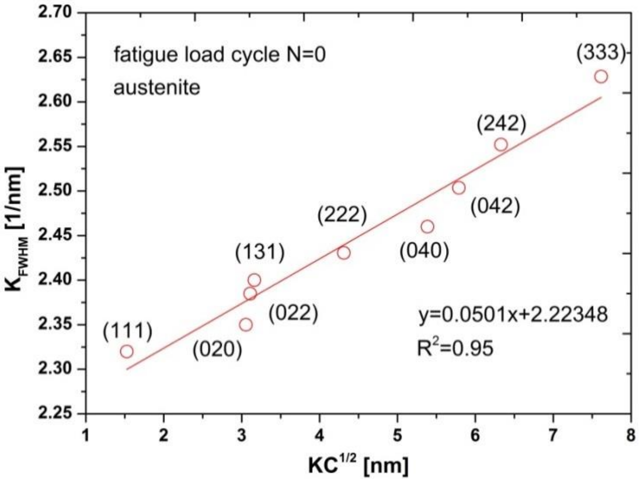

**Fig. 7.1:** A representation of the modified Williamson-Hall plot for dislocation determination.

Dislocation density can be then calculated from the slope of the fit line, which is:

$$\rho = \frac{2m}{\pi M^2 b^2} \tag{7.6}$$

# 8 References

[1] Whöler, A., Versuche über die Festigkeit der Eisenbahnwagenachsen, Zeitschrift für Bauwesen, 10 (1860) 583-616.

[2] Irwin, G.R., Analysis of stresses and strains near the end of a crack traversing a plate, Journal of Applied Mechanics, 24 (1957) 361-364.

[3] Paris, P.C., Gomez, M.P., Anderson, W.P., A rational analytic theory of fatigue, The Trend in Engineering, 13 (1961) 9-14.

[4] Bauschinger, J., Über die Veränderungen der Elastizitätsgrenze und der Festigkeit des Eisens und Stahls durch Strecken, Quetschen, Erwärmen, Abkühlen und durch oftmals wiederholte Belastung, Mitt. Mech-Tech Lab., München, 1986.

[5] Ewing, J., Humfrey, J.C., The fracture of metals under rapid alterations of stress, Philosophical Transactions of the Royal Society, 22 (1903) 241-250.

[6] Thompson, N., Wadsworth, N.J., Louat, N., The origin of fatigue fracture in copper, Philosophical Magazine, 1 (1956) 113-126.

[7] Elber, W., Fatigue crack closure under cyclic tension, Engineering Fracture mechanics, 2 (1970) 37-45.

[8] Ritchie, R.O., Suresh, S., and Moss, C.M., Near-threshold fatigue crack growth in Cr-Mo pressure vessel steel in air and hydrogen, Journal of Engineering Materials and Technology, 102 (1980) 291-299.

[9] Ritchie, R.O., Suresh, S., Some considerations on fatigue crack closure at near threshold stress intensities due to fracture surface morphology, Metallurgical Transactions, 13 (1981) 937-940.

[10] Essmann, U., Gösele, U., Mughrabi, H., A model of extrusions and intrusions in fatigued metals I. Point-defect production and the growth of extrusions, Philosophical Magazine A, 44 (1981) 405-426.

[11] Polák, J., Resistivity of fatigued copper single crystals, Materials Science and Engineering, 89 (1987) 35-43.

[12] Naito, T., Udda, H., Kikuchi, M., Observation of fatigue fracture surface of carburized steel, Journal of the Society Material Science, 32 (1983) 162-166.

[13] Bathias, C., There is no infinite fatigue life in metallic materials, Fatigue and Fracture of Engineering Materials and Structures, 22 (1999) 559-565.

[14] Mughrabi, H., Specific features and mechanisms of fatigue in the ultrahigh-cycle regime, International Journal of Fatigue, 28 (2006) 1501-1508.

[15] Christ, H.J., Zimmerman, M., Stöcker, C., Müller-Bollenhagen, C., Aktuelle Fragestellungen, experimentelle Herausforderungen und neue Forschungsergebnisse zum Ermüdungsverhalten metallischer Werkstoffe im Bereich sehr hoher Lastspielzahlen in: Tagungsband Werkstoffprüfung, Borsutzki, M. und Geisler, S. (eds), Verlag Stahleisen GmbH, Düsseldorf, 2009, 7-14.

[16] Sahu, J.K., Effect of 475 °C embrittlement on the fatigue behaviour of a duplex stainless steel, Doctorate Thesis, Siegen, 2008.

[17] Suresh, S., Fatigue of materials, Cambridge University Press, Cambridge, 1998.

[18] Neuhäuser, H., Arkan, O.B., Potthoff, H.-H. , Dislocation multipoles and estimation of frictional stress in f.c.c. copper alloys, Materials Science and Engineering, 81 (1986) 201-209.

[19] Amodeo, R.J., Ghoniem, N.M., Dislocation dynamics I: A proposed methodology for deformation micromechanics, Physical Review B, 41 (1990) 6958-6967.

[20] Man, J., Obrtlík, K., Polák, J., Extrusions and intrusions in fatigued metals. Part 1. State of the art and history, Philosophical Magazine, 89 (2009) 1295-1336.

[21] Stöcker, C., Zimmermann, M., Christ, H.J., Localized cyclic deformation and corresponding dislocation arrangements of polycrystalline Ni-base superalloys and pure nickel in the VHCF regime, International Journal of Fatigue, 33 (2011) 2-9.

[22] Dönges, B., Giertler, A., Krupp, U., Fritzen, C.P., Christ, H.J., Significance of crystallographic misorientation at phase boundaries for fatigue crack initiation in a duplex stainless steel during high and very high cycle fatigue loading, Materials Science and Engineering A, 589 (2014) 146-152.

[23] Antonopoulos, J.G., Brown, L.M., Winter, A.T., Vacancy dipoles in fatigued copper, Philosophical Magazine, 34 (1976) 549-563.

[24] Brown, L.M., Ogin, S.L., Role of internal stresses in the nucleation of fatigue cracks in Fundamentals of Deformation and Fracture, Bilby, B.A., Miller, K.J. and Willis, J.R. (eds), Cambridge University Press, Cambridge, 1985, 501.

[25] Brown, L.M., Nabarro, F.R.N. , The enumeration and transformation of dislocation dipoles II. The transformation of interstitial dipoles into vacancy dipoles in an open dislocation array, Philosophical Magazine, 84 (2004) 441-450.

[26] Basinski, Z.S., Basinski, S.J., Fundamental aspects of low-amplitude cyclic deformation in face- centered cubic crystals, Progress in Materials Science, 36 (1992) 89-148.

[27] Brown, L.M., Deformation mechanisms leading to the initiation and slow growth of fatigue cracks, in: Modelling of Material Behavior and Design, Embury, J.D. and Thompson, A.W. (eds)., TMS-AIME, Warrendale, 1990, 175.

[28] Polák, J., Man, J., Obrtlík, K., AFM evidence of surface relief formation and models of fatigue crack nucleation, International Journal of Fatigue, 25 (2003) 1027-1036.

[29] Mughrabi, H., Cyclic slip irreversibilities and the evolution of fatigue damage, Metallurgical and Materials Transactions B, 40 (2009) 431-453.

[30] Polák, J., On the role of point defects in fatigue crack initiation, Materials Science and Engineering, 92 (1987) 71-81.

[31] Hsiung, L.M., Stoloff, N.S., A point defect model for fatigue crack initiation in Ni3Al+B single crystals, Acta Metallurgica et Materialia, 38 (1990) 1191-1200.

[32] Tanaka, K., Mura, T., A dislocation model for fatigue crack initiation, Journal of Applied Mechanics, 48 (1981) 97-103.

[33] Zhai, T.-G., Lin, S., Xiao, J.-M., Influence of non-geometric effect of PSB on crack initiation in aluminium single crystal, Acta Metallurgica et Materialia, 38 (1990) 1687-1692.

[34] Zhai, T., Martin, J.W., Briggs, G.A.D., Fatigue damage in aluminum single crystals—I. On the surface containing the slip burgers vector, Acta Metallurgica et Materialia, 43 (1995) 3813-3825.

[35] Lin, T.H., Lin, S.R., Micromechanics theory of fatigue crack initiation applied to time-dependent fatigue, in: Fatigue Mechanisms, ASTM STP 675 , Fong, J.T. (ed), American Society for Testing and Materials, Philadelphia, 1979, 707.

[36] Basinski, Z.S., Basinski, S.J., Copper single crystal PSB morphology between 4.2 and 350 K, Acta Metallurgica, 37 (1989) 3255-3262.

[37] Mughrabi, H., On the life-controlling microstructural fatigue mechanism in ductile metals and alloys in the gigacycle regime, Fatigue and Fracture Engineering of Materials and Structures, 22 (1999) 633-641.

[38] Mughrabi, H., On multi-stage fatigue life diagrams and the relevant life-controlling mechanism in ultrahigh-cycle fatigue, Fatigue and Fracture of Engineering Materials and Structures, 25 (2002) 755-764.

[39] Mughrabi, H., Fatigue crack initiation mechanisms and fatigue life in high-cycle, in: Fatigue – David L. Davidson Symposium, Ultrahigh-cycle fatigue, Chan K.S., Liaw P.K., Bellows R.S., Togas T.C. and Soboyejo W.O. (eds), Warrendale TMS, 2002, 3–15.

[40] Mayer, H., Fatigue damage of low amplitude cycles under variable amplitude loading condition, in: Proc VHCF 4, Allison, J.E., Jones, J.W., Larsen, J.M. and Ritchie, R.O. (eds),University of Michigan Ann Arbor, Michigan, 2007, 333–340.

[41] Pyttel, B., Schwerdt, D., Berger, C., Very high cycle fatigue behaviour of two different aluminium wrought alloys, in: Proc VHCF 4, Allison, J.E., Jones, J.W., Larsen, J.M. and Ritchie, R.O. (eds), University of Michigan Ann Arbor, Michigan, 2007, 313–318.

[42] Sakai, T., Oguma, N., Harada, H., Strength level dependence of very high cycle fatigue property in interior inclusion-induced fracture for bearing steel in rotating bending, in: Proc VHCF 4, Allison, J.E., Jones, J.W., Larsen, J.M. and Ritchie, R.O. (eds),University of Michigan Ann Arbor, Michigan, 2007, 129–136.

[43] Sonsino, C.M., Course of SN-curves especially in the high-cycle fatigue regime with regard to component design and safety, International Journal of Fatigue, 29 (2007) 2246-2258.

[44] Pyttel, B., Schwerdt, D., Berger, C., Very high cycle fatigue – Is there a fatigue limit?, International Journal of Fatigue, 33 (2011) 49-58.

[45] Murakami, Y., Nomoto, T., Ueda, T., Factors influencing the superlong fatigue failure in steels, Fatigue and Fracture Engineering of Materials and Structures, 22 (1999) 581-590.

[46] Murakami, Y., Matsunaga, H., The effect of hydrogen on fatigue properties of steels for fuel cell system, International Journal of Fatigue, 28 (2006) 1509-1520.

[47] Murakami, Y., Endo, M., Effects of defects, inclusions and inhomogeneities on fatigue strength, International Journal of Fatigue, 16 (1994) 163-182.

[48] Sakai, T., Crack initiation mechanism of bearing steel in very high cycle fatigue, in: Proc ECF 16, Carpinteri, A. (ed), Alexandroupolis, 2006.

[49] Mateo, A., Anisotropy effects on the fatigue behaviour of rolled duplex stainless steels, International Journal of Fatigue, 25 (2003) 481-488.

[50] Leffler, B., Stainless steels and their properties, Avesta Sheffield AB Research Foundation, Stockholm, 1996, 30.

[51] Eckenrod, J.J., Kovach, C.W., Effect of nitrogen on the sensitization, corrosion and mechanical properties of 18Cr-8Ni stainless steels, Ohio: Materials Park, ASM-STP 679, 1979, 17.

[52] Nordberg, H., Mechanical properties of austenitic and duplex stainless steels, Avesta Sheffield Research Foundation, Innovation Stainless Steels, Florence, 1993, 217.

[53] Jia, N., Deformation behaviors of duplex stainless steel studied by in-situ experiments and self-consistent modeling, Doctorate Thesis, Shenyang, 2008.

[54] Pohl, M., The ferrite/austenite ration of duplex stainless steels, Zeitschrift für Metallkunde, 86 (1995) 97-102.

[55] Kovach, C.W., High-performance stainless steels, Pittsburgh: Technical report for Technical Marketing Resources, Inc. of Pittsburgh, Pennsylvania, 2000.

[56] Moverare, J.J., Odén, M., Deformation behaviour of a prestrained duplex stainless steel, Materials Science and Engineering A, 337 (2002) 25-38.

[57] Rossini, N.S., Dassisti, M., Benyounis, K.Y., Olabi, A.G., Methods of measuring residual stresses in components, Materials Design, 35 (2012) 572-588.

[58] Kloos, E., Eigenspannungen, Definition und Entstehungsurachen, Zeitschrift für Werkstofftechnik, 10 (1979) 293-332.

[59] Reimers, W., Pyzalla, A.R., Schreyer, A., Helmut, C., Neutron and synchrotron radiation in engineering materials science, WILEY-VCH Verlag GmbH Co. KGaA, Weiheim, 2008, 25.

[60] Özdemir, T., Edwards, L., Relaxation of residual stresses at cold-worked fastener holes due to fatigue loading, Fatigue and Fracture of Engineering Materials and Structures, 20 (1997) 1443-1451.

[61] Iida, K., Taniguchi, L., Relaxation of residual stress distribution produced by shot peening under fatigue test, Champaigne, J. (ed), in: Proceedings of 6th International Conference on shot peening, UB/TB Hannover press, San Francisco, 1996, 397-402.

[62] Torres, M.A.S., Voorwald, H.J.C., An evaluation of shot peening, residual stress and stress relaxation on the fatigue life of AISI 4340 steel, International Journal of Fatigue, 24 (2002) 877-886.

[63] Juijerm, P., Altenberger, I., Scholtes, B., Fatigue and residual stress relaxation of deep rolled differentlz aged aluminium alloy AA6110, Materials Science and Engineering A, 426 (2006) 4-10.

[64] Zaroog, O.S., Ali, A., Sahari, B.B., Zahari, R., Relaxation of residual stress, Part 2: relaxation of stage 2, American Journal of Engineering and Applied Science, 2 (2009) 759-763.

[65] Possel-Dölken, I., Röntgenographische Bestimmung von Mikrospannungen in polykristallinen Werkstoffen und ihr Verhalten bei statischer Verformung und schwingender Beanspruchung, Doctorate Thesis, Aachen, 2007.

[66] Hauk, V., Nikolin, H.-J., Mikroeigenspannungen in einem ferritischen und einem ferritisch austenitischen Stahl, Stabilität/Abbau bei der Schwingbeanspruchung., in: Gefüge und Bruch, Gebrüder Bornträger Berlin-Stuttgart, Materialkundl.-Techn. Reihe, Maurer, K.L. and Pohl, M. (eds), 1990, 173-180.

[67] Johansson, J., Odén, M., Load sharing between austenite and ferrite in a duplex stainless steel during cyclic loading, Metallurgical and Materials Transaction A, 31A (1999) 1557-1570.

[68] Totten, G., Howes, M., Inoue, T., Handbook of residual stress and deformation of steel, ASM international 2002, 63.

[69] Almer, J.D., Cohen, J.B., Moran, B., The effects of residual macrostresses and microstresses on fatigue crack initiation, Materials Science and Engineering A, 284 (2000) 268-279.

[70] Webster, G.A., Residual stress distrubtion and their influence on fatigue lifetimes, International Journal of Fatigue, 23 (2001) S375-S383.

[71] Almer, J.D., Cohen, J.B., Winholtz, R.A., The effects of residual macrostresses and microstresses on fatigue crack propagation, Metallurgical and Materials Transaction A, 29 (1998) 2127-2136.

[72] Chai, G., The formation of subsurface non-defect fatigue crack origins, International Journal of Fatigue, 28 (2006) 1533-1539.

[73] Eshelby, J.D., The determination of the elastic field of an ellipsoidal inclusion, and related problems, Proceedings Royal Society A, 241 (1957) 376-396.

[74] Artemev, A., Wang, Y., Khachaturyan, A.G., Three-dimensional phase field model and simulation of martensitic transformation in multilayer systems under applied stresses, Acta Materialia, 48 (2000) 2503-2518.

[75] Yin, H.M., Sun, L.Z., Paulino, G.H., Micromechanics-based elastic model for functionally graded materials with particle interactions, Acta Materialia, 52 (2004) 3535-3543.

[76] Heo, T.W., Chen, L.Q., Phase-field modeling of displacive phase transformations in elastically anisotropic and inhomogeneous polycrystals, Acta Materialia, 76 (2014) 68-81.

[77] Hauk, V., Structural and residual stress analysis by nondestructive methods: evaluation-application-assessment, Elsevier Science B.V., 1997, 254.

[78] Bacon, D.H., Edwards, L., Moffatt, J.E., Fitzpatrick, M.E., Synchrotron X-ray diffraction measurements of internal stresses during loading of steel-based metal matrix composites reinforced with $TiB_2$ particles, Acta Materialia, 59 (2011) 3373-3383.

[79] Alharbi, K., Ghadbeigi, H., Efthymiadis, P., Zanganeh, M., Celotto, S., Dashwood, R., Pinna, C., Damage in dual phase steel DP1000 investigated using digital image correlation and microstructure simulation, Modelling and Simulation in Materials Science and Engineering, 23 (2015) 085005.

[80] Ososkova, Y., Wilkinsona, D.S., Jainc, M., Simpsonb, T., In-situ measurement of local strain partitioning in a commercial dual-phase steel, International Journal of Materials Research, 98 (2007) 664-673.

[81] Ghadbeigi, H., Pinna, C., Celotto, S., Yates, J.R., Local plastic strain evolution in a high strength dual-phase steel, Materials Science and Engineering A, 527 (2010) 5026-5032.

[82] Krupp, U., Knobbe, H., Christ, H.-J., Köster, P., Fritzen, C.-P., The significance of microstructural barriers during fatigue of a duplex steel in the high- and very-high-cycle-fatigue (HCF/VHCF) regime, International Journal of Fatigue, 32 (2010) 914-920.

[83] Krupp, U., Giertler, A., Söker, M., Fu, H., Dönges, B., Christ, H.J., Hüsecken, A., Pietsch, U., Fritzen, C.P., Ludwig, W., The behavior of short fatigue cracks during very high cycle fatigue (VHCF) of duplex stainless steel, Engineering Fracture Mechanics, 145 (2015) 197-209.

[84] Düber, O., Künkler, B., Krupp, U., Christ, H.-J., Fritzen, C.-P., Experimental characterisation and two-dimensional simulation of short-crack propagation in an austenitic-ferritic duplex steel, International Journal of Fatigue, 28 (2006) 983-992.

[85] Wang, Q.Y., Étude de la fatigue oligocyclique des alliages ferreux, Doctorate Thesis, École Centrale de Paris, 1998.

[86] Jia, N., Cong, Z.H., Sun, X., Cheng, S., Nie, Z.H., Ren, Y., Liaw, P.K., Wang, Y.D., An in situ high-energy X-ray diffraction study of micromechanical behavior of multiple phases in advanced high-strength steels, Acta Materialia, 57 (2009) 3965-3977.

[87] Wang, X.L., Wang, Y.D., Stoica, A.D., Horton, D.J., Tian, H., Liaw, P.K., Choo, H., Richardson, J.W., Maxey, E., Inter- and intragranular stresses in cyclically-deformed 316 stainless steel, Materials Science and Engineering A, 399 (2005) 114-119.

[88] Jia, N., Peng, R., Wang, Y., Chai, G., Johansson, S., Wang, G., Liaw, P., Interactions between the phase stress and the grain-orientation-dependent stress in duplex stainless steel during deformation, Acta Materialia, 54 (2006) 3907-3916.

[89] Mateo, A., Llanes, L., Itugoyen, L., Anglada, M., Cyclic stress-strain response and dislocation substructure evolution of a ferrite-austenite stainless steel, Acta Materialia, 44 (1996) 1143-1153.

[90] Lianes, L., Mateo, A., Iturgoyen, L., Anglada, M., Aging effects on the cyclic deformation mechanisms of a duplex strainless steel, Acta Materialia, 44 (1996) 3967-3978.

[91] Xia, Y.B., Wang, Z.G., Low cycle fatigue behavior of a new type of stainless steel, Materials Science and Engineering A, 151 (1992) 29-35.

[92] Kruml, T., Polák, J, Obrtlik, K., Degallaix, S., Dislocation structures in the bands of localized cyclic plastic strain in austenitic 316L and austenitic-ferritic duplex stainless steels, Acta Materialia, 45 (1997) 5145-5151.

[93] Mateo, A., Girones, A., Keichel, J., Llanes, L., Akdut, N., Anglada, M., Cyclic deformation behavior of superduplex stainless steels, Materials Science and Engineering A, 314 (2001) 176-185.

[94] Düber, O., Untersuchungen zum Ausbreitungsverhalten mikostrukturell kurzer Ermüdungsrisse in zweiphasigen metallischen Werkstoffen am Beispiel eines austenitisch-ferritischen Duplexstahls, Doctorate Thesis, Siegen, 2006.

[95] Istomin, K., Dönges, B., Schell, N., Christ, H.-J., Pietsch, U., Analysis of VHCF damage in a duplex stainless steel using hard X-ray diffraction techniques, International Journal of Fatigue, 66 (2014) 177-182.

[96] Fischer-Cripps, A.C., Nanoindentation, Springer, 2011, 30.

[97] Woo, W., Ungár, T., Feng, Z., Kenik, E., Clausen, B., X-ray and neutron diffraction measurements of dislocation density and subgrain size in a friction-stir-welded aluminum alloy, Metallurgical and Materials Transactions A, 41 (2009) 1210-1216.

[98] Ribárik, G., Ungár, T., Characterisation of the microstructure in random and textured polycrystals and single crystals by diffraction line profile analysis, Materials Science and Engineering: A, 528 (2010) 112-121.

[99] Xiong, Z., Naoe, T., Wan, T., Futakawa, M., Maekawa, K., Mechanical property change in the region of very high cycle fatigue, Procedia Engineering, 101 (2015) 552-560.

[100] Knobbe, H., Starke, P., Hereñú, S., Christ, H.J., Eifler, D., Cyclic deformation behaviour, microstructural evolution and fatigue life of duplex steel AISI 329 LN, International Journal of Fatigue, 80 (2015) 81-89.

[101] Mateo, A., Llanes, L., Iturgoyen, L., Anglada, M., Cyclic stress-strain response and dislocation substructures evolution of a ferrite-austenite stainless steel, Acta Materialia, 44 (1996) 1143-1153.

[102] Zavattieri, P.D., Espinosa, H.D., Grain level analysis of crack initiation and propagation in brittle materials, Acta Materialia, 49 (2001) 4291-4311.

[103] Peng, R. L., Chai, G. C., Ellerman, A., Johansson, S., Manns, T., Microscopic load sharing in a duplex stainless steel and the influence of phase properties, Material Science Forum, 52 (2009) 328-335.

[104] Kammers, A.D., Daly, S., Samll-scale patterning methods for digital image correlation under scanning electron microscopy, Measurement Science and Technology, 22 (2011) 125501.

[105] Prasad Reddy, G.V., Robertson, C., Déprés, C., Fivel, M., Effect of grain disorientation on early fatigue crack propagation in face-centred-cubic polycrystals: A three-dimensional dislocation dynamics investigation, Acta Materialia, 61 (2013) 5300-5310.

[106] Dönges, B., Istomin, K., Söker, M., Schell, N., Krupp, U., Pietsch, U., Fritzen, C.P., Christ, H.J., Experimental investigation and numerical description of the damage evolution in a duplex stainless steel subjected to VHCF-loading, Materials Science and Engineering A, 646 (2015) 8-18.

[107] Gururaj, K., Robertson, C., Fivel, M., Channel formation and multiplication in irradiated fcc metals: a 3D dislocation dynamics investigation, Philosophical Magazine, 95 (2015) 1368-1389.

[108] Déprés, C., Robertson, C.F., Fivel, M.C., Low-strain fatigue in 316L steel surface grains: a three dimension discrete dislocation dynamics modelling of the early cycles. Part 2: Persistent slip markings and micro-crack nucleation, Philosophical Magazine, 86 (2006) 79-97.

[109] Déprés, C., Robertson, C.F., Fivel, M.C., Low-strain fatigue in AISI 316L steel surface grains: a three-dimensional discrete dislocation dynamics modelling of the early cycles I: Dislocation microstructures and mechanical behaviour, Philosophical Magazine, 84 (2004) 2257-2275.

[110] Déprés, C., Prasad Reddy, G.V., Robertson, C., Fivel, M., An extensive 3D dislocation dynamics investigation of stage-I fatigue crack propagation, Philosophical Magazine, 94 (2014) 4115-4137.

[111] Déprés, C., Fivel, M., Tabourot, L., A dislocation-based model for low-amplitude fatigue behaviour of face-centred cubic single crystals, Scripta Materialia, 58 (2008) 1086-1089.

[112] Mughrabi, H., Dislocations and properties of real materials, Lerotto, M.H. (Ed), Insitute of Metals, London, 1984, 244-262.

[113] Korsunsky, A.M., Sebastiani, M., Bemporad, E., Residual stress evaluation at the micrometer scale: Analysis of thin coatings by FIB milling and digital image correlation, Surface and Coatings Technology, 205 (2010) 2393-2403.

[114] Sebastiani, M., Eberl, C., Bemporad, E., Pharr, G.M., Depth-resolved residual stress analysis of thin coatings by a new FIB–DIC method, Materials Science and Engineering A, 528 (2011) 7901-7908.

[115] Massl, S., Keckes, J., Pippan, R., A direct method of determining complex depth profiles of residual stresses in thin films on a nanoscale, Acta Materialia, 55 (2007) 4835-4844.

[116] Charitidis, C.A., Dragatogiannis, D.A., Koumoulos, E.P., Kartsonakis, I.A., Residual stress and deformation mechanism of friction stir welded aluminum alloys by nanoindentation, Materials Science and Engineering A, 540 (2012) 226-234.

[117] Khan, M.K., Fitzpatrick, M.E., Hainsworth, S.V., Evans, A.D., Edwards, L., Application of synchrotron X-ray diffraction and nanoindentation for the determination of residual stress fields around scratches, Acta Materialia, 59 (2011) 7508-7520.

[118] Ungár, T., Borbey, A., The effect of dislocation contrast on X-ray line broadening: A new approach to line profile analysis, Applied Physics Letters, 69 (1996) 3173-3175.

[119] Ungár, T., Dislocation densities, arrangements and character from X-ray diffraction experiments, Materials Science and Engineering A, 309-310 (2001) 14-22.

[120] Ribárik, G., Ungár, T., Characterisation of the microstructure in random and textured polycrystals and single crystals by diffraction line profile analysis, Materials Science and Engineering A, 528 (2010) 112-121.

[121] Ungár, T., Dragomir, I., Revesz, A., Borbely, A., The contrast factors of dislocations in cubic crystals: the dislocation model of strain anisotropy in practice, Journal of Applied Crystallography, 32 (1999) 992-1002.